



A CFD and experimental approach for simulating the coupled flow dynamics of near wellbore and reservoir

by

© Mohammad Jalal Ahammad
B. Sc.(Hons), M. Sc., M.Phil.(CU-BD)
M.S. (MUN- Canada)

A thesis submitted to the School of Graduate Studies
in partial fulfillment of the requirements for the degree of
Doctor of Philosophy.

Mathematics and Statistics
(interdisciplinary Theoretical Physics Program)
Memorial University of Newfoundland

June 2019

ST. JOHN'S

NEWFOUNDLAND

Abstract

The modeling of simultaneous flow behavior through a reservoir and wellbore is important and an integrated model is needed which accounts for the transient multiphase flow in the wellbore and its surrounding region. In addition, reservoir and wellbore interface modeling and cost-effective Computational Fluid Dynamics (CFD) methodology are required to simulate the flow behavior in that region.

The study outlines the development of an experimental prototype to study multiphase flow in the near wellbore region. To the best of my knowledge, this facility has the capability to accommodate a larger length scale compared to similar facilities available in the research organizations. This experimental setup can be used for investigating a wide variety of multiphase flow problems which have been considered in the present research.

A CFD methodology has been developed using the 3D Navier-Stokes equations to simulate an integrated wellbore-reservoir flow. The CFD methodology has been verified for the fluid flow mechanism at near wellbore. The simulation results have been compared to the analytical solutions. Then, this model is extended to establish a coupled wellbore-reservoir framework which is based on 3D Navier-Stokes equations. The simulations have been performed to validate the newly developed CFD algorithm and various scenarios of a reservoir have been taken into consideration. The same process has been applied to investigate flow through a perforated tunnel and a new method of perforation has been discussed. The study indicates standard CFD techniques use a “numerical approach” such as the volume of fluid

accounts for capillary pressure and surface tension force needs to be improved for more understanding of the flow through porous media. In this regards, Allen-Chan phase-field method has been combined with the Navier-Stokes equations to simulate multiphase flow in porous media. The simulations performed with the phase-field method have been verified with the experimental data. The experimental and CFD approach of this thesis make a unique contribution in the field of the petroleum industry and multiphase flow in porous media.

Acknowledgement

First, I am very grateful to my supervisor, Dr. Jahrul M Alam, and Dr. Mohammad Azizur Rahman for accepting me as a graduate student in their interdisciplinary research group. I would like to express my deepest gratitude to them for their continuous support, insightful guidance, and patience during the research. Also special thanks to my supervisor for introducing me to such an interesting and challenging topic for my research and careful review of the manuscripts. It would be impossible to finish the dissertation writing up without their uncountable help. Especially, Dr. Alam trained me programming with his extraordinary efficiency and lovely care. Dr. Rahman guided me the experimental works in an easy way so that it was possible for me although I have a background in mathematics and computation. The whole period of my PhD program was an incredible journey where I had learned many things and matured in many ways.

I also acknowledge Compute-Canada and Memorial University for taking advantage of high-performance computing facilities.

Having mathematics and computational background, I was proud to be a member of interdisciplinary research group - the Drilling Technology Laboratory (DTL) at the Memorial University, Canada. I would like to take the opportunity by expressing gratefulness to Dr. Stephen D. Butt to guide me the experimental work which was a challenging task. They never compromised the quality of the research by any cost that helps to increase my depth of knowledge.

I would also like to thank Dr. Ivan Booth, head of Theoretical Physics program for financial and administrative support and my supervisory committee members Dr. Stephen D. Butt and Dr. James Munroe for their advice and wisdom.

I am grateful to the School of Graduate Studies and the Department of Theoretical Physics for providing financial support, and the Department of Mathematics and Statistics for arranging the Teaching Assistantship. The financial support from the scholarships “F. A. Aldrich Graduate Award”, “The Rev. Dr. Bernard J. O’Cornnor scholarship” and “Graduate Student’s Union Award for Leadership” are really appreciated since those scholarships forced me to do more focused on research.

I would like to mention the assistance I got from Mrs. David, Abdelsalam Abugharara, Li Zheng and Mohammad Said, team member of DTL laboratory at Memorial University, who were of the great assistance throughout the experimental phase of my research. I also like to extend thanks to the technical services department of Memorial University for their endless support especially Mr. David Snook, Supervisor, Mechanical Division.

I also appreciate the writing center of Memorial University for the help in English language corrections while preparing manuscripts.

Finally, I am very grateful and thankful to my parents, my wife Monuara and numerous friends for their continuous support and love, especially my kids, Jannat and Jami who got less love and take care from me because of my busy time during PhD research.

Statement of collaborations

Theoretical Physics program at Memorial University is an interdisciplinary PhD program and the present research is focused on a project which is the bridge between mathematics and engineering. The collaborations from different units and contributions of my supervisors are notable. My supervisors Dr. Jahrul Alam and Dr. Mohammad Azizur Rahman introduced me the research problem. Dr. Alam has significant contributions in setting up the computational algorithm and preparing the manuscripts, and reviewing the dissertation. He also provided all necessary computing facilities from Compute-Canada and Memorial University. Dr. Rahman has many contributions in experimental prototype development and reviewing manuscripts and dissertation. He spent his valuable time for this project although he was outside from Canada. All necessary supporting from DTL lab are notable. The strict guidance and follow up of Dr. Stephen Butt, principal investigator of DTL lab, Memorial University is remarkable. The technical support from the technical services department of Memorial University was very important and they showed their helping hand whenever was needed. In terms of financial support, School of Graduate Studies, Department of Mathematics and Statistics, Theoretical Physics program and supervisors grants have significant contributions in regards to complete the research. Mr. Li Zheng has contributions in some simulations only for the results presented in chapter 5. The detailed contributions are mentioned in chapter 1.

Contents

Abstract	ii
Acknowledgement	iv
Statement of collaborations	vi
List of Tables	xiii
List of Figures	xx
Abbreviations	xxi
1 Introduction	1
1.1 Motivation	1
1.2 Background	3
1.3 Objective	3
1.4 Research challenges	4
1.5 Lay summary of the research	6
1.6 Co-authorship statement	8
1.6.1 Authorship declaration	9
1.7 Novelty of the research	10

1.8	Organization of the thesis	11
2	Design of an experimental setup to characterise the flow phenomena at the near-wellbore region	13
2.1	Introduction	15
2.2	Structure of the RFC experimental setup	16
2.2.1	Main component of RFC	17
2.2.2	Fluid flow line	19
2.2.3	Axial load system	20
2.2.4	Assembling and disassembling apparatus	22
2.3	Methodology	22
2.3.1	Core sample preparation	22
2.3.2	Operating system of the RFC setup	25
2.3.3	Experimental procedure with RFC	26
2.4	RFC Device validation test	27
2.4.1	Possible leak test	27
2.4.2	Validation	28
2.5	Experimental results	29
2.5.1	Experiment with synthetic sample	29
2.5.2	Experiment with real sandstone sample	31
2.6	Rationale of the RFC experimental setup	33
2.7	Conclusions and recommendations	34
3	A CFD investigation of the flow behavior near a wellbore using Navier-Stokes equation	37
3.1	Introduction	39
3.2	Methodology	42

3.2.1	CFD model setup for near-wellbore simulation	42
3.2.2	Governing equation for flow through porous media	43
3.2.3	Boundary conditions	44
3.2.4	Analytical solutions of traditional models to validate CFD simulation	45
3.2.4.1	Pressure calculation using Darcy model	45
3.2.5	Pressure calculation using pressure diffusivity equation	46
3.2.6	Solution technique of NSE for petroleum industry	47
3.3	Inflow performance relationship formulation	49
3.4	Numerical results and discussions	49
3.4.1	Validation of CFD simulation against Darcy model	49
3.4.1.1	Comparing CFD simulations against the pressure diffu- sivity equation	51
3.4.2	Flow characteristic at the near wellbore	53
3.4.2.1	Flow behavior at near-wellbore region	53
3.4.2.2	Flow direction	55
3.4.3	Inflow performance relation analysis	56
3.4.4	Pressure distribution analysis using NSE	57
3.4.4.1	Different flow rates for linear flow model	57
3.4.4.2	Different flow rates for nonlinear flow model	63
3.5	Conclusion and future work	64
4	Wellbore-reservoir modeling based on 3D Navier-Stokes equations with a cou- pled CFD solver	67
4.1	Introduction	69
4.2	Methodology	71
4.2.1	Governing equation for flow through porous media	71

4.2.2	Boundary conditions	71
4.2.3	Pressure calculation using other models	72
4.2.3.1	Analytical solution of Darcy model	72
4.2.3.2	Analytical solution of pressure diffusivity equation	73
4.2.4	CFD model of oil reservoir	74
4.2.5	CFD technique to simulate coupled wellbore-reservoir model	77
4.2.6	Interface modeling for coupled wellbore-reservoir	78
4.3	Results and discussions	79
4.3.1	CFD model	79
4.3.1.1	Verification with the Darcy equation	79
4.3.1.2	Verification with pressure diffusivity equation for coupled wellbore-reservoir	82
4.3.2	Verification with inflow performance relation for coupled wellbore-reservoir	82
4.3.3	Coupled wellbore-reservoir model with formation damage	85
4.3.4	Comparison of coupled wellbore-reservoir with and without formation damage	85
4.3.5	Flow direction for coupled wellbore-reservoir with and without formation damage	89
4.3.6	Performance of coupled wellbore-reservoir model	91
4.3.6.1	Coupled wellbore-reservoir with different production rate	91
4.3.6.2	Coupled wellbore-reservoir study for different skin zones	91
4.3.6.3	Coupled wellbore-reservoir study for different reservoir formation	92
4.4	Conclusion and future work	95

5	Numerical investigation of two-phase flow in a perforation tunnel of a hydro-carbon reservoir	100
5.1	Introduction	102
5.2	Conventional perforation techniques	103
5.3	Proposed technique - Perforation by Drilling (PD)	105
5.4	Mathematical model	108
5.4.1	Computational technique	108
5.5	Results and Discussions	111
5.6	Conclusion and future work	115
6	Numerical simulation of two-phase flow in porous media using a wavelet based phase-field method	118
6.1	Introduction	120
6.2	Simulation methodology	125
6.2.1	Multiphase flow in porous media	125
6.2.2	The phase-field method and the surface tension	127
6.2.2.1	Dynamics of the two-phase interface	127
6.2.2.2	Surface tension	128
6.3	Computational procedures	129
6.3.1	Wavelet based CFD simulation	129
6.3.2	Simulation and parameters	130
6.4	Numerical simulations	131
6.4.1	Macroscale modelling of surface tension	131
6.4.1.1	Test case	132
6.4.1.2	Observation	132
6.4.1.3	Comments on the terminal bubble shape	133

6.4.2	Experimental validation of the bubble dynamics	133
6.4.2.1	Experimental data	136
6.4.2.2	Numerical simulations	136
6.4.3	Bubble dynamics in porous media	138
6.4.3.1	Two-phase flow simulation in a porous medium	138
6.4.3.2	Momentum balance and frictional force of porous media .	140
6.4.3.3	Numerical and experimental validation of the terminal velocity of a bubble	142
6.4.4	Mass conservation in a phase-field simulation	143
6.5	Conclusion and future work	146
7	Conclusion and future research direction	153
	Bibliography	156

List of Tables

1.1	The contributions of co-authors in the different perspective. The initials are: MJA- Mohammad Jalal Ahammad, JA- Dr. Jahrul Alam, SDB- Dr. Stephen Douglas Butt, MAR- Dr. Mohammad Azizur Rahman, and LZ- Li Zheng.	10
2.1	Parameter values used in the experimental study for real and synthetic samples.	30
3.1	Parameter values used in the analytical and simulations through out the article.	50
4.1	Parameter values used for the computational domain.	77
4.2	Parameter values used for the simulations in this paper. The data for computational domain and relative variables are adapted from (Molina & Tyagi, 2015).	81
5.1	Parameter values used for the computational domain.	109
5.2	Parameter values used for the computational domain.	109

List of Figures

2.1	Sketch of the experimental set up. (1) Air compressor, (2) and (11) Pressure release valve; (3) Air flow meter; (12) Liquid flow meter; (4) and (13) Control valve; (6) and (15) Non-return valve; (5), (7), (14) and (16) Pressure gauges; (8) and (9) Thermometers; (10) Pump; (17) Water Reservoir; (18) Radial flow cell; (19) Differential pressure gauge; (20) Computerized DAQ (Data Acquisition) system; and (21) Hydraulic pump.	18
2.2	Lab scale photograph of the experimental setup.	19
2.3	The prototype of entire the RFC, (a) two dimensional section view with different elements and (b) three dimensional view.	20
2.4	(a) Bottom and (b) top part, (c) Rubber membrane and (d) Arc support stabilizers (ASS) part of RFC with details view.	21
2.5	Prototype of (a) assembling and (b) disassembling apparatus of the experimental setup.	23
2.6	Photograph of (a) synthetic and (b) real samples used in the experimental.	24
2.7	Sensitivity of synthetic sample in Permeability at different confining pressure.	29
2.8	Pressure build up test with synthetic sample.	31
2.9	Pressure build up test with real sandstone sample.	32
2.10	Pressure draw down test with real sandstone sample.	33

3.1	(a) A computational design of reservoir along with a vertical wellbore, and (b) the near-wellbore region of a reservoir which is similar to the rest of the simulation in this research.	42
3.2	Flow chart for pressure based coupled solver.	48
3.3	Validation of CFD model based on Navier-Stokes equations for linear model ($\beta = 0$) with the analytical solution of Darcy equation for steady-state flow.	51
3.4	Comparison of pressure distributions calculated by NSE equations, and an- alytical solution of PD equation for nonlinear ($\beta = 2.3271 \times 10^8[\text{m}^{-2}]$) and linear ($\beta = 0$) <i>i.e</i> Darcy model.	52
3.5	Comparison of pressure drop as a function of flow rate at the wellbore surface where $\beta = 2.3271 \times 10^8[\text{m}^{-2}]$ and $\beta = 0$ for nonlinear and linear model respectively.	53
3.6	Pressure drop analysis at the near-wellbore with linear $\beta = 0$ and nonlinear models ($\beta = 2.3271 \times 10^8[\text{m}^{-2}]$).	55
3.7	The streamlines along a vertical cross section of the domain representing flow direction.	56
3.8	Comparison of the IPR curves: (a) steady-state IPR curves with theory, (b) time dependent IPR curves with theory.	58
3.9	Contour plots of pressure distribution along a vertical plane of the reservoir for steady-state linear model ($\beta = 0$) condition at different flow rates.	59
3.10	Pressure profiles for different flow rates of steady-state linear model ($\beta =$ 0) simulations.	60
3.11	Pressure distribution contour plot along a vertical plane for different flow rates for the simulations of nonlinear model ($\beta = 2.3271 \times 10^8[\text{m}^{-2}]$).	61

3.12	Pressure distributions as a function of radial distance to the wellbore for nonlinear flow model ($\beta = 2.3271 \times 10^8[\text{m}^{-2}]$). (a) For the flow rate, $q = 0.36803[\text{kg/s}]$, (b) For the flow rate, $q = 0.73606[\text{kg/s}]$, (c) For the flow rate, $q = 1.10408[\text{kg/s}]$ and (d) For the fixed time $t = 0.014\text{hrs}$ with different flow rates.	62
4.1	Idealized reservoir with vertical wellbore: (a) the sketch of a undamaged reservoir and (b) reservoir with skin zone (source: Chaudhry (2004)). . . .	75
4.2	Computational geometry of a typical reservoir with skin zone: (a) 3D view and (b) top view.	76
4.3	Comparison of present model with the analytical solution of Darcy equation for an idealised reservoir (without wellbore for CFD simulation): (a) pressure contour plot of the present CFD set up, (b) comparison of pressure profiles ($\beta = 0$ and $q = 474.36$ [bbl/day]).	80
4.4	Pressure profile distribution of a reservoir without skin zone (<i>i.e.</i> $\mathcal{K}_r = 250[\text{mD}]$, and $\mathcal{K}_s = \mathcal{K}_r = 250[\text{mD}]$), (a) pressure contour plot, (b) comparison of pressure profile with analytical solution of pressure diffusivity equation for ($\beta = 1.035 \times 10^8[\text{ft}^{-1}]$ and $q = 300.00$ [bbl/day]).	83
4.5	Inflow performance analysis with IPR curves for the reservoir without any skin zone.	84
4.6	Comparison of pressure profiles of an idealised reservoir with a coupled wellbore-reservoir including formation damage where idealised reservoir permeability, $\mathcal{K} = 250[\text{mD}]$, skin zone permeability (<i>i.e.</i> $\mathcal{K}_s = 50[\text{mD}]$, : (a) pressure contour plot, (b) comparison of pressure profile with analytical solution of pressure diffusivity equation for ($\beta = 1.035 \times 10^8[\text{ft}^{-1}]$ and $q = 300.00$ [bbl/day]).	86

4.7	Pressure contour plot for coupled wellbore-reservoir model. First row: (a) wellbore region without skin effect and (b) wellbore region with skin effect. Second row: (c) skin zone without its effect and (d) skin zone with its effect. Third row: (e) reservoir area without skin effect and (f) reservoir area with skin effect. All parameters are same except skin zone <i>i.e.</i> $\mathcal{K}_r = 250$ [mD] & $\mathcal{K}_s = 50$ [mD].	88
4.8	Comparison of pressure profile of the undamaged reservoir and damage reservoir with the analytical solution of PD to quantify the results presented in Fig 4.7.	89
4.9	Stream lines plot of the coupled wellbore-reservoir model representing flow direction: (a) without skin zone, (b) with skin zone.	90
4.10	Investigation of pressure drop for the different flow conditions for coupled wellbore-reservoir model.	92
4.11	Pressure contour plots for fixed reservoir formation with different skin zones such as skin permeability: (a) $\mathcal{K}_s = 150$ [mD], (b) $\mathcal{K}_s = 100$ [mD], and (c) $\mathcal{K}_s = 50$ [mD].	93
4.12	Effect of different skin zones on pressure drop, the pressure profiles are drawn along a horizontal line of the domain for the simulations presented in Fig:4.11.	94
4.13	Pressure contour plots for fixed skin zone with different reservoir formations permeability such as: (a) $\mathcal{K}_r = 250$ [mD], (b) $\mathcal{K}_r = 400$ [mD], and (c) $\mathcal{K}_r = 500$ [mD].	96
4.14	Effect of different reservoir formation permeability on pressure drop, the pressure profiles are drawn along a horizontal line of the domain for the simulations presented in Fig:4.13.	97

5.1	Sketch of an idealized reservoir well configuration with horizontal wellbore involving variety of the reservoir elements such as perforation tunnel, formation damage undamaged reservoir region etc.	104
5.2	Sketch of the experimental set up. (1) Air compressor, (2) and (11) Pressure release valve; (3) Air flow meter; (12) Liquid flow meter; (4) and (13) Control valve; (6) and (15) Non-return valve; (5), (7), (14) and (16) Pressure gauges; (8) and (9) Thermometers; (10) Pump; (17) Water Reservoir; (18) Radial flow cell; (19) Differential pressure gauge; (20) Computerized DAQ (Data Acquisition) system; and (21) Hydraulic pump.	106
5.3	A diagram of computational domain. Left figure is the computation geometry having a perforation tunnel at the center and right figure is the cross section of the domain representing the damage zone, undamage region, perforation tunnel and flow direction.	110
5.4	The Effect of Permeability on Injection Pressure.	111
5.5	The Effect of Porosity on Injection Pressure.	112
5.6	The Effect of Air Flow Rate on Injection Pressure.	113
5.7	The Effect of Back Pressure on Injection Pressure.	114
6.1	A schematic illustration of an oil reservoir, where a vertical wellbore with perforation tunnels are also shown. The figure is adapted from a similar illustration given by Rahman <i>et al.</i> (2007 <i>b</i>). Note that the fluid flow is vertical in the wellbore and horizontal in the reservoir. Bubbles may be present in the wellbore or in the reservoir. When the reservoir fluid enters into the wellbore, the flow rate is affected by the formation damage near the perforation tunnels.	122

6.2	Temporal evolution of a rising bubble in a liquid for various meshes of resolutions: (a) R1(32×64), (b) R2(65×128), (c) R3(128×256), (d) R4(256×512). All the cases are at the same time, $tD/W = 7.4$	134
6.3	Contour line plot of the simulations presented in Fig 6.2. The results represent how accurately the interface between two fluids have been resolved by various resolutions.	135
6.4	Time series of the velocity of the simulation presented in Fig 6.2. The results represent the convergence of the approximate solutions subject to the surface tension and truncation error.	135
6.5	Terminal shapes of the rising bubble in a liquid. (a), (d) and (g) are plots of the experimental results provided by Bhaga & Weber (1981). (b), (e) and (h) are plots of corresponding numerical results provided by Hua & Lou (2007). (c), (f) and (i) are plots of numerical results present CFD simulation. Although the physical conditions and parameters are not exactly the same for three cases, the comparison supports findings of ‘adverse’ pressure gradient in the wellbore.	137
6.6	Terminal shapes of a rising gas bubble in a liquid. (a), (c) and (e) are plots from the reference model provided by Hua & Lou (2007). (b), (d) and (f) are corresponding plots from the present CFD simulation. Although the modelling technique and the numerical method are not the same in both cases, the comparison supports the findings of the two-phase flow modelling approach considered in the present work.	139

6.7	The Effects of permeability on the shape of the rising bubbles. Here, all the parameters including porosity, $\phi = 18\%$ for the simulations are same except the Darcy numbers. The results (a) for the $\mathcal{D}a = 9 \times 10^{-3}$ with $t = 6.85$, (b) for the $\mathcal{D}a = 9 \times 10^{-4}$ with $t = 6.9$, (c) for the $\mathcal{D}a = 9 \times 10^{-5}$ with $t = 7.0$ and (d) for the $\mathcal{D}a = 9 \times 10^{-7}$ with $t = 8.9$	141
6.8	Time vs distance plot for a rising bubble. (a) A test of a rising bubble in a fluid. The data fit well with an average speed 25 cm/s. (b) A test of a rising bubble in a fluid saturated porous medium. The data fit well with an average speed 17.5 cm/s.	144
6.9	The terminal bubble velocity of a rising bubble as a function of the initial radius of the bubble. The present numerical study is compared with respect to the theoretical terminal velocity v_T and experimental data from Roosevelt & Corapcioglu (1998). (a) clear fluid, and (b) fluid saturated porous medium.	145
6.10	The time series representing the normalized mass of the gas phase. Clearly the total mass is conserved with sufficient accuracy. (a) The time series associated to the results in Fig: 6.2 (clear medium); (b) the time series associated to the results in Fig: 6.7(b) in the porous media with the Darcy number, $\mathcal{D}a = 9 \times 10^{-4}$. Note the terminal bubble shapes are very close for the selected results.	147

Abbreviations

Symbol	Description
AWCM	Adaptive wavelet collocation method
ASS	Arc Support Stabilizer
CFD	Computational Fluid Dynamics
CSA	Canadian Standards Association
DTL	Drilling Technology Laboratory
DAQ	Data Acquisition System
EOR	Enhanced Oil Recovery
IOR	Improve Oil Recovery
IPR	Inflow Performance Relations
NSE	Navier-Stokes Equations
PDE	Partial Differential Equation
PD	Perforation by Drilling
PPE	Personal Protective Equipment
RFC	Radial Flow Cell
TB	Terabytes
VA-NSE	Volume Averaged Navier-Stokes Equations
VOF	Volume of Fluid
CPU	Central Processing Unit

Chapter 1

Introduction

1.1 Motivation

Fluid flow phenomena in the near-wellbore region have importance in the well productivity analysis (Dake, 1983; Nind, 1989). Most of the parameters related to the well production are influenced by this region and the flow system is not fully understood (Ding, 2011). Generally, the fluid flow obeys Darcy's equation in the reservoir, away from the wellbore, and the pressure gradually decreases as the fluid moves towards the wellbore. In addition, the fluid flows at the near-wellbore is a radially convergent flow that causes the fluid velocity to increase continuously and inertial effect becomes important in the near-wellbore region (Li *et al.*, 2001; Song *et al.*, 2015). On the other hand, the fluid flow through a wellbore follows the fully non-linear or turbulent flow regime. Therefore, coupling the wellbore-reservoir flow in numerical simulation is an active research topic. In addition, an efficient CFD technique is needed for such simulations where proper interface modeling is required to couple wellbore and reservoir (Miller *et al.*, 1998).

Furthermore, multiphase flow occurs through wellbore or through porous media in different stages of hydrocarbon recovery *i.e.* cuttings cleaning (Horgue *et al.*, 2015a), forma-

tion damage analysis (Rahman *et al.*, 2007b), flow in fractured porous media (Wu, 2002a), EOR, and so on. During the entire hydrocarbon recovery process liquid, gas, and other solid particles migrate from the reservoir end to the near-wellbore region; however, this happens in deep underground locations that we do not have enough technology to directly visualize the geological multiphase flow regimes (Islam *et al.*, 2010). In practice, numerical studies and experiments of multiphase flow are primary tools to advance the knowledge on reservoir fluids flow phenomena towards the reservoir productivity and overall optimization of the reservoir (Higdon, 2013; Olbricht, 1996). For example, the study of multiphase flow helps to understand the oil and gas production performance that can be described in terms of the volumetric flow rate and the pressure gradient for the reservoir with different types of forces such as drag force by the porous media and surface forces of two fluids (Weisbrod *et al.*, 2009). The behavior of fluid flow near the wellbore region is not fully clear and there are many challenges in this regards (see for detail, Miller *et al.*, 1998; Branets *et al.*, 2009). Only the knowledge of the porosity and the permeability properties of porous media may not be sufficient to understand the reservoir fluid flow phenomena, especially, near-wellbore flow (Olbricht, 1996). The capillary pressure associated with surface forces also play an important role for the flows through porous media, for example, an increased permeability may increase the fluid flow rate if other parameters remain unchanged.

According to a brief literature review, it seems that the current understanding of multiphase flow in porous media is not complete yet (Miller *et al.*, 1998; Chen *et al.*, 2006b). Moreover, the existing numerical methods available in the literature are often found inadequate to analyze the skin effect in the perforation zone, as well as bubbly flow in fractured porous media (Chen *et al.*, 2006b). In petroleum industries, a large number of grid cells is required to capture the actual flow phenomena and about 90% of the total simulation time is spent in solving systems equations (Branets *et al.*, 2009). Therefore, a cost-effective CFD modeling can help to optimize the simulation process in this regard.

1.2 Background

A porous medium is a material that is characterized by the porosity and the permeability. The porosity is a measure of the pore space within a specific porous medium (Anovitz & Cole, 2015). The permeability is a measure of the ability of a porous medium to allow fluids to pass through it (Dullien, 2012). Darcy's equation approximates the flow through porous media *i.e.* the reservoir fluid flow. When there are a fracture or perforation tunnels in the near-wellbore of a reservoir, the flow phenomena can be explained using a non-linear model (Saboorian-Jooybari & Pourafshary, 2015; Khaniaminjan & Goudarzi, 2008; Wu, 2002b; Wu *et al.*, 2016). Recently, there is a trend to use Navier-Stokes Equations to describe flow through porous media including near-wellbore region (Molina & Tyagi, 2015; Ahammad *et al.*, 2017; Ahammad & Alam, 2017; Szanyi *et al.*, 2018; Ahammad *et al.*, 2018b). Computational capabilities have extensively increased at the end of the twentieth century, and as a result, the larger datasets can be handled and more physics can be considered into the problems of interest. This suggests advancing the CFD modeling approach for problems in petroleum industries.

1.3 Objective

The overall objective of this research is to study wellbore-reservoir flow and analyse near-wellbore flow phenomena using the 3D Navier-Stokes Equations and state-of-the-art of CFD techniques based on experimental knowledge and field observations. In particular, the experiments in the laboratory and CFD simulations are employed to improve the current understanding of multiphase flow regime in porous media. More specifically, the following are the research objectives.

1. Propose an experimental prototype to design advanced oil and gas flow process by

characterizing the near-wellbore phenomena and addressing the impacts of formation damages.

2. Designing a coupled CFD solver based on the VA-NSE to study of near-wellbore fluid flow phenomena of a reservoir.
3. Modeling of wellbore-reservoir coupling with Navier-Stokes Equations capturing the multiphysics phenomena of a reservoir.
4. CFD investigation of multiphase flow phenomena in order to characterize the impact of formation damages due to various types of perforation techniques used in petroleum industries.
5. Develop a CFD algorithm for multiphase flow in porous media using the VA-NSE and the Allen-Cahn phase-field method.

An important aspect of this research is to introduce a reusable CFD simulation platform for multiphase flow in porous media. The research community may be benefited from using it for other prospects and so that the model will be more validated. The attempt to apply a phase-field method to the study of flow through porous media is pioneering work. Coupling a reservoir and a wellbore using the Navier-Stokes Equations with a coupled CFD solver is another innovation of this research. The novelty of the experiment is mentioned in the experimental section.

1.4 Research challenges

Despite significant advancement of multiphase flow in porous media the research on this area still faces some issues. The issues are involved in the flow governing equation, computational technique, and experimental development (Miller *et al.*, 1998; Branets *et al.*,

2009). The reservoir formation is also complex in nature itself. Moreover, after long-term production, the reservoir fluid properties and the wellbore conditions may change, thus the understanding of the reservoir performance and future forecasting become more challenging (Wang, 2016). Thus, the reliable and sophisticated tools are needed to understand the real scenario of the reservoirs conditions (Islam *et al.*, 2010).

In the process of hydrocarbon recovery, different approaches are used to study different problems of interest in this field. The experimental development is a multidisciplinary research, thus it requires active collaborations in different fields. The experiment can be performed for a limited range of problems and operating conditions with at a limited number of points and time instants. Reservoir-scale is much higher than the lab scale for any types of experimental study (Rahman *et al.*, 2007b). Thus, the scale gap is another challenge in the experimental study. Moreover, the experimental process is expensive, slow, and changing parameters is not straightforward.

Reservoirs and their fluids have different characteristics such as heterogeneity, viscosity, surface tension, and permeability. In addition, reservoirs have different flow regimes such as flow in a low permeable region, perforated tunnel, and wellbore (Molina & Tyagi, 2015). Thus, the coupling of all flow regimes in a single equation is challenging endeavour (Tang *et al.*, 2017; Vicente *et al.*, 2000) and the different boundary conditions are needed to solve the flow governing equations (Arzanfudi *et al.*, 2016; Helmig *et al.*, 2013). The satisfying mass conservation law is also another issue which is important in reservoir simulations studies (Miller *et al.*, 1998). Furthermore, the study of multiphase flow in porous media has another window of the challenges due to the changing topological shape of the capillary interface (Antanovskii, 1995). By considering all those properties, the mathematical theory for the flow in porous media *i.e.* reservoir fluid flows is quite challenging and interesting subject of research.

The simulations in the reservoir studies face challenges in computational complexity

because of the length scale of the actual flow (Miller *et al.*, 1998; Branets *et al.*, 2009). Geological reservoirs are tens of kilometers in length *i.e.* $\mathcal{O}(\text{km})$ and several meters in depth *i.e.* $\mathcal{O}(\text{m})$; for example, the Weyburn oil field in Canada has a productive area of about 180 km^2 (Elsayed *et al.*, 1993). However, the actual flow occurs at micro meter scale *i.e.* $\mathcal{O}(\mu\text{m})$ (Popov *et al.*, 2009; Hasle *et al.*, 2007). Thus, for a typical reservoir with 10 km length, 10 km wide, and 100 m deep, we need $10^{10} \times 10^{10} \times 10^8$ grid points for a simulation which aims to capture the actual fluid flow with the spatial step size, $\Delta x = 1 \mu\text{m}$. Pruess & Zhang (2008) attempted to determine the optimal of Δx using the Darcy's equation, and found that at least $\Delta x = 1 \text{ mm}$ is reasonably sufficient to resolve flow phenomena. For such a case, $10^7 \times 10^7 \times 10^5$ grid points are needed for a single simulation. According to this typical scenario, a naive estimate shows that $10^6 - 10^{15} \text{ TB}$ computer memory is required. Therefore, a sophisticated CFD approach may help to resolve the actual flow as much as possible with optimal computational cost.

1.5 Lay summary of the research

In the petroleum industry, 80 – 90% of the computation time is spent to solve the system of equations that arise from the discretization of the model equations (Redondo *et al.*, 2018). Generally, Implicit Pressure Explicit Saturations (IMPES) methodology is applied in the most of reservoir simulations. This method has been successfully applied and some improvements on this were achieved over time. In the modeling of near-wellbore flow, pressure, temperature and velocity rapidly change and the simulation methodology needs to improve in that case (Chen *et al.*, 2004). In addition, the collocated grid arrangement offers significant advantages on complex domains and the vector and scalar variables store at the same locations on the grid (Abbasi *et al.*, 2013). Furthermore, the usage of multigrid methods in solving the system of equations accelerates the solution process. However, col-

located grid arrangement becomes prominent in the developments of the pressure-velocity coupling algorithms, and Rhie & Chow (1983) interpolation scheme helps to overcome the occurrence of unexpected oscillations in the pressure field calculation in this algorithm (Tu *et al.*, 2018).

In this research, we model an integrated wellbore-reservoir coupling technique for the fluid flow using the Volume Averaged Navier-Stokes Equations. The system of discretized equations is solved in a coupled manner on a collocated grid arrangement *i.e.* a single large system of equations is solved simultaneously for pressure and momentum. The primary outcomes of this research project are articulated below.

1. The development of an experimental device that is able to characterize the near-wellbore phenomena and study the impact of formation damage. This equipment can be used in other related research areas such as EOR, heat transfer through porous media.
2. The experimental results including validation test towards the development of the experimental facility are summarised and submitted to the 38th International Conference on Ocean, Offshore and Arctic Engineering, Glasgow, Scotland, 2019, ASME.
3. Primary CFD simulations towards the development of multiphase flow modeling are presented and published in the Society of Petroleum Engineers (SPE)- International Conference and Exhibition on Formation Damage Control, USA (2016).
4. The results towards the development of a CFD model for two-phase flow in porous media using VA-NSE and phase-field method are published in an article in the Journal of Chemical Engineering Science in 2017.
5. The outcome of the research towards CFD investigation of multiphase flow phenomena to study the impact of formation damages due to various types of perforation

techniques is published in the Journal of Natural Gas Science and Engineering in 2018.

6. The results in the designing of a coupled CFD solver based on VA-NSE to study of near-wellbore fluid flow phenomena of a reservoir are summarised in a manuscript and submitted to a special issue – Numerical Simulation and Novel Construction Methods in Oil and Gas Engineering of the Journal of Advances in Mechanical Engineering, published by SAGE.
7. The results towards the development of an integrated wellbore-reservoir coupling model with the Navier-Stokes Equations by capturing multiphysics phenomena of a reservoir are summarised in a manuscript and submitted to the journal of Petroleum Sciences and Engineering.

1.6 Co-authorship statement

This is a manuscript based thesis, thus there are contributions in the research articles from different individuals. This chapter describes the contributions of the co-authors. I am the sole author of chapter 1 and 7, and I have 90% contributions in the most chapters . The experimental facility described in chapter 2 is designed with the collaboration of Drs. Butt, Rahman, Alam. The research problems described in chapter 3 and 4 is designed by myself with the consultation of Drs. Rahman and Alam. Dr. Rahman has the contribution in chapter 5 and Dr. Alam has the contribution in chapter 6 to design the research problems. The details contributions of the respective author are described in the next section.

1.6.1 Authorship declaration

The contributions of the authors are summarized in the Table 1.1.

Table: 1.1								
	Design and identification of the research problem	Developing method/ algorithm	Perform research works	Data analysis	Providing facilities computation / experimental	Manuscript preparation/ review	Contribution in percent	Status
Chapter 1	MJA	---	---	---	---	---	MJA - 100%	Introductory Chapter
Chapter 2	MJA, SDB, MAR	MJA, SDB	MJA	MJA	SDB, MAR	MJA, JA	MJA 90% Others 10%	Accepted, ASME-38th International Conference, Scotland, UK
Chapter 3	MJA	MJA, JA	MJA	MJA	JA, MAR	MJA, JA MAR, SDB,	MJA 90% Others 10%	Submitted to J. Adv. Mech. Eng. (sp. issue) - SAGE pub
Chapter 4	MJA	MJA, JA	MJA	MJA	JA, MAR	MJA, JA MAR, SDB,	MJA 80% Others 20%	Submitted to J. Pet. Sci and Eng. - Elsevier
Cont...								

Chapter 5	MJA, MAR	MJA	MJA, LZ	MJA	MAR	MJA, MAR JA, SDB	MJA 80% Others 20%	Published in J. Natural Gas Sci. and Eng. Vol.55, 2018 - Elsevier
Chapter 6	MJA, JA	MJA, JA	MJA	MJA	JA	MJA, JA MAR, SDB	MJA 80% Others 20%	Published in J. Chem. Sci. and Eng. vol.173, 2017 - Elsevier
Chapter 7	MJA	---	---	---	---	---	MJA - 100%	Concluding Chapter

Table 1.1: The contributions of co-authors in the different perspective. The initials are: MJA- Mohammad Jalal Ahammad, JA- Dr. Jahrul Alam, SDB- Dr. Stephen Douglas Butt, MAR- Dr. Mohammad Azizur Rahman, and LZ- Li Zheng.

1.7 Novelty of the research

The fluid dynamical interaction of oil (and gas) reservoir with a wellbore which occurs usually in the near wellbore zone has been studied in this thesis. Such interactions dictate whether narrow tunnels between a wellbore and a reservoir would be constructed through a “shooting method” or a “drilling method”, and how to mitigate the impact of formation damage. A relatively small improvement in fracturing or drilling technology may introduce an order of magnitude economic benefit in the petroleum industry. The thesis contributed toward the development of a modeling approach in which a coupled system of “wellbore and reservoir” can be simulated through either a scaled model of physical experiment or a numerical model through Computational Fluid Dynamics (CFD). Through this PhD project, laboratory experiments, field measurements, and numerical simulations have been combined to develop a CFD methodology to illustrate some aspects of fluid dynamics,

which are among primary concerns in the oil and gas industries. The newly developed experimental setup has the capability to perform the investigation of the flow characteristics with a higher scale of parameters such as dimensions of the core sample compared to others setup, for example, Rahman *et al.* (2007c). A core sample is innovated in the laboratory for this study which has a higher permeability with high strength. The radially convergent and divergent flow facility of the device leads to perform more research in this research area. 3D NSE is applied to understand the fluid dynamics of at the near wellbore and reservoir. An efficient CFD methodology is developed to solve the system of linear equations in a coupled manner for the flow through porous media. An Algebraic Multigrid solver is applied to accelerate the solution. Furthermore, an integrated wellbore-reservoir coupling approach with skin zone is applied to study nonlinear flow behavior of flow from the reservoir to the wellbore. Finally, Allen-Cahn phase-field methodology is used to model surface force for the flow through porous media. Best of the author knowledge, the implementation of the phase-field method for the flow through porous media is new. In this study, an optimal wavelet method is used for the solution technique.

1.8 Organization of the thesis

The research focused on this dissertation is organized as follows. Chapter 1 describes the motivation, background, challenges, and research opportunity of the present project in this field. The contributions of the different authors in published and submitted papers of this research project are given in chapter 1 with the details. The experimental prototype development to study near-wellbore phenomena and formation damages are described step-by-step in chapter 2 with the validation tests. The experimental facilities help to get the idea of a real situation of a problem although it has some limitations such as the parameters of interest cannot be changed as frequently as desired. The CFD investigation can help more

in this regard. In chapter 3, near-wellbore phenomena of a reservoir are described with 3D Navier-Stokes equations. A CFD algorithm based on a coupled solver is implemented with an algebraic multigrid technique for the simulations. The modeling of wellbore-reservoir coupling is described in chapter 4. The CFD algorithm developed in the previous chapter is used here and interface modeling for reservoir and wellbore boundary is also implemented. The different reservoir formations and skin zones are considered, and flow performance is analyzed in this chapter. Next, in chapter 5, we study fluid flows through a perforation tunnel to investigate formation damages. Perforation by drilling is introduced here as a new technique and its benefit is studied for the different conditions. In chapter 6, the two-phase flow through porous media is studied using the Navier-Stokes equations combining with a phase-field method. A wavelet-based phase-field method is used for the numerical simulations. This method will continue to provide insight understanding of multiphase flow in porous media. Finally, conclusions are drawn and perspectives on future work are discussed in chapter 7.

Chapter 2

**Design of an experimental setup to
characterise the flow phenomena at the
near-wellbore region**

Title of the article: *An experimental development to characterise the flow phenomena at the near-wellbore region*

Authors: *M Jalal Ahammad*¹, *Mohammad Azizur Rahman*², *Stephen D Butt*³,
*Jahrul M Alam*⁴.

Corresponding author: Mohammad Azizur Rahman; email: marahman@tamu.edu
The 38th International Conference on Ocean, Offshore and Arctic Engineering,
Glasgow, Scotland, UK, 9 – 14 June 2019, ASME.
(Accepted for presentation and publication).

Abstract: The understanding of rock characteristic and fluid flow behavior at the near-wellbore region is an important topic. Triaxial experiment setup can help to investigate these properties. In this research, a new triaxial experimental setup has been developed where the higher scale of the parameters such as higher reservoir pressure, and comparatively larger core sample can be used. High permeable synthetic porous samples are prepared to validate the device. The new triaxial experimental setup is validated with water as a base fluid. In the validation test, real samples and synthetic samples are used. First, flow in convergent direction is studied which represents as production at the in-situ condition. Then, the flow in divergent direction is examined that may represent the injection of fluid to enhance the hydrocarbon production. The near-wellbore flow phenomena are studied with real and synthetic samples. The results indicate that using this triaxial setup pressure drop and pressure buildup test can be explained. The new experimental setup is able to reduce the scale-up gap between laboratory data and field data to get actual reservoir flow phenomena.

¹Mathematics and Statistics, Memorial University, Canada, A1C 5S7

²Petroleum Engineering, Texas A& M University, Qatar

³Process Engineering, Memorial University, Canada, A1C 5S7

⁴Mathematics and Statistics, Memorial University, Canada, A1C 5S7

Keywords: Radial flow cell, permeability, high permeable synthetic sample, near-wellbore region, formation damage.

2.1 Introduction

The reservoir rock properties change during the well production and mainly happens at near the wellbore region Hillel (1998); Holt *et al.* (2000); Zoback (2010). This phenomenon happens in the underground which is more than 1[km] in depth. The investigations of rock properties and fluid flow behavior through underground reservoir formation can be performed by triaxial setup Barla *et al.* (2010). The triaxial tests are of vital importance for rock characterization and to understand the flow phenomena near the wellbore. These studies help to provide the input parameters required for production engineer and numerical modeling studies Perera *et al.* (2011). Triaxial setup can also be used for numerous studies such as rock characterization, sequestration of CO₂, N₂, brine, etc. Somerton *et al.* (1975); Viete & Ranjith (2006); McKee *et al.* (1988). Further, the triaxial setup is often used to investigate the stability of deep underground mines and large open pit mines, deep underground disposal of nuclear wastes, assist with interpretation of in-seam seismic surveys Barla *et al.* (2010); Shepherd *et al.* (1981); Butt *et al.* (2005). Butt (1999) developed a triaxial apparatus to characterize the sandstone for the gas flow. Rahman *et al.* (2007c) introduced an experimental procedure with GDS triaxial setup to study formation damage due to drilling. Barla *et al.* (2010) introduced a new triaxial apparatus to investigate the mechanical properties of rock with higher confining pressures and indicated that the mechanical influence of fluid flow within the rock was not studied extensively. Ranjith & Perera (2011) developed a new apparatus to investigate the mechanical and fluid flow aspects of carbon dioxide sequestration in geological formations. In addition, most of the research using triaxial setup was designed for axial flow, for example, Rahman *et al.* (2007c).

Usually, rock samples of the reservoir formation or similar rock are cored in laboratories for the desired investigations through the triaxial setup. The rock sample collection is very crucial as it should represent the reservoir formation. The core samples may be prepared in the lab or collected from the desired place, for example, Butt *et al.* (2005) collected the sample from the mine field, Nova-Scotia, Canada; and Rahman *et al.* (2007c) prepared the samples in lab for their studies. In the laboratory, core samples can be prepared in different ways. Holt *et al.* (2000) prepared and investigated synthetic samples to simulate in-situ rock conditions. Their investigation indicated that synthetic specimens can be used in place of real cores for laboratory investigations.

The current study introduces a new triaxial apparatus which is developed and housed at DTL laboratory at the Memorial University, Canada. The setup is named as Radial Flow Cell (RFC) and designed to characterize the near-wellbore formation and flow behavior. The setup is also capable to study radially convergent and divergent flow that can be applicable for EOR process or waste disposal in the underground. The experimental setup in the study of radial flow phenomena at the near wellbore flow is limited and most of the setup is small scale, for examples, Butt (1999); Rahman *et al.* (2007a). The present experimental setup has a wide range of applications such as the near-wellbore flow phenomena including formation damage that happens during the well completion. Moreover, in this research, the synthetic samples are made of epoxy glue in DTL laboratory at the Memorial University and real sandstone samples collected from Nova-Scotia, Canada to validate the newly developed experimental setup.

2.2 Structure of the RFC experimental setup

This setup has different components that can be categorized into four main parts: a) Radial flow cell, b) Fluid flow line, c) Axial load system and, d) Assembling and disassembling

apparatus. The sketch of the setup is illustrated in Fig: 2.1 and full lab scale is shown in Fig: 2.2.

2.2.1 Main component of RFC

This is the most important part of the current development of this experimental setup. The device is fully design and developed in Drilling Technology Laboratory (DTL) at Memorial University. All the metal parts are made of stainless steel. The RFC (see, Fig: 2.3) contains four parts: i) outer shell, ii) top part, iii) base/bottom-part and iv) rubber membrane. The detailed description of the parts are as below:

i) Outer shell – This is the outer part of the RFC. This part holds the confining pressure. It has three holes: the middle one acts as an inlet of hydraulic oil to create confining pressure, the bottom one is for the draining of hydraulic oil and the top one is for air release. This RFC is capable to hold confining pressure up to 3,000 [psi].

ii) Top part – This is the top-most part of the RFC and stands on the porous sample (Fig: 2.4(b)). It has four flow lines, two O-Ring grooves, six screw holes for the Arc support stabilizers (ASS) and a rubber gas kit. The center flow line can be used as an outlet and other three side flow lines can be used as an inlet for convergent flow study. The flow lines can be altered for divergent flow by switching from a control panel. O-rings are used to prevent hydraulic oil from leaking out of the cell to have the desired confining pressure. The gas kit prevents any possible liquid slipping from the inlet.

iii) Base/bottom part – This is the base part of the RFC and sits on the bottom part of the axial load system (Fig: 2.4(a)). It also has two O-Ring grooves, six screw holes for the ASS and a rubber gas kit. O-rings are used to prevent hydraulic oil from leaking out of the cell to have the desired confining pressure. The gas kit prevents any possible unwanted liquid slipping from the inlet.

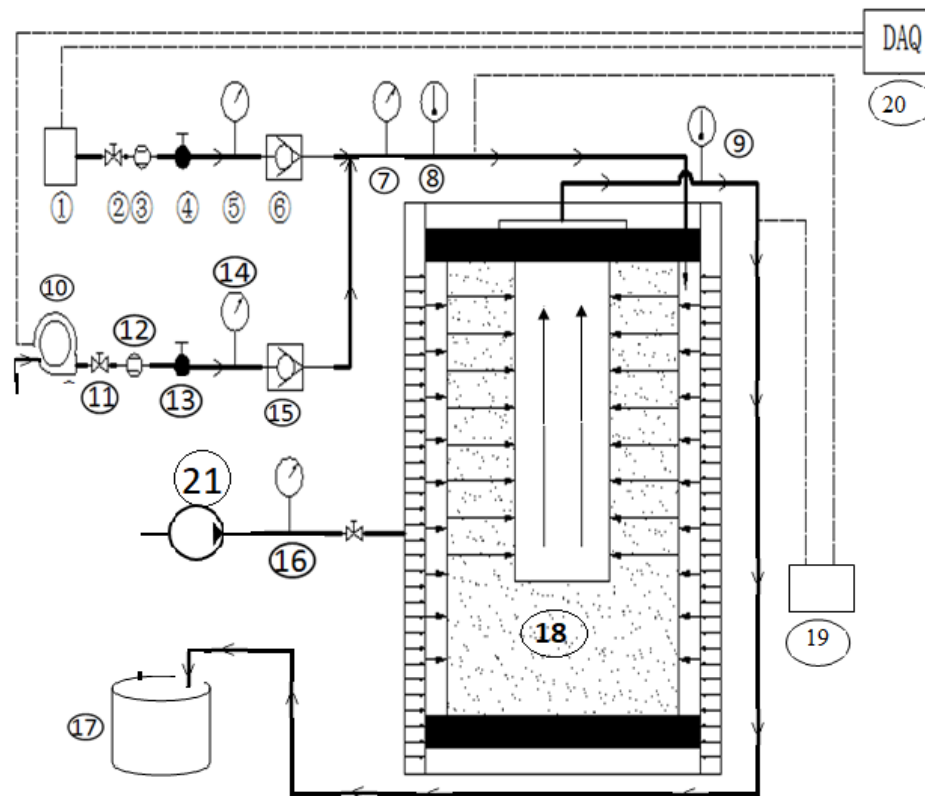


Figure 2.1: Sketch of the experimental set up. (1) Air compressor, (2) and (11) Pressure release valve; (3) Air flow meter; (12) Liquid flow meter; (4) and (13) Control valve; (6) and (15) Non-return valve; (5), (7), (14) and (16) Pressure gauges; (8) and (9) Thermometers; (10) Pump; (17) Water Reservoir; (18) Radial flow cell; (19) Differential pressure gauge; (20) Computerized DAQ (Data Acquisition) system; and (21) Hydraulic pump.

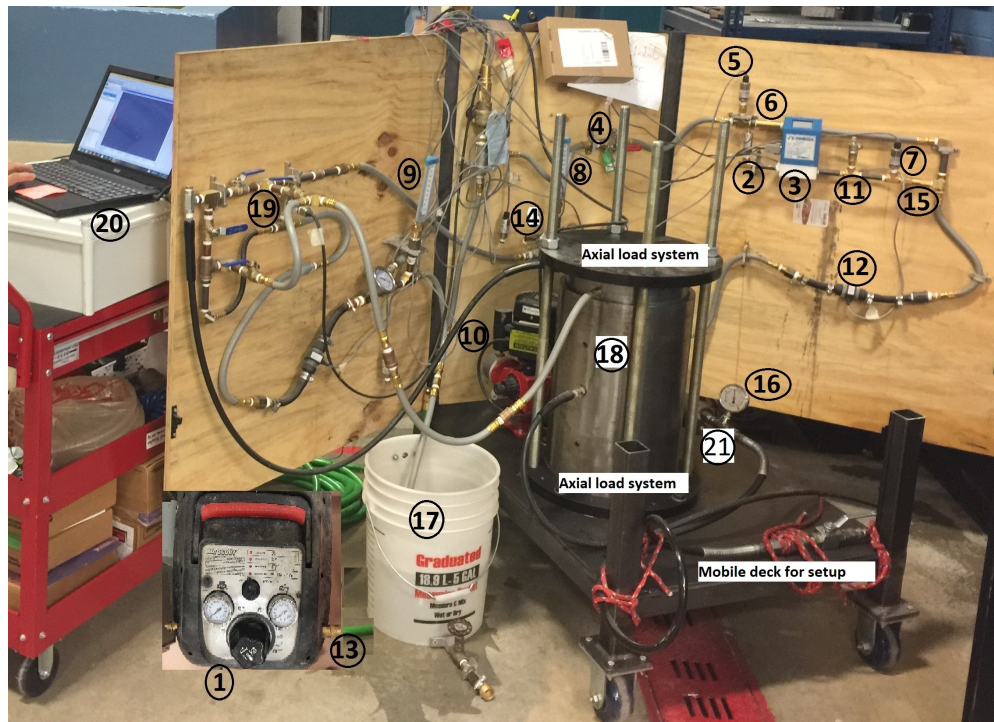


Figure 2.2: Lab scale photograph of the experimental setup.

iv) Rubber Membrane – This is the most important component (Fig: 2.4(c)) since it will help separate hydraulic oil from the experimental fluid, which is injected separately. The purpose is to provide a 360-degree seal on both top and bottom side. The bottom side of the rubber is attached to the bottom part and is held in place by ASS (Fig: 2.4(d)) with screws and the top side is attached to the top part in the same way. The whole RFC sits on the platform of the mobile deck (Fig: 2.2).

2.2.2 Fluid flow line

This component consists of flow meters, pressure gauges, inlet, and outlet flow boundary, flow control valve, pumps and temperature meters. The schematic diagram is shown in Fig: 2.1 and lab scale is displayed in Fig: 2.2. The pressure gauges have the range up to 200 [psi]. A positive displacement pump with a pressure range up to 145 [psi] is used for

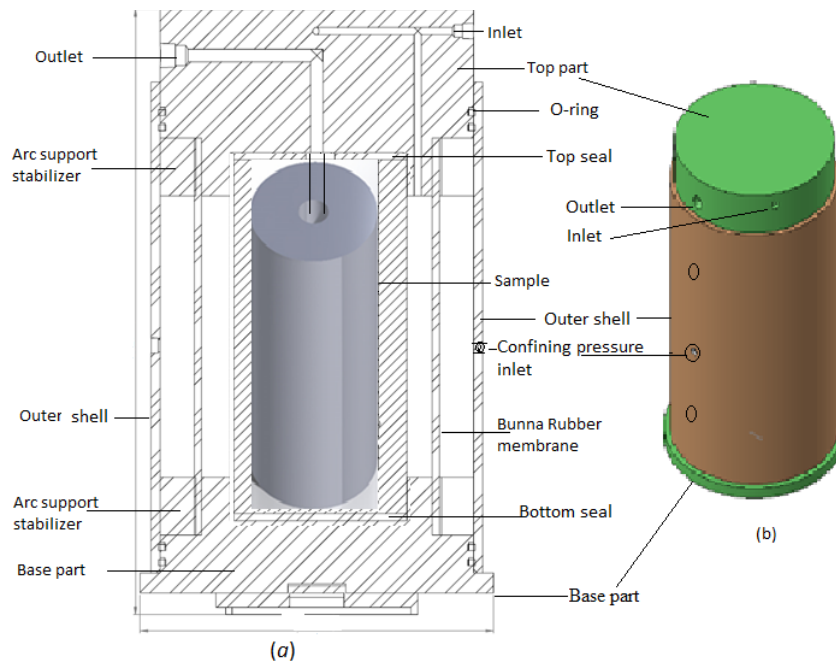
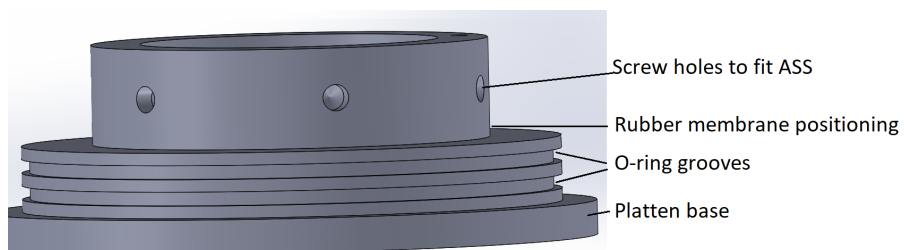


Figure 2.3: The prototype of entire the RFC, (a) two dimensional section view with different elements and (b) three dimensional view.

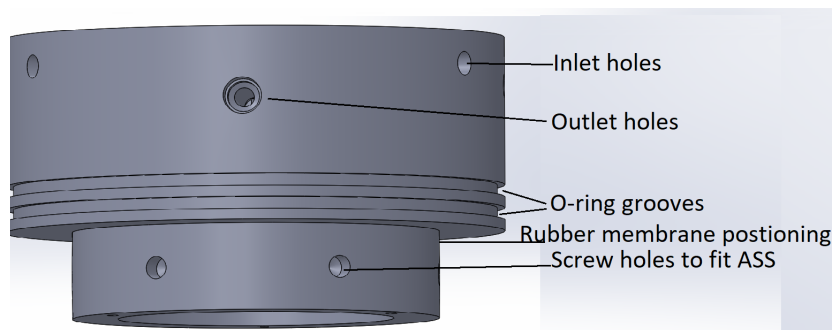
liquid supply with a fixed flow rate. Flow meters are selected within the desired range. Note that, flow meters and pressure gauges are designed for low frequency; it requires signal conditioning. The experimental set-up is also equipped with the digital data recording system which allows the recording of dynamic behavior response of the inlet and outlet pressure, differential pressure and flow rates. The Mobile DAQ can be attached to set-up to collect continuous required data for a certain flow period.

2.2.3 Axial load system

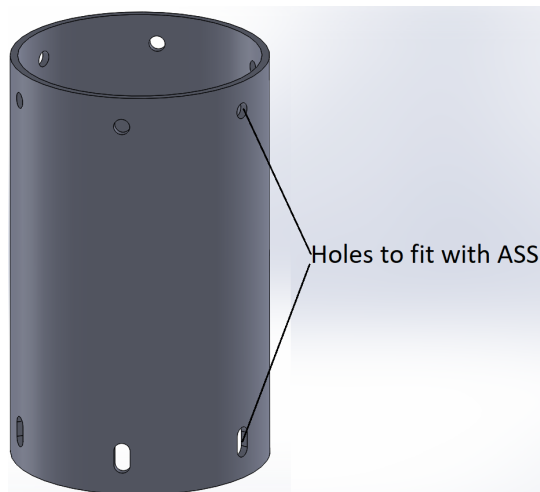
The axial load system is important to prevent possible leakage of fluid (Fig:2.1). One plate is set at the bottom and another one on the top of the RFC with four high strength rods to distribute pressure evenly.



(a)



(b)



(c)



(d)

Figure 2.4: (a) Bottom and (b) top part, (c) Rubber membrane and (d) Arc support stabilizers (ASS) part of RFC with details view.

2.2.4 Assembling and disassembling apparatus

The RFC cell is made of stainless steel and performs the stress analysis using Solidworks stress simulations. The total weight of the RFC is about 500 [kg]. Thus, it is demanded an efficient assembling and disassembling apparatus to handle this setup. Brainstorming is performed within the research group and a couple of options are find out. Considering safety, simplicity and economic factors; the present assembling and disassembling apparatus is designed (Fig:2.5). This apparatus consists of one clamp, one plate, three small rods, and one threaded rod with a mechanical head. The clamp is placed on the surface of the outer shell of RFC, three small rods are attached to clamp and plate, then the mechanical head of the threaded rod is placed at the center of the top part of the RFC. In the case of assembling, the threaded rod rotates in the clockwise direction, then the outer shell goes down slowly by sliding over the top part of RFC. The process needs to keep continue until outer shell reaches to the bottom part platen plate. In the case of disassembling purpose, the threaded rod needs to rotate in the anti-clockwise direction, then the outer shell will come out. To complete the process, support from a cherry picker is required.

2.3 Methodology

In this section, we describe the technique of core samples preparation and the step-by-step process of the experimental procedure.

2.3.1 Core sample preparation

In this research, we consider two types of cylindrical samples: one is made of sand particles with epoxy glue and another one is a real sandstone from Nova Scotia, Canada. The first one is named synthetic and second one is a real sample. The specimens are prepared with

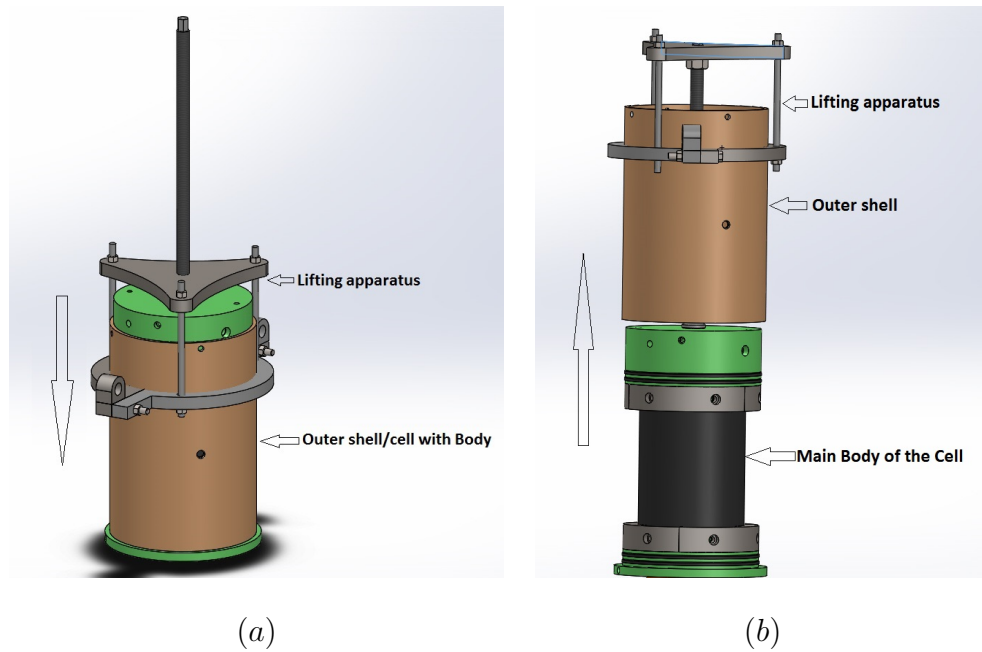


Figure 2.5: Prototype of (a) assembling and (b) disassembling apparatus of the experimental setup.

length and dimension ratio of 2 following (Butt *et al.*, 2005). The size of the samples are height, 12 [in] and radius, 6 [in] with a hole of radius, 0.50 [in] at the middle up to 11 [in]. The synthetic sample made of sand particle size of 1.00 – 1.50 [mm] and we consider the following recipe as: amount of sand – 6434.8 [kg] and epoxy glue – 450 [ml] with hardener – 40 [ml]. Real sample from Nova Scotia is prepared by cutting from the square shape of a sample with the curing bit. Pictures of both samples are displayed in Fig:2.6. The core samples are prepared for the test in accordance with standard practices as (D4543, 1985). The porosity of the samples is measured using Archimedes principle as:

$$\text{Porosity, } \phi = \frac{V_v}{V_T},$$

where Pore volume, $V_v = \text{Mass of saturated sample at air} - \text{Mass of unsaturated sample at air}$ and Bulk volume, $V_T = \text{Mass of saturated sample at air} - \text{Mass of saturated sample in water}$.

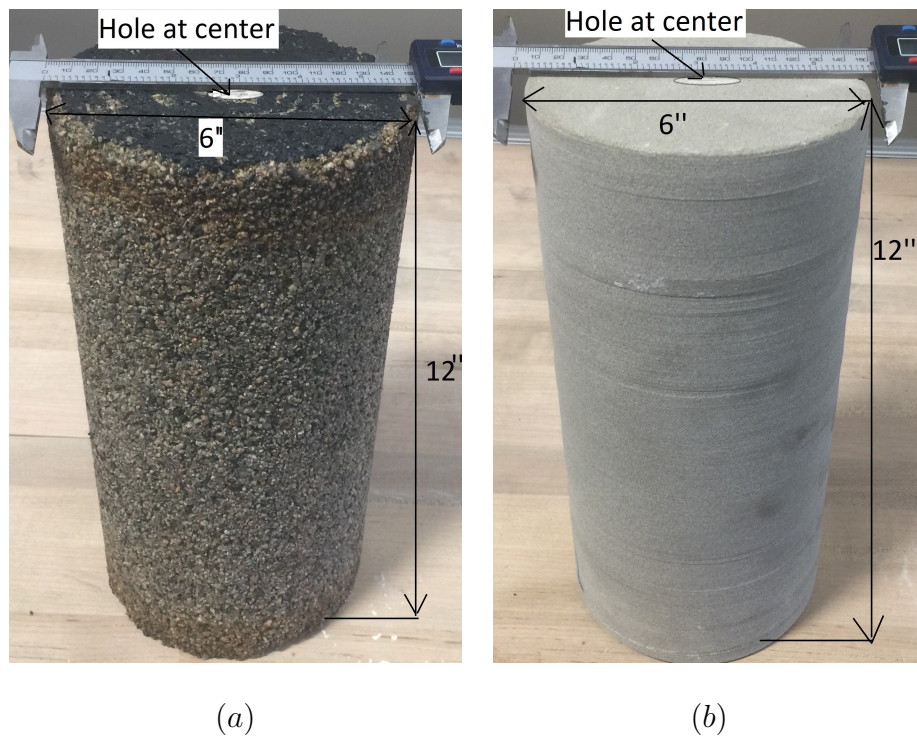


Figure 2.6: Photograph of (a) synthetic and (b) real samples used in the experimental.

2.3.2 Operating system of the RFC setup

Before starting experiments the followings Personal Protective Equipment (PPE) have to obey for safety rules and regulations. Canadian Standards Association (CSA) approved safety footwear, Protective goggles, Lab coat, and Glass shield. The following section will provide the step-by-step procedure to perform a potential experiment.

Step-by-step procedure of the experiment:

1. Collect all the required materials.
2. Place the base plate of an axial system on the mobile deck.
3. Place base/bottom part of the RFC with a gas kit on the base plate.
4. Place porous sample in the middle of base/bottom part of the RFC.
5. Place rubber membrane on its position as shown in Fig:2.4 so that the holes are aligned with the holes of ASS fitting.
6. Tightly clamps the rubber membrane with bottom part by ASS.
7. Pack coarse particle into the empty annular region between sample and rubber membrane of RFC and make sure the region is compacted evenly.
8. Place the top part of RFC with a gas kit on the sample and make sure it fits with the upper side of the rubber membrane and aligned with the holes. Place the ASS with a rubber membrane to the top part and tight them to ensure no possible leakage.
9. Wire O-rings on the grooves of the bottom and top part of the RFC.
10. Arrange assembling apparatus to place outer shell over the top part of RFC.

11. Operate assembling apparatus in the appropriate direction to place the outer shell on the plate of the bottom part. The set up looks like Fig: 2.5(a).
12. Place the top plate of axial load system on the top part of RFC and place four threaded rods through the holes of top and bottom plate of the axial load system, now tighten all fittings to ensure no possible leakage.
13. The assembling of RFC is completed.
14. Set other components such as flow line and sensors of the setup.
15. After finishing the experiment, disassembly can be done with disassembling apparatus by operating in the opposite direction of the assembling process as shown in Fig: 2.5(b).

2.3.3 Experimental procedure with RFC

After assembling the setup following steps need to ensure to perform the experiment

1. Close all the valves for safety and make sure everything performs in a step-by-step manner.
2. Hook up water line into the pump, then place the outlet of the reservoir.
3. Plug in all sensors to the DAQ (Data Acquisition) system following the diagram.
4. Plug in all power switches where necessary.
5. Turn on inlet water line while turning on the outlet line, and keep it flowing for sometimes so that the sample becomes fully saturated.
6. When the outlet flow becomes steady then generate desired confining pressure through the hydraulic pump.

7. Before the final experiment, it is better to perform a pre-test.
8. All the data will save in Labview software as an excel file system.
9. In the post-process, data are plotted using Matlab script.

2.4 RFC Device validation test

It is very important to validate any new apparatus/technology same as CFD model needs to validate before modeling any physical problem. First, we check any possible leak to confirm the applicability of the device and then single phase flow is considered to the radially convergent and divergent direction.

2.4.1 Possible leak test

The leak test is a more challenging task in this development. There is two possible leaking problem: one is hydraulic oil, another one is inlet fluid leaking through the top and bottom part of RFC. Couples of investigations are performed to ensure that there is no leak of a hydraulic oil leak. The hydraulic Leak test plan is prepared and reviewed as follows:

1. Ensure proper PPE prior to the test.
2. Fill out Job Safety Analysis.
3. Ensure all connections and fittings are in place.
4. Fill the confining chamber with hydraulic oil, ensuring no air is trapped inside the cell.
5. Re-check all connections and potential leak points.

6. Start to pressurize the cell incrementally to 100 [psi], inspect set up and surrounding for potential leakage; if there is a leakage then follow next step.
7. Pressurize in steps of 100 [psi] to 1000 [psi].

Multiple tests are performed to ensure there is no leak of a hydraulic oil leak. At the beginning stage of development, oil mix water comes out this indicates there is a leak through rubber membrane. The possible sources of a leak are loose ASS bolt, rubber membrane cracking, and adjustment of ASS. To overcome those challenges, we use high strength hollow cylindrical rubber and make sure all the bolts are tied well and ASS adjustment is appropriate. If no oil mix water comes out, it confirms that there is no leak. For the other type of leak, we make sure enough axial load is applied and gas kits are placed well in the position. The test is successful and set up is ready for the preliminary experiment. The leakage test confirms the effectiveness of the device for the desired test.

2.4.2 Validation

We have validated the present experimental development by measuring relative permeability of the core sample with different confining pressure and water as a base fluid. Standard ASTM procedures are followed, first, we set a confining pressure with hydraulic pump. Then, the inlet flow regulator is opened to start water flow. The inlet pressure is maintained at the same level throughout the test and flow rate is measured at the outlet. The tests are performed for different convergent and divergent flow, and confining pressure used here from 100 [psi] to 350 [psi]. The detailed procedures of the experiment are mentioned in the section 2.3.2. The results are summarized in Fig 2.7. It shows that there is a gradual decrease in permeability with increasing confining pressure which is expected. Increasing confining pressure from 100 [psi] to 250 [psi] the permeability decreases at $O(10)$. From 250 [psi] to 350 [psi], the permeability has not changed much, so, we did not increase con-

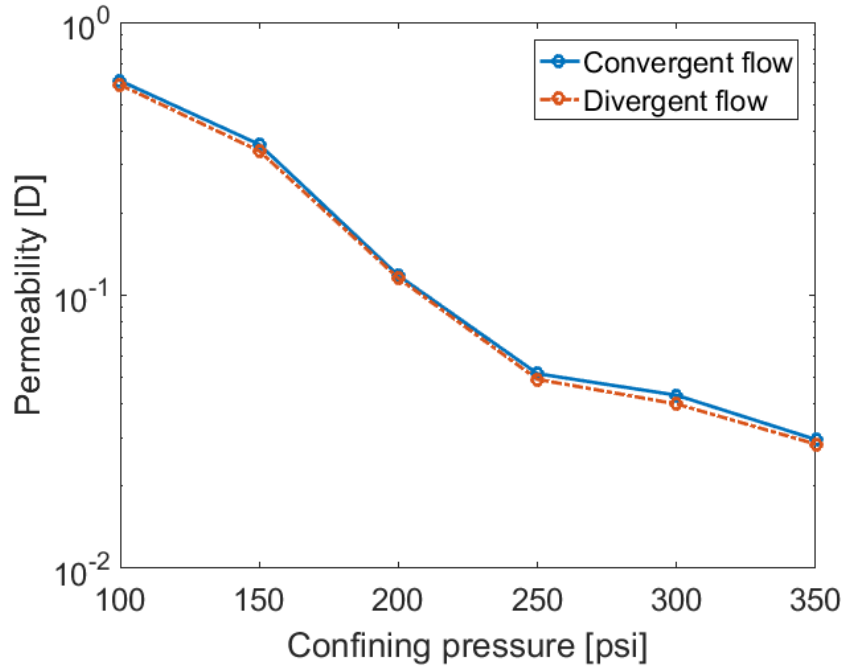


Figure 2.7: Sensitivity of synthetic sample in Permeability at different confining pressure.

fining pressure. This permeability sensitivity test confirms that the device will work as we desire.

2.5 Experimental results

The experiment is performed to study pressure drop at the wellbore with two types of core samples: one is a synthetic sample which is made in a laboratory and another one is real sandstone sample and collected from Nova-Scotia, Canada.

2.5.1 Experiment with synthetic sample

The synthetic core sample is prepared with the dimension so that it fits in the experimental setup. The porosity is measured by following section 2.3.1 and the permeability is

Table: 2.1		
Parameter	Value used for synthetic sample [SI] units	Value used for real sandstone sample [SI] units
r_e	0.0762 [m]	0.0762 [m]
r_w	0.0254 [m]	0.0254 [m]
ϕ	0.30 [-]	0.15 [-]
h	0.3048 [m]	0.3048 [m]
q	0.211 [kg/s]	0.492 [kg/s]
μ	$8.9 \times 10^{-4} [\text{kgm}^{-1}\text{s}^{-1}]$	$8.9 \times 10^{-4} [\text{kgm}^{-1}\text{s}^{-1}]$
ρ	997 [kg/m ³]	997 [kg/m ³]

Table 2.1: Parameter values used in the experimental study for real and synthetic samples.

measured using falling head method apparatus as described in ASTM-D5084 (2010). The parameter's value used in the experiment is listed in the second column of Table 2.1. First, the experimental setup is assembled with the core sample by following section 2.3.2. Then the step-by-step experimental process is followed as described in section 2.3.3. The result is presented in Fig: 2.8. The result shows that initially the wellbore pressure is at atmospheric pressure, and the pressure reaches at about 44[psi] with time, $t = 20[\text{sec}]$. After this time, the pressure becomes almost steady and the pressure is measured for the total time, $t = 180[\text{sec}]$. We have calculated the permeability of the synthetic sample using the collected data with Darcy's law and it is found $\mathcal{K} = 536.0 \times 10^{-15}[\text{m}^2]$.

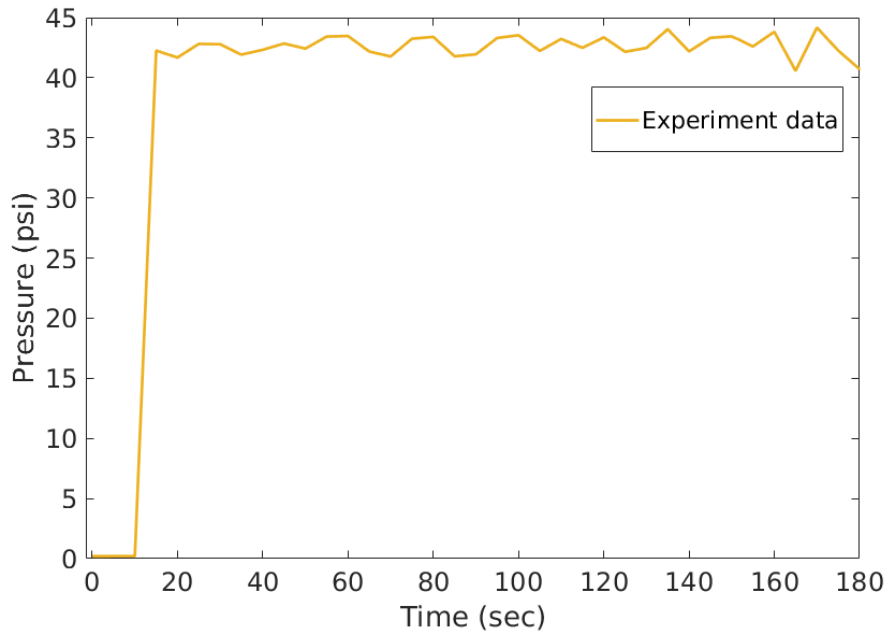


Figure 2.8: Pressure build up test with synthetic sample.

2.5.2 Experiment with real sandstone sample

The core sample from real sandstone is prepared in DTL lab so that it fits in the experimental setup. The porosity and permeability are measured by following the procedure mentioned in section 2.5.1. The parameter's value used in the experiment is listed in the third column of Table 2.1. After accomplishing the experiment with a synthetic sample, the RFC setup is disassembled and the real core sample is assembled by following the steps mentioned in section 2.3.2. Then the step-by-step experimental process is followed as described in section 2.3.3. In this case, the result shows that the pressure reaches at about 102[psi] with time, $t = 40$ [sec]. After this time, the pressure becomes almost steady and the pressure is measured for the total time, $t = 180$ [sec]. The result is displayed in Fig: 2.9. In comparison with a synthetic sample test, real sands sample has taken more time to reach a steady-state level and the wellbore pressure is also higher than the synthetic sample. This

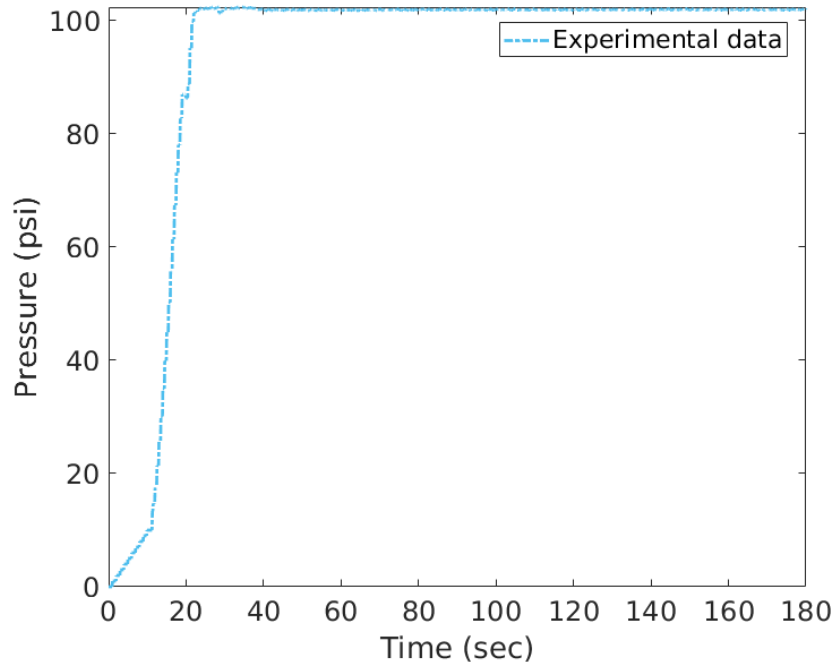


Figure 2.9: Pressure build up test with real sandstone sample.

is because the permeability of the real core sample is smaller than the synthetic sample that is mentioned in Table 2.1.

In addition, after the pressure build-up test, we perform a pressure drawdown test with real sands sample. In this purpose, we stop the inlet flow and keep the outlet flow on. The initial pressure is 102[psi] and the pressure drop is at about 30[psi] within 150[sec] (Fig: 2.10). The permeability of the real sandstone is measured with the experimental data using the Darcy's law and it is found $\mathcal{K} = 95 \times 10^{-15}[\text{m}^2]$. The experiments indicate the present RFC setup is capable to study the flow phenomena near the wellbore with different conditions.

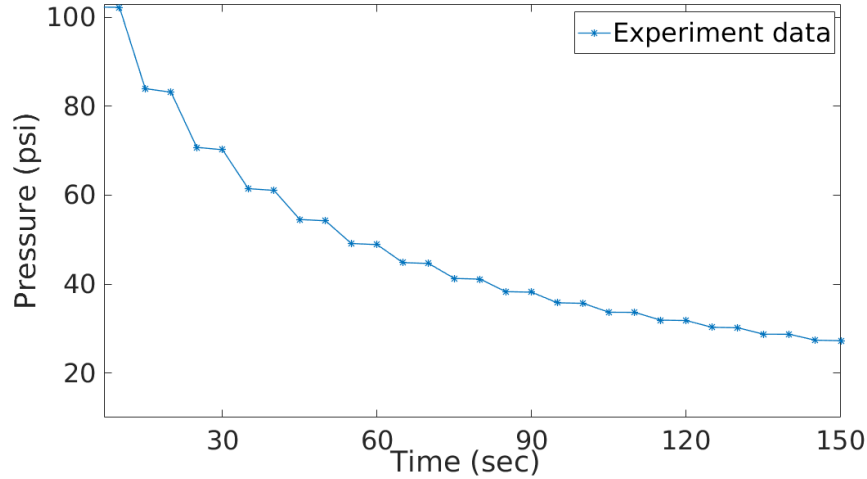


Figure 2.10: Pressure draw down test with real sandstone sample.

2.6 Rationale of the RFC experimental setup

The availability of a radial flow apparatus in the scientific market is limited. The present device has significantly higher capacities of axial load up to 450 [kn], confining pressure up to 3,000 [psi] and cylindrical specimen with 0.1524 [m] diameter and 0.3048 [m] height. Water or oil or other fluid of interest at ambient temperature can be used and it is also capable to handle Newtonian and non-Newtonian fluids. These properties and the following applicable fields make this technology novel in the study of fluid flow in the porous media. This new scientific experimental technology is developed to understand the near-wellbore conditions and reservoir fluid flows. It is possible to predict the direction and rate of flow, as well as determine the type of formation damage and its influence on the hydrocarbon production with this new technology. The scale-up gap is a challenging endeavor in the oil reservoir study, this new apparatus is able to reduce the scale-up gap between laboratory and field data to get the actual scenario of reservoir fluids to flow phenomena compared to available apparatus in the literature (Rahman *et al.*, 2007a). Furthermore, this new technology can be used to assist in the areas of the near-wellbore to far-field flow assurance,

improved and enhanced oil recovery, heat and mass transfer, formation damages and multiphase flow behavior.

2.7 Conclusions and recommendations

The present RFC experimental prototype is validated with synthetic samples prepared in the DTL lab. The experimental investigations provide evidence that the apparatus is capable to simulate near-wellbore flow phenomena. More investigations will confirm the more applicability of this device which is underway in the lab with another research group. This device has a wide range of applications in oil/gas reservoir engineering. The device is able to simulate a larger scale than the existing device in the market with the more applicable field of research. Some of them are mentioned below. Each application has deep scientific interest and long-term goal for the industries.

- Investigation of the characteristics of the various formation zones and formation damage due to different perforation techniques with multiphase flow mechanism.
- Investigation of near-wellbore flow characteristics with multiphase flow mechanism.
- Investigation of formation damage in the near-wellbore environment due to the drilling process.
- The convergent flow facility of this device will help to understand clay sensitivity in the perforated tunnel.
- Effect of drilling mud on the reservoir formation.
- The divergent flow system of this device will help to improve the thermal recovery knowledge in EOR process.

- The flow study near injection well including fine mitigation, injection rate, formation damage during EOR process for the flooding techniques.

Experimental apparatus helps to get the real scenario of a practical problem. A comparatively higher dimension of the parameters are used here, still, the experimental results are not fully free from some limitations. In the experiment, the measurement tools (*i.e* boundary conditions) cannot be placed exactly at the desired position of the domain. The results are also not fully free from mechanical errors. In addition, during the experiment, the quantitative description of flow phenomena can be performed for one quantity at a time and a limited number of points with fixed time instants. Moreover, setting up an experiment for a problem is comparatively more expensive than CFD simulations and all the parameters cannot be changed frequently as like CFD simulations.

Acknowledgments

M. A. Rahman acknowledges financial support from the grant NPRP10-0101-170091 from Qatar National Research Fund (a member of the Qatar Foundation). He also acknowledges financial support from the National Science and Research Council-discovery grant (NSERC-DG), Canada, RDC Ignite, NL and Seed grant Memorial University of Newfoundland, Canada. Ahammad acknowledges School of graduate studies, Memorial University of Newfoundland, Canada for scholarships.

Nomenclature

<i>Symbol</i>	<i>[SI] Units</i>	<i>Description</i>
q	kg/s	Flow rate
r_e	m	Radius of reservoir end
r_w	m	Radius of wellbore
P_w	Pa	Bottom hole pressure
h	m	Hight of the reservoir
t	s	Time
P	Pa	Pressure
\mathcal{K}	m ²	Permeability of the medium
μ	mPa.S	Viscosity of fluid
ρ	Kg/m ³	Density
V_T	m ³	Bulk volume
V_v	m ³	Pore volume
ϕ	---	Porosity of the medium
B	---	Formation volume factor

Abbreviation

ASS	Arc Support Stabilizer
CFD	Computational Fluid Dynamics
CSA	Canadian Standards Association
DTL	Drilling Technology Laboratory
DAQ	Data Acquisition system
EOR	Enhanced Oil Recovery
PPE	Personal Protective Equipment
RFC	Radial Flow Cell

Chapter 3

**A CFD investigation of the flow behavior
near a wellbore using Navier-Stokes
equation**

Title of the article: *A CFD investigation of the flow behavior near a wellbore using Navier-Stokes equations*

Authors: *M Jalal Ahammad*¹, *Mohammad Azizur Rahman*², *Jahrul M Alam*³,
*Stephen D Butt*⁴.

Corresponding author: Mohammad Azizur Rahman; email: marahman@mun.ca

*Journal of Advances Mechanical Engineering (sp. issue) –
Numerical Simulation and Novel Construction Methods in Oil and Gas Engineering,
SAGE Publication, UK (Accepted for the publication – 2019).*

Abstract: The analysis of fluid flow near the wellbore region of a hydrocarbon reservoir is a complex phenomenon. The pressure drop and flow rates change in the near-wellbore with time and the understanding of this system is important. Besides existing theoretical and experimental approaches, Computational Fluid Dynamics (CFD) studies can help understanding the nature of fluid flow from a reservoir into the wellbore. In this research, a near-wellbore model using 3D Navier-Stokes equations is presented for analyzing the flow around the wellbore. Pressure and velocity are coupled into a single system which is solved by an algebraic multigrid method for the optimal computational cost. The CFD model is verified against the analytical solution of the Darcy model for reservoir flow, as well as against the analytical solution of pressure diffusivity equation. The streamlines indicate that the flow is radially symmetric with respect to the vertical plane as expected. The present CFD investigation observes that the motion of reservoir fluid becomes non-linear at the region of near-wellbore. Moreover, this non-linear behavior has an influence on the hydrocarbon recovery. The flow performance through wellbore is analyzed using the inflow

¹Mathematics and Statistics, Memorial University, Canada, A1C 5S7

²Petroleum Engineering, Texas A& M University, Qatar

³Mathematics and Statistics, Memorial University, Canada, A1C 5S7

⁴Process Engineering, Memorial University, Canada, A1C 5S7

performance relations curve for the steady-state and time-dependent solution. Finally, the investigation suggests that the Navier-Stokes equations along with a near-optimal solver provides an efficient CFD framework for analyzing fluid flow in a wellbore and its surrounding region.

Keywords: 3D Navier-Stokes Equations, multi-grid technique, hydrocarbon reservoir, nonlinear flow, near-wellbore reservoir, inflow performance relation.

3.1 Introduction

In the petroleum industry, the fluid flow phenomena at the vicinity of a wellbore are very important since most of the important quantities such as pressure drop, flow rate, formation damage etc. are expected in this region (Dake, 2001). In fact, the flow near a wellbore is more complex than the reservoir region far away from wellbore and could be nonlinear since sudden pressure drop can occur due to natural or artificial fractures or high permeable formation or perforation tunnels (Jin *et al.*, 2012; Molina & Tyagi, 2015). Darcy's equation describes reservoir fluid flow in the regions where the flow phenomena are linear. In contrast, Forchheimer equation describes nonlinear fluid flow through porous media (Firoozabadi & Katz, 1979; Li *et al.*, 2001; Wu *et al.*, 2011; Song *et al.*, 2015). Nonlinear flow behavior in the near-wellbore regions may have a significant influence on oil and gas production of the hydrocarbon reservoir (Rahman *et al.*, 2007c; Song *et al.*, 2015; Ahammad *et al.*, 2018b). Holditch *et al.* (1976) investigated the near-wellbore fluid flow using a model of fractured porous media, and concluded that over prediction of the flow rates happened when the linear equation was considered. Their study also showed that the hydrocarbon production had a fifty percent decline over the life of the well when the nonlinearity of the flow was neglected. Therefore, further research can be performed using 3D Navier-Stokes equations towards the study of near-wellbore fluid flow.

Most of the existing models assume steady-state flow in the study of oil and gas flows of a reservoir (Shi *et al.*, 2005; Chupin *et al.*, 2007). In fact, during the production stage, the flow behavior becomes complex and pressure changes with time which has an influence on the productivity index (Shi *et al.*, 2005; Ding *et al.*, 1999; Byrne *et al.*, 2010). Note that, the productivity index is the relation among the flow rates of a well and pressures of wellbore and reservoir. Moreover, time dependent nonlinear flow has significant influence on the inflow performance which effects the productivity index. Thus, the time dependent models based on the Navier-Stokes equations are more reliable since it covers the detailed physics of the flow including linear and nonlinear flow properties (Shi *et al.*, 2005; Khadivi & Soltanieh, 2014a). Khadivi *et al.* (2013) used Navier-Stokes equations in the modeling of a coupled wellbore-reservoir to study a reservoir of the different layer of formations with an abrupt change in permeability. A brief literature review shows that there is a growing interest to use the Navier-Stokes equations in the field of petroleum industry. Narsilio *et al.* (2009) investigated various reservoir properties using the Navier-Stokes equations. Ahammad *et al.* (2017) studied fluid flows through porous media using the Navier-Stokes equations. Ahammad & Alam (2017) investigated miscible fluid flow through porous media using the Navier-Stokes equations. Therefore, the Navier-Stokes equations can be used to study reservoir flow in order to optimize the hydrocarbon production (Narsilio *et al.*, 2009). Appropriate techniques and algorithms help to accurately solve this model to study flow in hydrocarbon reservoir (Shi *et al.*, 2005).

Recently, Computational Fluid Dynamics (CFD) has attracted many researchers to study the fluid flow in a hydrocarbon reservoir. The availability of high performance multi-core computing resources has made it possible to utilize the Navier-Stokes equations for CFD investigations of some technological aspects of hydrocarbon reservoirs. Byrne *et al.* (2009) studied the fluid flow through a perforated open-hole tunnel of a vertical well using CFD methodology. The formation damage of asymmetric distribution around a well was

simulated with CFD by Byrne *et al.* (2010). Molina & Tyagi (2015) performed a CFD investigation to study the fluid flow for the different formation layers and Frac-Packing zone. Szanyi *et al.* (2018) studied a near-wellbore of a horizontal well for steady-state flow using a pressure-based (segregated) on control volume technique with Navier-Stokes equations. The present investigation explores the some benefits of using 3D Navier-Stokes equations to study pressure drop at the near-wellbore and understand fluid flow phenomena as well. The aim of this research is further advancement of the application of the 3D Navier-Stokes equations with CFD methodology in the field of petroleum industry. In this regards, the results based on NSE will be compared with Darcy and Forchheimer equations.

In the section 3.2.1, we present the important techniques for investigating fluid flow in the vicinity of a vertical wellbore. Notably, the CFD analysis of near-wellbore region requires appropriate mathematical formulations. We briefly outline the mathematical equations for the flow through porous media which represent the near-wellbore flow with necessary boundary conditions in section 3.2.2 and 3.2.3. The sections 3.2.4 and 3.2.5 describe the analytical solution to calculate pressure for steady-state and time-dependent conditions respectively. In section 3.2.6, the potential solution technique to solve the model equation for the flow through porous media based on NSE in the is described. The numerical simulations are analyzed in the results section (sec: 3.4). The model is verified with existing analytical solutions. Finally, the performance of the model is investigated and analyzed with pressure drop and IPR curves studies, and flow direction is studied with streamline behavior and discussed in the numerical results section.

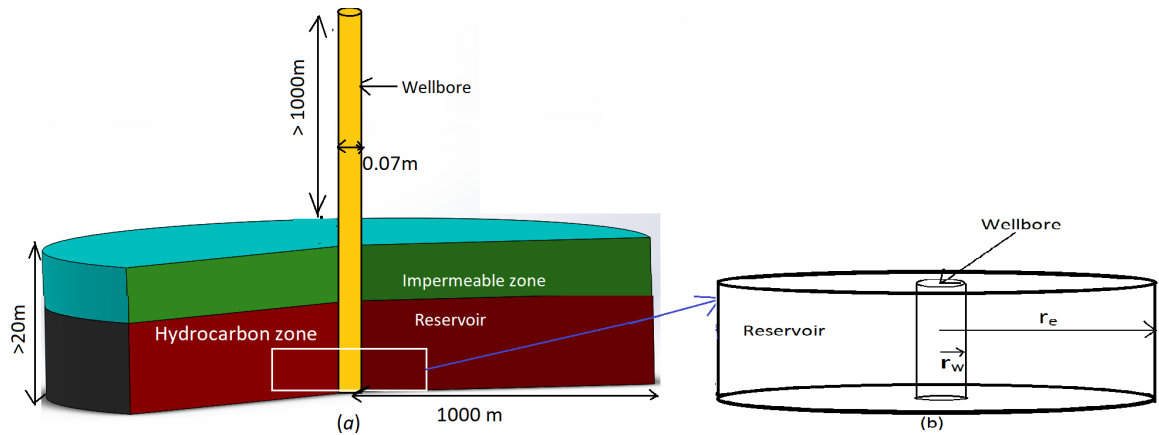


Figure 3.1: (a) A computational design of reservoir along with a vertical wellbore, and (b) the near-wellbore region of a reservoir which is similar to the rest of the simulation in this research.

3.2 Methodology

3.2.1 CFD model setup for near-wellbore simulation

The diagram of a commonly used computational design for a near-wellbore simulation is shown in Fig (3.1). The average length, height, and depth of a hydrocarbon reservoir are 3000[m], 100[m], and 477[m] respectively, (Chupin *et al.*, 2007). To design an effective a near-wellbore model, one needs to consider the reasonable scale of the reservoir; for example, Chupin *et al.* (2007) assumed a length of 350[m], a thickness of 26.7[m] and a depth of 477[m] for a near-wellbore reservoir simulations. Chupin *et al.* (2007) also considered 153 lateral grid blocks for the reservoir of size 3000[m] \times 3000[m] \times 30[m], and 100 grid blocks for a near-wellbore reservoir of size 350[m] \times 350[m] \times 26.7[m]. Thus, a single grid block has the average lateral size of 20[m] for the full scale reservoir, and 3.5[m] for near wellbore

reservoir model. In fact, to capture the real flow, this size is not sufficiently fine because the typical length and diameter of a perforation tunnel is much less than 3.5[m]. Therefore, we need to choose a near-wellbore dimension and grid size so that the near-wellbore flow can be captured. Further, Chupin *et al.* (2007) argued that a sufficient distance of a wellbore from a reservoir should be at least 10[m] to simulate a near-wellbore model since considering larger scale of a reservoir increases computational burden. We consider a near-wellbore with a reasonable scale in this research so that computational cost can be optimized with sufficient smaller grid size. In Fig 3.1(b), r_w and r_e represent wellbore and near-wellbore reservoir radius respectively. The present computational domain can be extended as desired size and shape as convenient, moreover, the formation damage zone around wellbore can be included as well.

3.2.2 Governing equation for flow through porous media

We consider the volume averaged Navier-Stokes equations for slightly compressible flow to investigate the flow behavior in the near-wellbore region of a reservoir as (see, Szanyi *et al.* (2018); ANSYS (2016); Azadi *et al.* (2017); Ahammad & Alam (2017)):

$$\frac{\partial \rho}{\partial t} + \frac{\partial(\rho u_j)}{\partial x_j} = 0, \quad (3.1)$$

$$\rho \left(\frac{\partial u_i}{\partial t} + u_j \frac{\partial u_i}{\partial x_j} \right) = -\frac{\partial P}{\partial x_i} + \frac{\partial \tau_{ij}}{\partial x_j} + \rho g_i + \mathcal{F}_i, \quad (i, j = 1, 2, 3), \quad (3.2)$$

where $\tau_{ij} = \mu \left(\frac{\partial u_i}{\partial x_j} + \frac{\partial u_j}{\partial x_i} \right)$ and \mathcal{F}_i is a combination of Darcy and Forchheimer model for flow through porous media. Note that, the Forchheimer term represents pressure changes due to the inertial force (*i.e.* nonlinear flow) which is dominant in the near-wellbore region. According to a brief literature review, we see the near-wellbore flow has a nonlinear tendency (Firoozabadi & Katz, 1979; Li *et al.*, 2001; Wu *et al.*, 2011; Song *et al.*, 2015). The

total momentum sink is accounted by

$$\mathcal{F}_i = -\frac{\mu}{\mathcal{K}}u_i - \beta\frac{\rho}{2}|\mathbf{u}|u_i, \quad (3.3)$$

where the loss coefficient β is modeled as $\beta = \frac{17.2 \times 10^{10}}{\mathcal{K}^{1.76}}$ (see for details, Khaniaminjan & Goudarzi (2008)).

3.2.3 Boundary conditions

As shown in Fig 3.1(a), we consider a near-wellbore region for the present CFD simulations. The outer boundary is the inlet and the outlet at the wellbore surface. The inlet boundary condition of the present CFD simulation is

$$P(r_e, t) = P_0, \text{ for all time } t \geq 0. \quad (3.4)$$

The outlet boundary condition is

$$r\frac{\partial P}{\partial r} = \frac{q\mu}{2\pi\mathcal{K}h}, \text{ for all time } t > 0, \text{ at } r = r_w \quad (3.5)$$

where q is constant flow rate. In other words, pressure-inlet and flow rate-outlet are considered to satisfy mass conservation.

The initial pressure in the reservoir is set to be uniform, thus,

$$P(r, 0) = P_0, r_w \leq r \leq r_e. \quad (3.6)$$

Top and bottom layers of the computational domain are considered as wall, so no flow boundary condition is used on those boundaries. Note that, these boundary conditions are proposed according to numerical tests so that the CFD model remains consistent with the traditional reservoir model.

3.2.4 Analytical solutions of traditional models to validate CFD simulation

In the following subsection, we recall the analytical solutions of the Darcy equation and pressure diffusivity equation to validate the CFD simulations of the present research.

3.2.4.1 Pressure calculation using Darcy model

Assuming the flow is steady-state, and linear from reservoir end to wellbore surface, then classical Darcy model has the form

$$\frac{\partial P}{\partial x_i} = -\frac{\mu}{\mathcal{K}}u_i, i = 1, 2, 3. \quad (3.7)$$

Here, the flow is assumed in the radial direction, and the reservoir is isotropic, so eqn (3.7) can be written in polar coordinate as

$$\frac{\partial P}{\partial r} = -\frac{q\mu}{2\pi r\mathcal{K}h}, \quad r \in [r_w, r_e]. \quad (3.8)$$

Integration of eqn(3.8) leads to the analytical solution of Darcy equation for a steady state condition as (Economides, 2013)

$$P = P_w + \frac{q\mu}{h\mathcal{K}} \ln \left(\frac{r}{r_w} \right), \quad (3.9)$$

where r, r_w, P_w, P and h is the reservoir radius, wellbore radius of the reservoir, wellbore pressure, reservoir pressure and height of the reservoir respectively. Converting to oilfield units, where P and P_w are in [psi], q is in [STB/d], μ is in [cp], \mathcal{K} is in [mD], h is in [ft], and B is the formation volume factor to convert STB into bbl, in that case eqn (3.9) becomes (Economides, 2013)

$$P = P_w + 141.22 \frac{Bq\mu}{h\mathcal{K}} \ln \left(\frac{r}{r_w} \right). \quad (3.10)$$

3.2.5 Pressure calculation using pressure diffusivity equation

As we assume that flow occurs in radial direction and the mass conservation equation for radial flow with true velocity is

$$\frac{\partial}{\partial t}(\phi\rho) + \frac{\partial}{r\partial r}(ru\rho) = 0. \quad (3.11)$$

Darcy equation can be combined with mass conservation equation to obtain pressure diffusivity equation (PD). Thus, combining Darcy equation e.g. eqn(3.7) with the mass conservation eqn(3.11), one dimensional diffusivity equation for slightly compressible fluid takes the form as (Rahman *et al.*, 2007c; Razminia *et al.*, 2014)

$$\frac{\partial^2 P}{\partial r^2} + \frac{1}{r} \frac{\partial P}{\partial r} + c_r \left(\frac{\partial P}{\partial r} \right)^2 = \frac{\phi\mu c_t}{\mathcal{K}} \frac{\partial P}{\partial t}, \quad (3.12)$$

where total compressibility c_t is the sum of rock and fluid compressibility $c_r = \frac{1}{\phi} \frac{\partial \phi}{\partial P}$ and $c_f = \frac{1}{\rho} \frac{\partial \rho}{\partial P}$ respectively. The solution of this equation describes pressure at any location, r , at any time, t , within the domain. This is a nonlinear partial differential equation and difficult to solve for an analytical solution. For simplification, one can neglect the nonlinear term in eqn (3.12) by considering pressure variation is small (Azin *et al.*, 2017), then the eqn (3.12) becomes

$$\frac{\partial^2 P}{\partial r^2} + \frac{1}{r} \frac{\partial P}{\partial r} = \frac{1}{\chi} \frac{\partial P}{\partial t}, \quad (3.13)$$

which is known as the pressure diffusivity equation in reservoir studies, where $\chi = \frac{\mathcal{K}}{\phi\mu c_t}$. Under the following assumptions pressure can be calculated analytically from PD. The reservoir is isotropic and homogeneous in all directions, well produces at constant flow rate, the radius of the well is negligible compared to reservoir, the reservoir has uniform initial pressure, and the well drains an infinite area (i.e., $P \rightarrow P_0$ as $r \rightarrow \infty$). Under these conditions, pressure can be calculated from the eqn (3.13) as

$$P(r, t) = P_0 - \frac{q\mu}{4\pi\mathcal{K}h} \ln \left(\frac{2.25t\chi}{r^2} \right).$$

Now converting the variables in oilfield units and above equation becomes (Economides, 2013)

$$P(r, t) = P_0 - \frac{162.6Bq\mu}{Kh} \left(\log_{10} \left(\frac{t\chi}{r^2} \right) - 3.23 \right). \quad (3.14)$$

3.2.6 Solution technique of NSE for petroleum industry

CFD simulation requires to approximate the model equation with the suitable discretization technique. In this research, a higher resolution scheme based on the upwind method is used for the spatial discretization and implicit backward Euler scheme is used for the time integration since it is unconditionally stable (Pletcher *et al.*, 2013). Mesh generation is important in CFD simulations since capturing the physics of flow, accuracy and convergence depend on mesh size and time step (Pletcher *et al.*, 2013). The meshing tools in *ANSYS CFX v17.2* is used to generate 3D mesh in both reservoir and wellbor in this research. The velocity-pressure coupling solver on collocated grid arrangement is used in this research where the system of equations is solved using an algebraic multigrid technique. In other words, after discretization, a single large system of equation is simultaneously solved for all variables. Algebraic multigrid technique help to transform a system of discrete equations for a coarse mesh by summing the finer mesh equations. The process is performed on virtual grid cells during the iterations and re-refine the mesh to obtain an accurate solution. This technique is less expensive with higher convergence rates since the discretization of the nonlinear equations is solved only once on finer mesh (Pletcher *et al.*, 2013). The algorithm is implemented in *ANSYS CFX* software and verified for the purposes other than porous media. The advantage of this algorithm is utilized in the current research. The flow chart of the solution process of the transient problem is exhibited in the Fig (3.2).

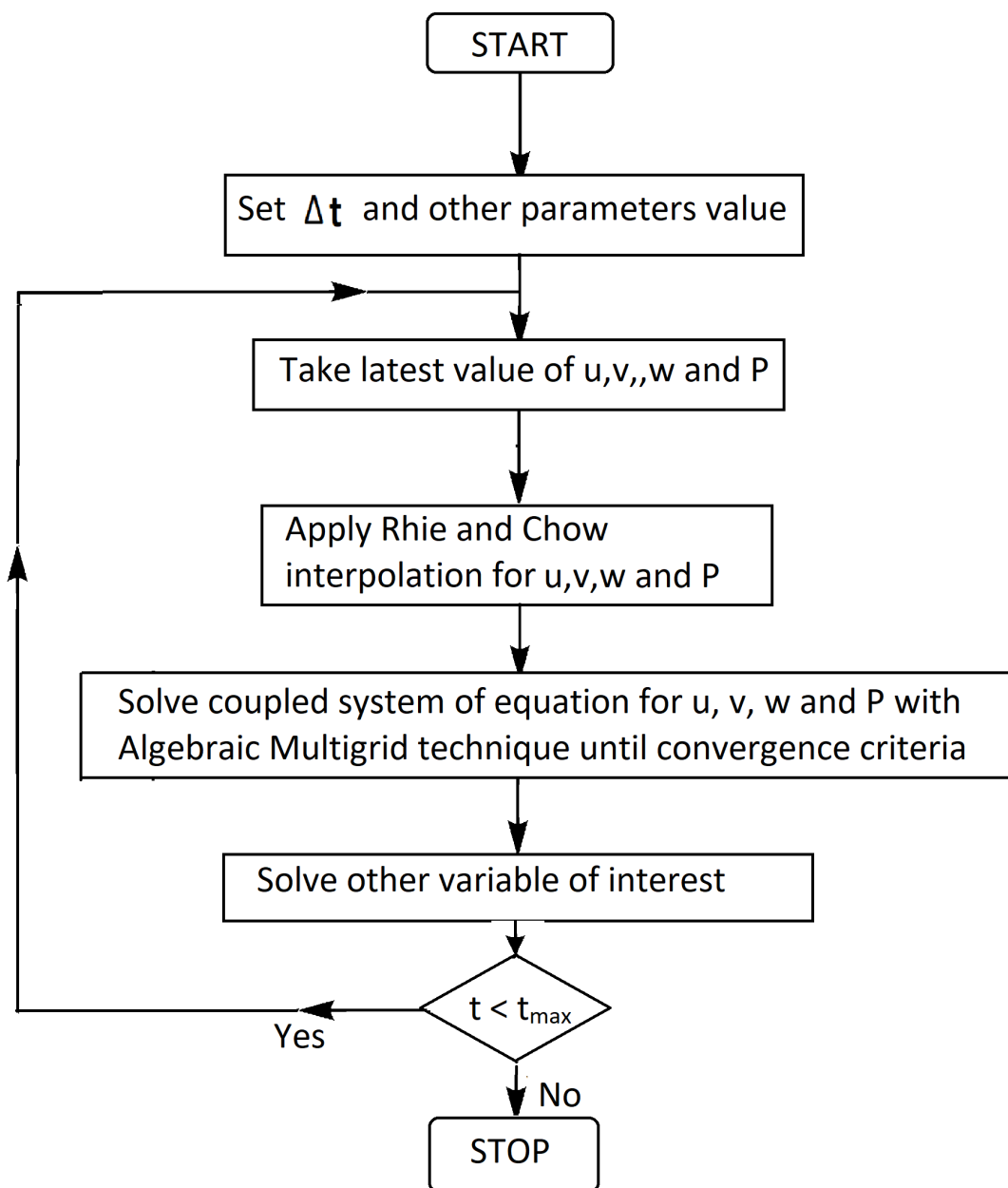


Figure 3.2: Flow chart for pressure based coupled solver.

3.3 Inflow performance relationship formulation

The present near-wellbore model based on Navier-Stokes equations is expected to perform as like other models such as pressure diffusivity equation. We study the Inflow Performance Relationship (IPR) with the present numerical solutions using NSE. The IPR is defined as the relationship between the well production rate and flowing pressure of the well. It has importance to the production engineers since depending upon this relation they have to adjust the pressure at separator or pipeline junction (Economides, 2013). The IPR curves can be three types: steady-state, transient, and pseudo-steady-state. The IPR curves calculated by the present simulations will be compared to the analytical solution. First, we derive IPR formulation with the parameters listed in table (3.1) for linear ($\beta = 0$) flow simulations model. After utilizing the parameters value in eqn (3.10), the IPR curve for steady-state with no skin effect stands as

$$P_w = 1200 - 0.84q. \quad (3.15)$$

Now, deploying the parameters value from table (3.1) to eqn (3.14) for nonlinear flow ($\beta = 2.3271 \times 10^8 [\text{m}^{-2}]$) phenomena, the IPR curve of time dependent model equation for nonlinear flow with no skin effect becomes

$$P_w = 1200 - \frac{q}{3.46} (\log_{10} t + 5.75). \quad (3.16)$$

3.4 Numerical results and discussions

3.4.1 Validation of CFD simulation against Darcy model

The CFD simulation is performed for a near-wellbore region with Navier-Stokes equations for steady-state condition. The performance of CFD result is verified with the analytical solution of the Darcy equation (i.e. eqn(3.10)). Parameters value for this simulation are

Table 3.1		
Parameter	Value [SI units]	Value [oilfield units]
r_e	1.0668 [m]	3.5 [ft]
r_w	0.0381 [m]	0.125 [ft]
P_0	1200 [psi]	8.273709×10^6 [pa]
P_w	800 [psi]	5.516×10^6 [pa]
\mathcal{K}	250×10^{-15} [m ²]	0.9869×250 [mD]
ϕ	25 % [-]	0.25 [-]
h	0.6096 [m]	2 [ft]
q	0.872 884 [kg/s]	474.36 [bbl/day]
μ	8.9×10^{-4} [kgm ⁻¹ s ⁻¹]	0.89 [cP]
ρ	997 [kg/m ³]	62.24 [lb/m ³]
β	2.3271×10^8 [m ⁻²]	7.09×10^7 [ft ⁻²]

Table 3.1: Parameter values used in the analytical and simulations through out the article.

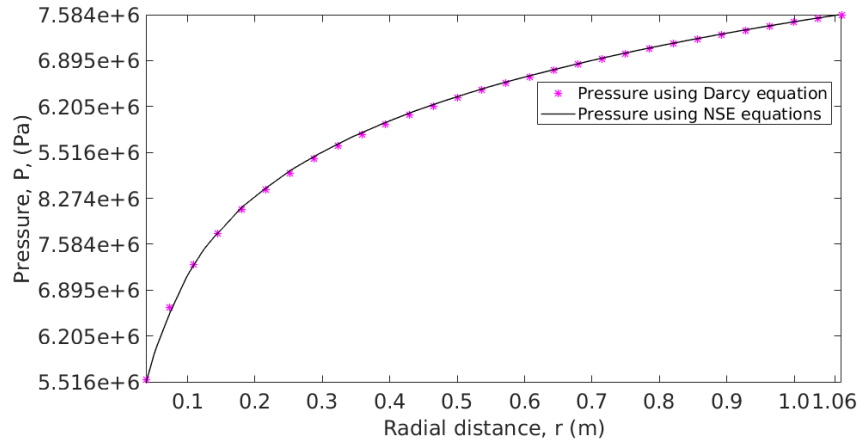


Figure 3.3: Validation of CFD model based on Navier-Stokes equations for linear model ($\beta = 0$) with the analytical solution of Darcy equation for steady-state flow.

listed in table 3.1 where water temperature is 25°C . In addition, we choose $\beta = 0$ so that inertia force is turn off in Navier-Stokes equations (eqn 3.2) to make consistent with the Darcy model. Pressure profile is calculated from the present model and compared with the analytical solutions of the Darcy model (see, Fig 3.3). Both solutions have a very good agreement and the relative error is very small to distinguish both solutions. Thus, some data points of both solutions are measured with error analysis. The analysis indicates that the present model has a very close consistent result to the analytical solution with a maximum error of 0.45%. This result indicates that the present model setup can be used to describe the underlying physics of fluid flow in a near-wellbore reservoir.

3.4.1.1 Comparing CFD simulations against the pressure diffusivity equation

Here, we compare the pressure which is calculated using Navier-Stokes equations for current numerical simulations with the analytical solution of PD. The parameters value for the simulations are listed in table 3.1. The pressure are calculated using Navier-Stokes equa-

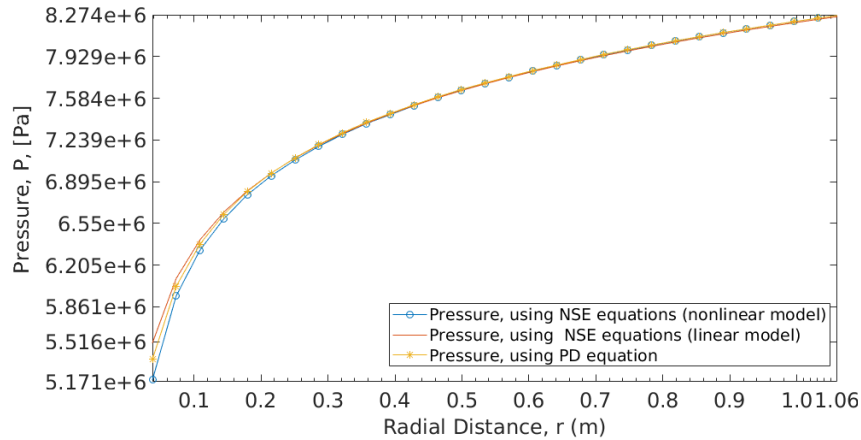


Figure 3.4: Comparison of pressure distributions calculated by NSE equations, and analytical solution of PD equation for nonlinear ($\beta = 2.3271 \times 10^8 [\text{m}^{-2}]$) and linear ($\beta = 0$) *i.e.* Darcy model.

tions for nonlinear ($\beta = 2.3271 \times 10^8 [\text{m}^{-2}]$) and linear ($\beta = 0$) models, and are compared with the analytical solution of PD equation. The pressure profiles are drawn along the radial distance of the reservoir and presented in Fig (3.4). The results indicate that the pressure drop with respect to radial distance has a good match except at the wellbore region. We notice that the differences of pressure drop at the wellbore between linear model *i.e.* without inertia force and nonlinear *i.e.* with inertia force is about 344738 [Pa] \simeq 50 [psi]. In addition, the difference of pressure drop between the analytical solution of pressure diffusivity equation and NSE equations with the nonlinear term is about 172369 [Pa] \simeq 25 [psi]. The deflection of pressure drop compared to the linear and nonlinear model using the Navier-Stokes equations, and the analytical solution of the PD equation may be the cause inertia force *i.e.* nonlinear term. We see in the Darcy equation – flow rate is linearly dependent with pressure drop and the analytical solution of PD is obtained by dropping the nonlinear term. This is the reason of deflection of pressure near the wellbore. This investigation indi-

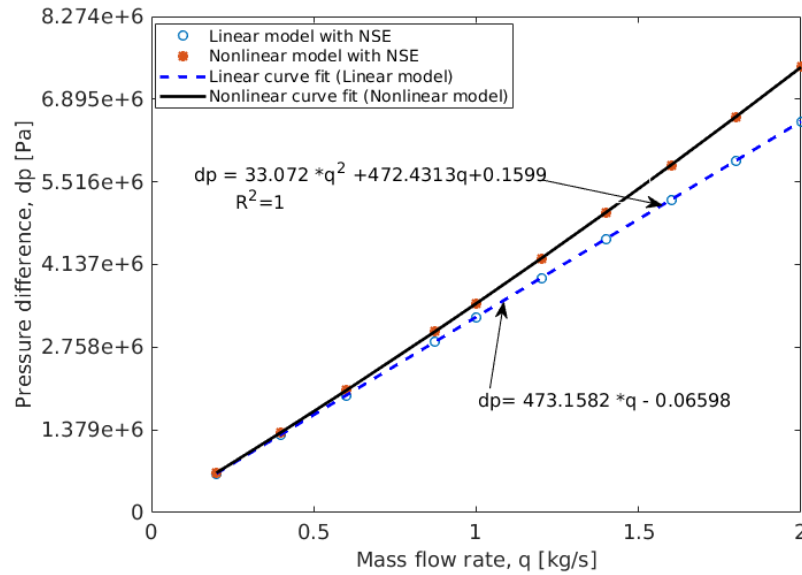


Figure 3.5: Comparison of pressure drop as a function of flow rate at the wellbore surface where $\beta = 2.3271 \times 10^8 [\text{m}^{-2}]$ and $\beta = 0$ for nonlinear and linear model respectively.

icates that the NSE with efficient CFD technique in the study of reservoir flow is promising.

3.4.2 Flow characteristic at the near wellbore

In this section, we discuss the fluid flows phenomena at the near-wellbore region for different flow rates scenarios.

3.4.2.1 Flow behavior at near-wellbore region

The flow phenomena at the near-wellbore of an idealized reservoir are investigated with different flow rate scenarios considering linear and nonlinear flow models. Here, $\beta = 2.3271 \times 10^8 [\text{m}^{-2}]$ is considered for nonlinear model and $\beta = 0$ for linear model with the variation of flow rate, q . Pressure drop is calculated at the wellbore surface for dif-

ferent flow rates in both cases. Generally, the pressure drop occurs at the near-wellbore and the mean flow of a reservoir fluid is along the radial direction which causes fluid velocity to increase continuously at wellbore region (Jin *et al.*, 2012). The same behavior is observed in the present simulation. The pressure difference data are plotted with respect to flow rates and presented in Fig (3.5) for both linear and nonlinear flow models with least square curve fitting process. To investigate the nature of the relation of pressure drop with flow rate the polyfit tool is used for the curve fitting process in Matlab code while plotting the simulations data in Fig (3.5). A quadratic curve is well fitted with the data for nonlinear flow whereas a curve with degree one is fitted with the linear flow. Eqn (3.3) with $\beta = 2.3271 \times 10^8 [\text{m}^{-2}]$ is nonlinear and the curve fitting equation, $dp = 33.072q^2 + 472.4313q + 0.1599$ with $R^2 = 1$, is also nonlinear. On the other hand, eqn (3.3) with $\beta = 0$ is considered as Darcy flow which is linear and curve fitting equation, $dp = 473.1582q - 0.06598$ with $R^2 = 1$, is also linear. Note that, when the flow rate is small linear and nonlinear models have the same behavior and the difference is noticeable for a higher flow rate. The CFD results with the value of the prescribed parameter indicate that the relationship between pressure drop and flow rate remains linear until the mass flow rate reaches 0.6 [kg/s]. After that, the relation between flow rate and pressure drop is visible *i.e.* linear and nonlinear. This analysis indicates NSE can explain fluid flow phenomena at the near-wellbore region. This investigation helps production engineer and well management with more ideas of flow behavior near-wellbore region in that case of linear or nonlinear. The pressure drop at the wellbore depends greatly on the well flow rate and the life of the reservoir depends on the optimum production rate. Over time, the flow and pressure decreasing rates depend upon the various reservoir parameters. This study focuses on the near-wellbore flow phenomena where the flows are mostly nonlinear. We see the pressure drop increases with time for both linear and nonlinear flows Fig (3.6). The prediction of pressure drop by linear flow model at the early time is about 6.378×10^6 [Pa] \simeq 925 [psi]

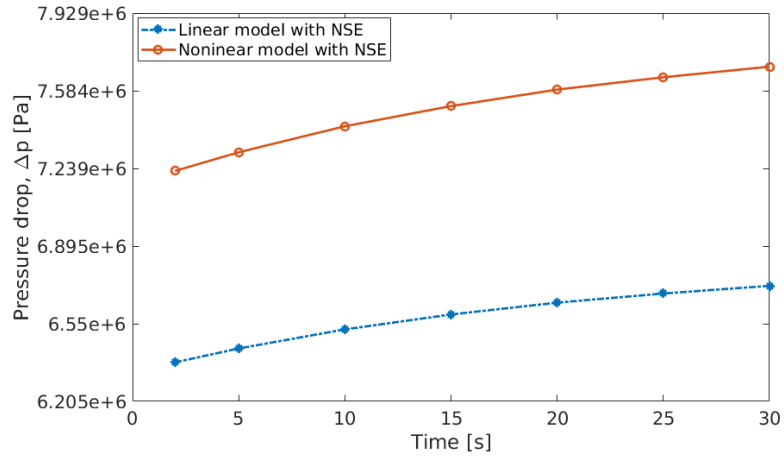


Figure 3.6: Pressure drop analysis at the near-wellbore with linear $\beta = 0$ and nonlinear models ($\beta = 2.3271 \times 10^8 [\text{m}^{-2}]$).

whereas $7.2395 \times 10^6 [\text{Pa}] \simeq 1050 [\text{psi}]$ for the nonlinear model. The trend continues until the final time of the simulations and at the end, the difference of pressure drop between the two models is $8.619 \times 10^5 [\text{Pa}] \simeq 125 [\text{psi}]$. This indicates that the flow rates at the near-wellbore will be decreased gradually over the production period and it will be more for the nonlinear model compared to linear model – this information supports the findings of Wang & Sheng (2017).

3.4.2.2 Flow direction

Here, we consider nonlinear model with $\beta = 2.3271 \times 10^8 [\text{m}^{-2}]$ to investigate the flow pressure pattern and flow direction. Streamlines may give a more detailed description of mass flow across the wellbore region since they provide information both on the magnitude and direction of flow velocity at a given point in time. The streamlines are plotted along a vertical plane of the reservoir and presented in Fig: (3.7). We see the magnitude of the velocity is higher at the near-wellbore compare to the reservoir end. The fluid velocity is

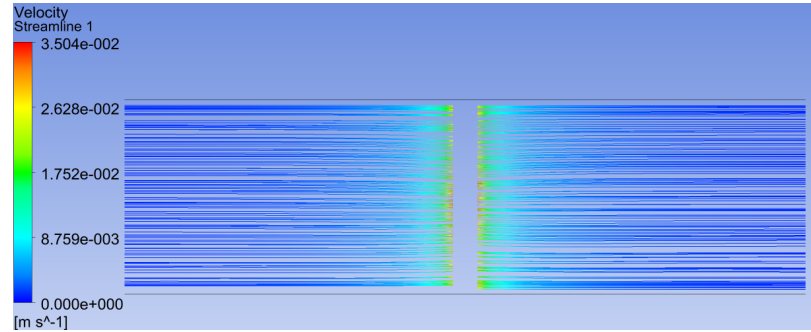


Figure 3.7: The streamlines along a vertical cross section of the domain representing flow direction.

gradually increasing from the reservoir end to the wellbore region. This indicates the fluid is flowing in a constant flow rate to the radial direction of the reservoir.

3.4.3 Inflow performance relation analysis

In this section, we consider linear and nonlinear model based on Navier-Stokes equations to investigate the inflow performance at the near-wellbore. The inflow performance relation is investigated for two scenarios: linear and nonlinear flow models. First case, we consider CFD simulations for linear model $\beta = 0$ using NSE and the results are compared with the analytical solutions (*i.e.* eqn(3.15)). We find that the IPR curve generated from CFD solution has a good agreement until flow rate $q = 0.92007$ [kg/s] $\simeq 500$ [bbl/day]. Further, the deflection is noticed for the higher flow rate, *i.e.* $q = 1.10408$ [kg/s] $\simeq 600$ [bbl/day], in this case, the decline pressure is about 137895 [Pa] $\simeq 20$ [psi] which is 3% (see, Fig:3.8(a)). In the second case, we investigate the application of the proposed CFD model based on Navier-Stokes equations for the nonlinear model for inflow performance analysis. Three-time durations: $t = 0.003$ [hrs], 0.008 [hrs] and 0.014 [hrs] are taken into account for the present study. Following eqn (3.16), the time-dependent IPRs are calculated and then com-

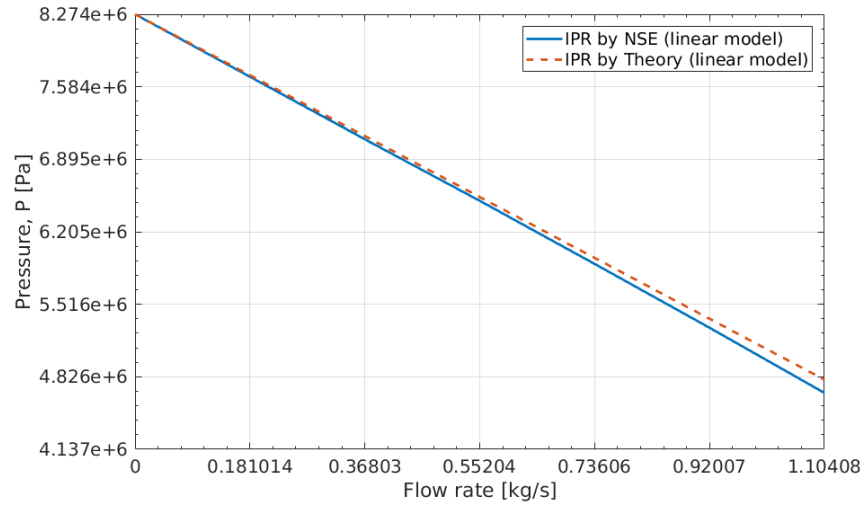
pared against the present CFD data (see, Fig:3.8(b)). The transient IPR curves for present CFD simulations have a very good agreement with the theoretical results. There is only a slight deflection for higher flow rate ($q = 1.10408$ [kg/s] \simeq 600 [bbl/day]) at the final time 0.014 [hrs] which about 3.7% difference of pressure and this reasonable. Thus, the simulation time 0.008 [hrs] can be the optimal time duration for a flow to be steady-state in the present idealized reservoir condition. The proposed CFD modeling based on Navier-Stokes equations can be used for better determination of the future behavior of a reservoir and can explain the various production scenarios of a reservoir and help production engineering to maintain the pressure at separator or transport pipeline.

3.4.4 Pressure distribution analysis using NSE

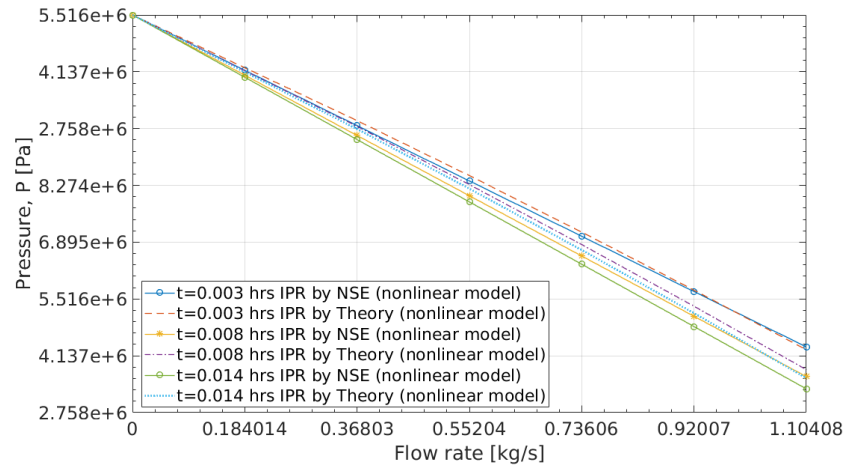
The CFD modeling based on Navier-Stokes equations delivers the promising results, including pressure and velocity distribution in the near-wellbore model as well as three-dimensional flow patterns. In this section, we discuss the characteristics of pressure distribution for different conditions such as flow rates. The pressure distribution help understand the process of reservoir fluid flow through a reservoir to the wellbore.

3.4.4.1 Different flow rates for linear flow model

The pressure distribution for linear flow model ($\beta = 0$ in model equation) is studied for three different flow rates such as ($q = 0.36803$ [kg/s], 0.73606 [kg/s], and 1.10408 [kg/s]) in the case of steady-state condition. The pressure contours for each case is plotted along a vertical plane, *i.e.* $y = 0$ and the results are exhibited in Fig (3.9). The pressure at the reservoir ends is gradually decreasing towards around the wellbore. This means that the reservoir fluid is gradually moving to the wellbore. To quantify the pressure drop at the wellbore, we draw pressure profiles for three cases along a horizontally mid-line of the



(a)



(b)

Figure 3.8: Comparison of the IPR curves: (a) steady-state IPR curves with theory, (b) time dependent IPR curves with theory.

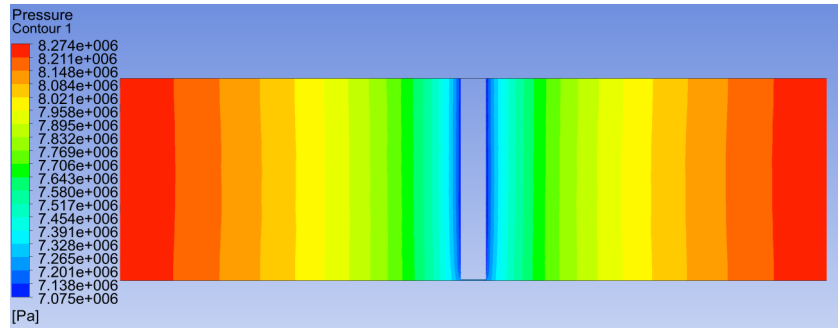
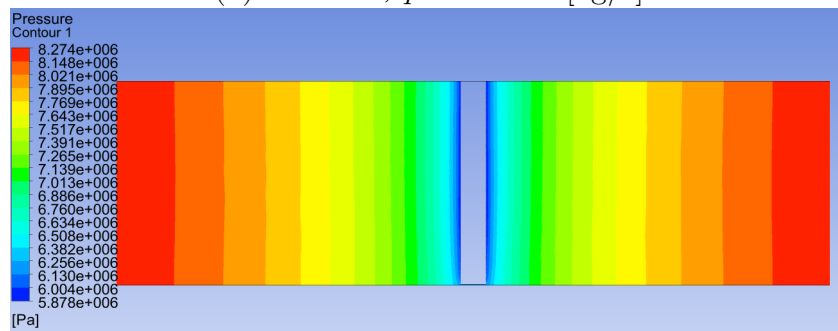
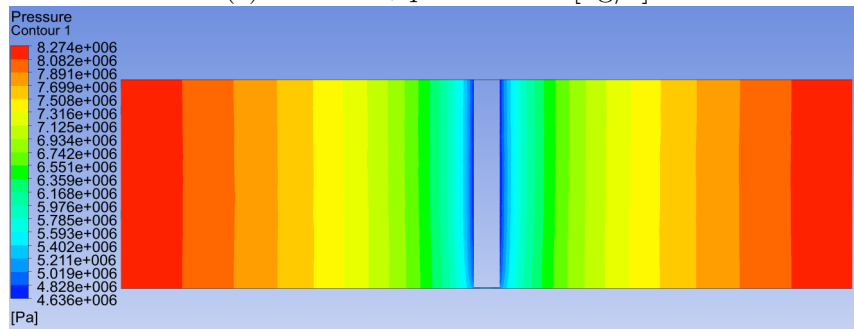
(a) Flow rate, $q = 0.36803$ [kg/s](b) Flow rate, $q = 0.73606$ [kg/s](c) Flow rate, $q = 1.10408$ [kg/s]

Figure 3.9: Contour plots of pressure distribution along a vertical plane of the reservoir for steady-state linear model ($\beta = 0$) condition at different flow rates.

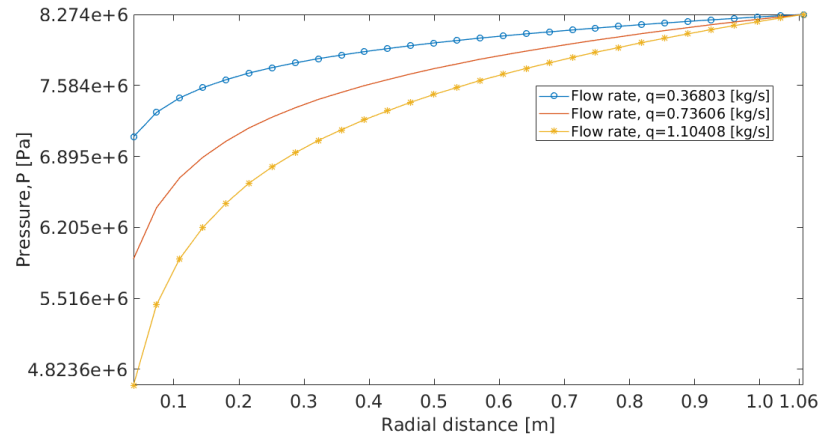


Figure 3.10: Pressure profiles for different flow rates of steady-state linear model ($\beta = 0$) simulations.

reservoir (Fig 3.10). We see that there is a pressure drop about 7.075×10^6 [Pa] for the flow rate of 0.36803 [kg/s], 5.878×10^6 [Pa] for flow rate 0.73606 [kg/s] and 4.636×10^6 [Pa] for flow rate 1.10408 [kg/s]. The results show that pressure drop increases for higher production rate, this means for higher production of a well will reduce the reservoir life. Furthermore, the pressure distribution in the near-wellbore shows that the pressure gradient is adverse in the near-wellbore which indicates the sudden changes in the velocity field. The results indicate that velocity increases at the near-wellbore for the high flow rate compared to low flow rate. This argument supports the sudden pressure drop at the wellbore region. This is the sign of turbulent flow at the wellbore for high flow rate and we have to use Non-Darcy model to study flow in wellbore. The pressure variation along the axial direction of the wellbore is explained in the next chapter.

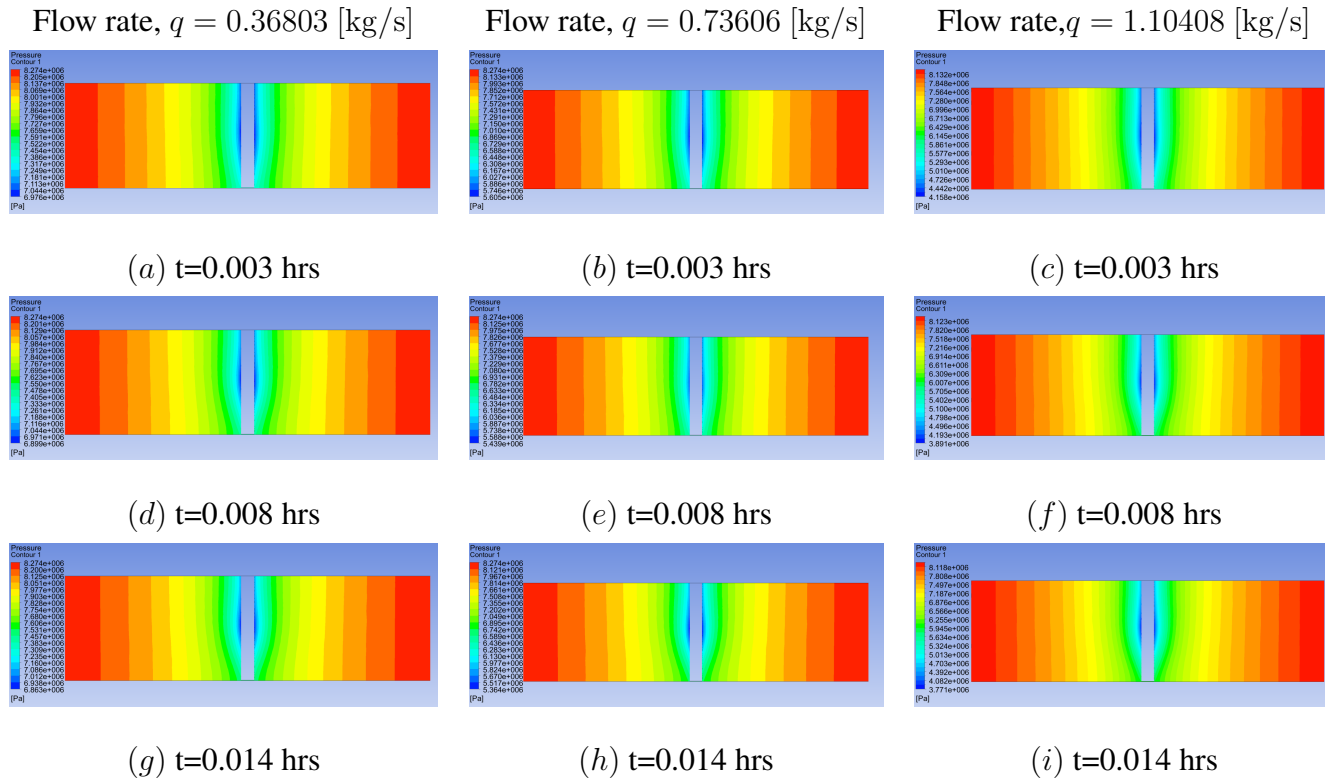
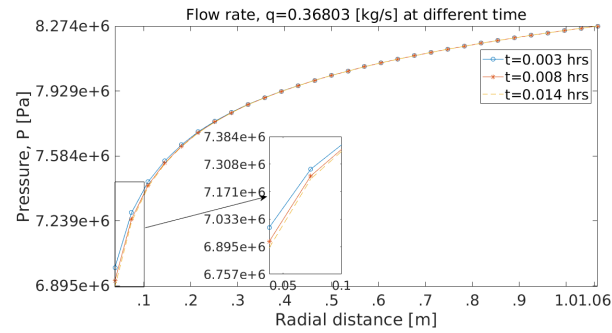
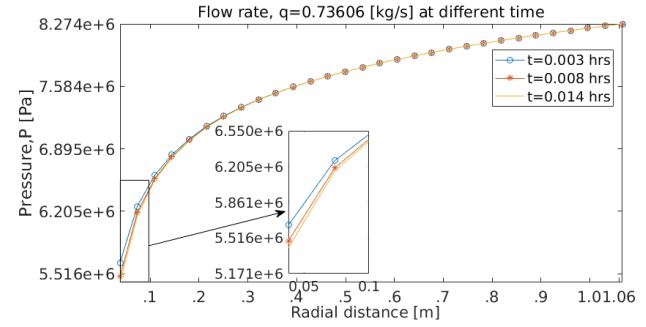


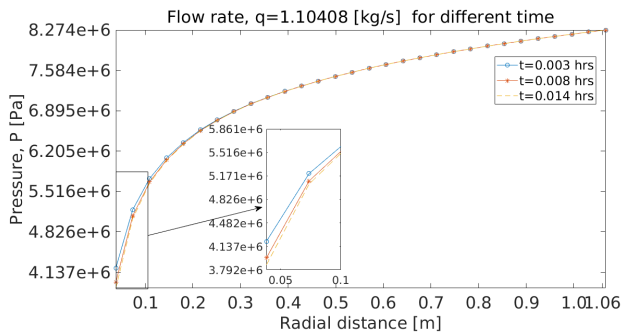
Figure 3.11: Pressure distribution contour plot along a vertical plane for different flow rates for the simulations of nonlinear model ($\beta = 2.3271 \times 10^8$ [m⁻²]).



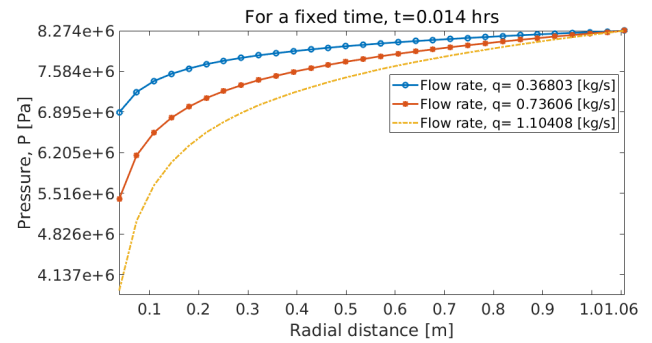
(a)



(b)



(c)



(d)

Figure 3.12: Pressure distributions as a function of radial distance to the wellbore for non-linear flow model ($\beta = 2.3271 \times 10^8 [\text{m}^{-2}]$). (a) For the flow rate, $q = 0.36803 [\text{kg/s}]$, (b) For the flow rate, $q = 0.73606 [\text{kg/s}]$, (c) For the flow rate, $q = 1.10408 [\text{kg/s}]$ and (d) For the fixed time $t = 0.014 \text{ hrs}$ with different flow rates.

3.4.4.2 Different flow rates for nonlinear flow model

In this section, we study the influences of production rates and production time on the fluid flows of a reservoir and pressure drop at the near-wellbore using the nonlinear model ($\beta = 2.3271 \times 10^8 [\text{m}^{-2}]$) with NSE. Here, we also consider three different flow rates (0.36803 [kg/s], 0.73606 [kg/s], and 1.10408 [kg/s]). We plot pressure contour of each case of flow rate for three time intervals: 0.003 [hrs], 0.008 [hrs] and 0.014 [hrs]. The influences of production rates are as the same as the linear model but more pressures drop occur for the nonlinear model. The pressure drop at the near-wellbore is decreasing with respect to time increases for all three cases (Fig 3.11). This means that the reservoir fluid is gradually moving to the wellbore with time runs. In Fig (3.11), the pressure changes are only visible in the legend of the contour plots. We draw pressure profiles for all cases of simulations presented in Fig (3.11) along the mid-line of the reservoir. The results are displayed in Fig (3.12) with zoom in for more visibility of the differences. We notice two features in all cases: pressure drops gradually near the wellbore and it converges with the increases of time. Furthermore, when the flow rate increases the pressure drop near the wellbore is higher than the less flow rate Fig (3.12)(d). This pressure drop at the near-wellbore indicates that the velocity at the near-wellbore increases for the higher flow rate compared to low flow rate. This supports the accurate pressure calculation in the study of reservoir fluid flows using NSE equations.

Finally, we follow that higher pressure drop occurs for the higher flow rate. This indicates to the production engineers that more attention needs to be drawn to maintain optimal pressure at all stages. This is the sign of turbulent flow at the wellbore for high flow rate and nonlinear model is more suitable to study flow at near-wellbore.

3.5 Conclusion and future work

This study investigates modeling of fluid flows phenomena around the near-wellbore of a reservoir using 3D Navier-Stokes equations. The pressure based velocity-pressure coupled solver is used to get a robust, accurate numerical solution of NSE. We verify the present model with existing analytical solutions and other models. Then, we study the nature of the fluid flows around the near-wellbore for a steady-state and time-dependent solution. In this study, we extensively investigate the flow behavior near the wellbore with pressure, stream-lines and IPR curve analysis. This study will help to understand the pressure drop near the wellbore for different flow scenarios and the IPR utility in solving everyday production problems and confirm the possibility of time-dependent IPR curves. Time-dependent IPR curves are dependent on the production history so it helps for future forecasting of the reservoir life. The extension of this model is under process to study the formation damage with different skin zones using coupled wellbore-skin-reservoir approach and transient flow analysis at the near-wellbore of a reservoir. The different layers of a reservoir can be included in the new model. In addition, the model can be extended for a horizontal well with formation damage and other features such as sand control.

Acknowledgments

J. Alam acknowledges financial support from the National Science and Research Council (NSERC), Canada. M. A. Rahman acknowledges financial support from the National Science and Research Council-discovery grant (NSERC-DG), Canada, RDC Ignite , NL and Seed grant Memorial University of Newfoundland, Canada. M. J. Ahammad acknowledges School of graduate studies, Memorial University of Newfoundland, Canada for scholarships.

Nomenclature

Symbol	Units	Description
B	1/psi	Formation volume factor
H	m	Hight of the wellbore
h	m	Hight of the reservoir
P	Pa	Pressure
q	kg/s	Flow rate
R	J/mol.K	Gas constant
T	K	Temperature
t	s	Time
u	ms ⁻¹	True velocity field of i^{th} component
v	ms ⁻¹	True velocity field of j^{th} component
w	ms ⁻¹	True velocity field of k^{th} component
c_r	1/psi	Rock compressibility
c_f	1/psi	Fluid compressibility
c_t	1/psi	Total compressibility
g_i	ms ⁻²	Gravitational force along i^{th} direction
P_e	Pa	Reservoir pressure
P_0	Pa	Reservoir pressure at the near-wellbore
P_w	Pa	Bottom hole pressure
r_e	m	Radius of reservoir end
r_w	m	Radius of wellbore
u_i	ms ⁻¹	Intrinsic velocity field of i^{th} competent
x_i	m	Axis of i^{th} coordinate
x_j	m	Axis of j^{th} coordinate

\mathcal{K}	m^2	Permeability of the medium
μ	$\text{mPa}\cdot\text{S}$	Viscosity of fluid
ρ	Kg/m^3	Density
ϕ	---	Porosity of the medium

Abbreviation

CFD	Computational Fluid Dynamics
EOR	Enhanced Oil Recovery
IPR	Inflow Performance Relations
NSE	Navier-Stokes Equations
PD	Pressure Diffusivity Equation
VOF	Volume Of Fluid

Chapter 4

Wellbore-reservoir modeling based on 3D Navier-Stokes equations with a coupled CFD solver

Title of the article: *Wellbore-reservoir modeling based on 3D Navier-Stokes equations with a coupled CFD solver*

Authors: *M Jalal Ahammad*¹, *Mohammad Azizur Rahman*², *Jahrul M Alam*³
*Stephen D Butt*⁴.

Corresponding author: Mohammad Azizur Rahman; email: marahman@tamu.edu

Journal of Petroleum Science and Engineering – Elsevier

(Submitted in January 2019).

Abstract: The fluid flows phenomena near a wellbore is the main concern of the petroleum industries since pressure drop, formation damage and other variables of interest are mostly available in this region. The fluid flows from reservoir to wellbore, thus it is important to model this phenomenon with a coupled wellbore-reservoir model. In this study, a coupled wellbore-reservoir model is developed with 3D Navier-Stokes equations and the formation damage zone is included in this model. Conservative mass flux interface model is used with GGI interface technique for the porous-porous and porous-fluid interfaces. Pressure based velocity-pressure coupling solver is used to solve model equations. An algebraic multigrid method is used to solve the system of equations for robust and faster solution. The model is validated with the analytical solution of the pressure diffusivity equation for steady-state flow condition. The coupled wellbore-reservoir model is applied for the different cases of the reservoir condition for example, different production rate, formation zone, reservoir formation conditions. The results indicate that the present CFD model can be extended to simulate the real field scale model. Coupled wellbore-reservoir modeling based on Navier-Stokes equations with efficient computational technique can lead the field of petroleum

¹Mathematics and Statistics, Memorial University, Canada, A1C 5S7

²Petroleum Engineering, Texas A & M University, Qatar

³Mathematics and Statistics, Memorial University, Canada, A1C 5S7

⁴Process Engineering, Memorial University, Canada, A1C 5S7

industries to advance the current knowledge.

Keywords: Coupled wellbore-reservoir model, simultaneous solution, interface model, formation damage, inflow performance curve, Computational Fluid Dynamics (CFD).

4.1 Introduction

Oil and gas production by vertical wells is a widely used technology. There are established methods for primary, secondary, and enhanced oil recovery techniques (Ramirez, 1987). Sophisticated drilling technologies exist for hydrocarbon recovery through vertical wells. However, the drilling process impairs the permeability of reservoir rocks, which reduces the natural productivity of the reservoirs. The phenomena are known as formation damage – a common reason that is due to drilling, completion, work-over operations, and stimulation (Yuan & Wood, 2018). In the petroleum industries, skin factor is used to evaluate the degree of influence of formation permeability around the wellbore where the formation damages happen (Liu *et al.*, 2016; Ahammad *et al.*, 2018b).

A huge impact on well productivity due to formation damage has been widely recognized in petroleum industries. There are positive trends to utilize the advantage of Computational Fluid Dynamics (CFD) facilities in the studies of reservoir flow phenomena that are related to hydrocarbon production. A few researches are performed CFD tools to understand the near-wellbore phenomena with formation damage; among them, the works done by Byrne *et al.* (2009, 2010); Sun *et al.* (2013); Byrne *et al.* (2014); Szanyi *et al.* (2018) are notable. The actual flow occurs at the millimeter scale whereas some models use the full size of the reservoirs with larger grid size. In those cases, the grid size is greater than the diameter of perforated tunnels (Szanyi *et al.*, 2018). Byrne *et al.* (2009) investigated the well performance of a wellbore with a skin zone by CFD modeling. Sun *et al.* (2013) used CFD software to simulate the production flow for 3D geometric formation considering drilling

damage, perforation damage, and anisotropy of the reservoir. Byrne *et al.* (2014) performed the CFD simulations for 3D domain with completion and production zone and confirmed that perforating the entire length of the completion and production section was not necessary in order to maximize the target flow rate. Szanyi *et al.* (2018) modeled a near-wellbore of a long horizontal well for linear flow system with CFD tools.

The modeling of fluid flows through three main regions such as reservoir region, skin zone and wellbore area is another challenge in this field. Vicente *et al.* (2000) studied the coupling of wellbore-reservoir flow with two independent equations for each region in the case of single-phase gas flow. Chupin *et al.* (2007) developed an integrated wellbore-reservoir model to investigate the liquid loading in a gas well. During the modeling of coupled reservoir, there exists a sharp interface between two domains such as porous-porous or porous-fluid interfaces. The modeling of the interface of the two domains is the main challenge in coupled wellbore-reservoir modeling. Tang *et al.* (2017) introduced a coupled wellbore-reservoir model with a drift-flux approach for the interface of two domains to study liquid flow phenomena in oil industries.

In the present article, we focus on two novel ideas for advancing our knowledge of simulating a formation damage with a coupled wellbore-reservoir model. First, we consider the first principle conservation laws based on the 3D Navier-Stokes equations to simulate the impact of formation damage. We attempt to simulate reservoir fluid flows for a coupled wellbore-reservoir model with Navier-Stokes equations using conservative flux technique for the interface condition. Second, in the simulation process, we consider a CFD approach in which the velocity and the pressure are simultaneously coupled into a single system of equations which is solved by algebraic multigrid technique. An advantage of this CFD approach is robustness, flexibility, accuracy of it. It takes the advantage of modern high-performance computing architecture, thereby bringing the fastest CFD methods to the field of oil, gas, and energy technology will explore new window of research.

4.2 Methodology

4.2.1 Governing equation for flow through porous media

We consider Navier-Stokes equations for slightly incompressible flow to investigate the flow behavior near-wellbore region of a reservoir as (see, ANSYS (2016); Szanyi *et al.* (2018); Ahammad & Alam (2017); Ahammad *et al.* (2017); Molina & Tyagi (2015)):

$$\frac{\partial \rho}{\partial t} + \frac{\partial(\rho u_j)}{\partial x_j} = 0, \quad (4.1)$$

$$\rho \left(\frac{\partial u_i}{\partial t} + u_j \frac{\partial u_i}{\partial x_j} \right) = -\frac{\partial P}{\partial x_i} + \frac{\partial \tau_{ij}}{\partial x_j} + \rho g_i + \mathcal{F}_i, \quad i, j = 1, 2, 3. \quad (4.2)$$

where $\tau_{ij} = \mu \left(\frac{\partial u_i}{\partial x_j} + \frac{\partial u_j}{\partial x_i} \right)$ and \mathcal{F}_i is the momentum sink which is a combination of Darcy and Forchheimer forces due to porous media. Note that, Forchheimer term represents the inertial force which may have significant effect on the near-wellbore fluid flows. The total momentum sink due to porous media is defined as

$$\mathcal{F}_i = -\frac{\mu}{\mathcal{K}} u_i - \beta \frac{\rho}{2} |\mathbf{u}| u_i, \quad (4.3)$$

where loss coefficient, β , is modeled by following Khaniaminjan & Goudarzi (2008) as

$$\beta = \frac{17.2 \times 10^{10}}{\mathcal{K}^{1.76}}.$$

4.2.2 Boundary conditions

We consider a coupled wellbore-reservoir model for the present CFD simulations Fig 4.2. The dimension of the computational model and other parameters are listed in Table 4.1 and Table 4.2 respectively. We also assume inlet at the outer boundary of the domain and outlet

at the wellhead of the wellbore as exhibited in Fig 4.2. The inlet boundary condition is chosen for the present CFD simulations as

$$P(r, t) = P_0, t \geq 0,$$

The outlet boundary condition is

$$r \frac{\partial P}{\partial r} = \frac{q\mu}{2\pi\mathcal{K}h}, t > 0,$$

where a constant flow rate is presented.

Further, we assume uniform pressure in the reservoir initially, thus,

$$P(r, 0) = P_0, r_w \leq r \leq r_e.$$

Top and bottom layers of the computational domain are considered as wall, so no slip boundary condition is used here.

4.2.3 Pressure calculation using other models

4.2.3.1 Analytical solution of Darcy model

The Darcy model describes the fluid flow through porous media *i.e.* flow through oil and gas reservoir. Assuming the flow is steady-state, and linear in the reservoir then classical Darcy model has the form

$$\frac{\partial P}{\partial x_i} = -\frac{\mu}{\mathcal{K}} u_i. \quad (4.4)$$

The eqn (4.4) can be written in polar coordinate for the isotropic reservoir, as

$$\frac{\partial P}{\partial r} = -\frac{q\mu}{2\pi r\mathcal{K}h}, \quad r \in [r_w, r_e]. \quad (4.5)$$

The analytical solution of Darcy equation for a steady state condition can be achieved by integration of eqn(4.5) and which leads to (Economides, 2013)

$$P = P_w + \frac{q\mu}{h\mathcal{K}} \ln\left(\frac{r}{r_w}\right), \quad (4.6)$$

where r, r_w, P_w, P and h is the reservoir radius, wellbore radius of the reservoir, wellbore pressure, reservoir pressure and height of the reservoir respectively. This equation can be written for the oilfield units as (Economides, 2013)

$$P = P_w + 141.22 \frac{Bq\mu}{h\mathcal{K}} \ln\left(\frac{r}{r_w}\right). \quad (4.7)$$

4.2.3.2 Analytical solution of pressure diffusivity equation

The reservoir fluid flows mostly radial direction towards the wellbore, thus the mass conservation equation for flow to the radial direction with true velocity is

$$\frac{\partial}{\partial t}(\phi\rho) + \frac{\partial}{r\partial r}(ru\rho) = 0. \quad (4.8)$$

Pressure diffusivity equation can be derived from the first principal of mass conservation law by combining with Darcy equation. Thus, for a slightly compressible and radially symmetric flow in an oil reservoir, the spatio-temporal reservoir pressure is given by the well-known solution of pressure diffusivity equation as (Economides, 2013; Rahman *et al.*, 2007c; Razminia *et al.*, 2014)

$$\frac{\partial^2 P}{\partial r^2} + \frac{1}{r} \frac{\partial P}{\partial r} + c_r \left(\frac{\partial P}{\partial r}\right)^2 = \frac{\phi\mu c_t}{\mathcal{K}} \frac{\partial P}{\partial t}, \quad (4.9)$$

where total compressibility, c_t , is the sum of rock and fluid compressibility $c_r = \frac{1}{\phi} \frac{\partial \phi}{\partial P}$ and $c_f = \frac{1}{\rho} \frac{\partial \rho}{\partial P}$ respectively.

This equation is a nonlinear partial differential equation in nature which is difficult to solve for an analytical solution. One can neglect the nonlinear term in eqn (4.9) if pressure

variation is small (Azin *et al.*, 2017), then the eqn (4.9) becomes

$$\frac{\partial^2 P}{\partial r^2} + \frac{1}{r} \frac{\partial P}{\partial r} = \frac{1}{\chi} \frac{\partial P}{\partial t}, \quad (4.10)$$

which is known as the pressure diffusivity equation in reservoir studies, where $\chi = \frac{\mathcal{K}}{\phi\mu c_t}$. The solution of this equation describes pressure at any location, r , at any time, t , within the domain.

We assume the reservoir is isotropic and homogeneous in all directions, well produces at constant flow rate, the radius of the well is negligible compared to reservoir radius, the reservoir has uniform initial pressure, and the well drains an infinite area (i.e., $P \rightarrow P_0$ as $r \rightarrow \infty$). Following these assumptions pressure can be calculated analytically from pressure diffusivity equation (4.10) as

$$P(r, t) = P_0 - \frac{q(t)\mu}{4\pi\mathcal{K}h} \ln \left(\frac{2.25t\chi}{r^2} \right).$$

The above equation becomes in the form of field unit by converting the respective variables in oilfield units as (Economides, 2013)

$$P(r, t) = P_0 - \frac{162.6Bq(t)\mu}{\mathcal{K}h} \left(\log_{10} \left(\frac{t\chi}{r^2} \right) - 3.23 \right). \quad (4.11)$$

4.2.4 CFD model of oil reservoir

We consider a vertical wellbore of radius r_w and a reservoir of radius r_e as depicted schematically in Fig: 4.2, where the wellbore is parallel to the z -axis. The annulus region around the wellbore represents formation damage, which is called ‘skin zone’ in this article. Table 4.1 provides the necessary field-measurement regarding the wellbore-reservoir system, and Table 4.2 presents the other modelling parameters as well. Note that, the outer boundary of the reservoir is usually far away from the well, and typically the ratio of the reservoir radius and wellbore radius can be expressed as $r_e/r_w \geq 3000$ – a CFD mesh of

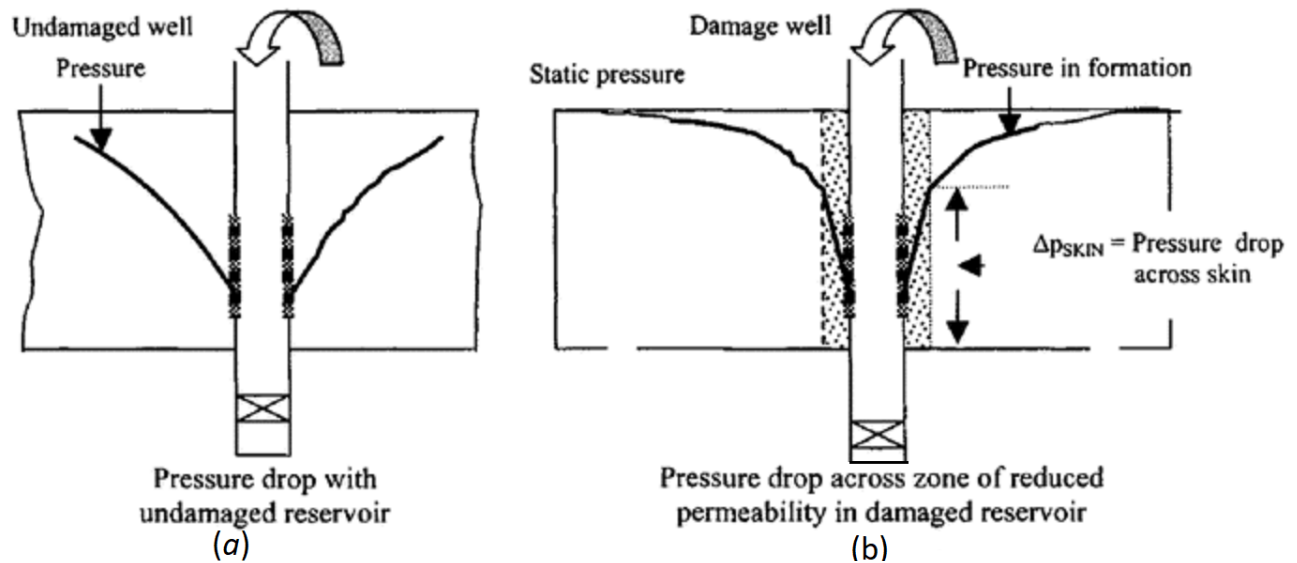
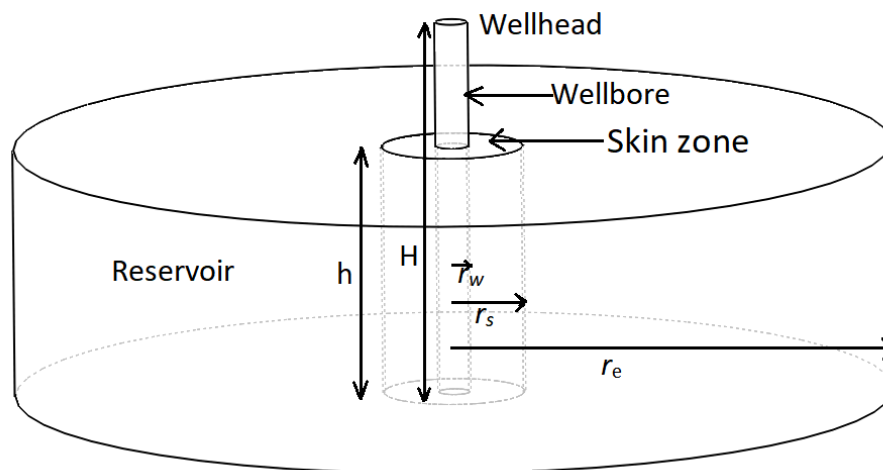


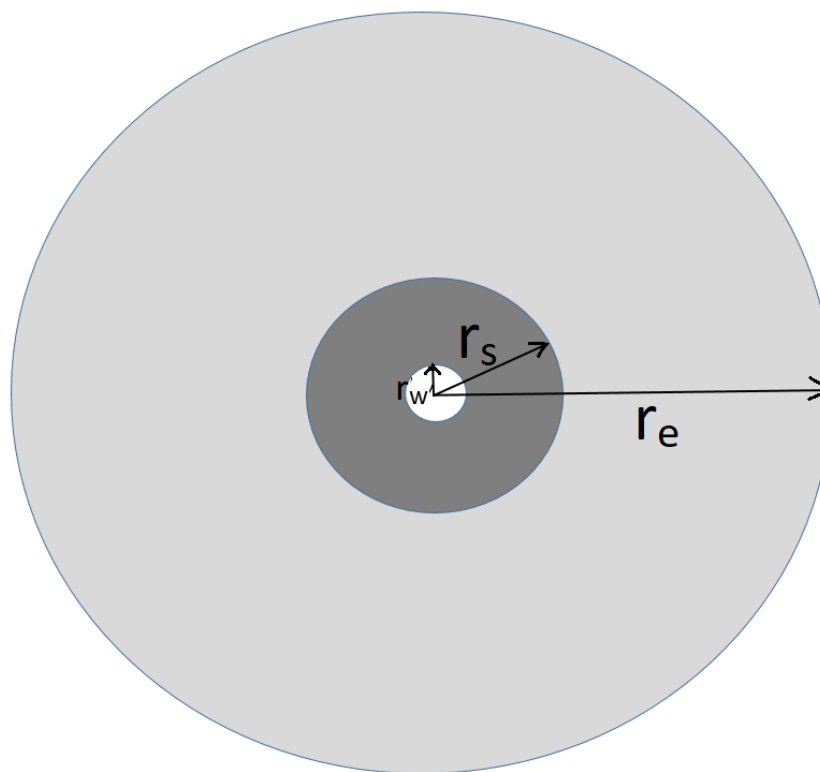
Figure 4.1: Idealized reservoir with vertical wellbore: (a) the sketch of a undamaged reservoir and (b) reservoir with skin zone (source: Chaudhry (2004)).

which is difficult to be resolved with modern computing resources. In the present work, we have developed a CFD simulation framework for the near-wellbore region, where we have truncated the outer boundary of the model reservoir with ratio $r_e/r_w \geq 28$. To ensure that the CFD model enforces the most appropriate boundary condition at $r \rightarrow r_e$, the following assumptions are adopted.

- i*) There is a steady flow of a slightly compressible reservoir fluid far away from the well at $r > r_e$.
- ii*) The pressure in the outer region is given by the solution of the pressure diffusivity equation under the assumption of radial symmetry.
- iii*) The mass flow across the outer boundary is continuous when the actual reservoir is truncated to the computational reservoir.
- iv*) The momentum flow satisfies the Darcy's equation in the outer region at $r > r_e$.



(a)



(b)

Figure 4.2: Computational geometry of a typical reservoir with skin zone: (a) 3D view and (b) top view.

Table: 4.1 Size of computational domain	
Parameter	Value [Oil Field units]
r_e	3.5 [ft]
r_w	0.125 [ft]
r_s	0.66 [ft]
h	2.0 [ft]
H	3.0 [ft]

Table 4.1: Parameter values used for the computational domain.

Under these assumptions, we expect that the CFD simulation is equivalent to the field-scale reservoir flow near the wellbore if all other parameters are consistent with the field measurements.

4.2.5 CFD technique to simulate coupled wellbore-reservoir model

The model equations need to approximate on the discrete points to simulate the physical problem. In this research, a higher resolution scheme based on the upwind method is used for the spatial discretization (Barth & Jespersen, 1989), For the time integration, implicit backward Euler scheme is used for the time integration since it is unconditionally stable (Pletcher *et al.*, 2012). After discretization, the system of equations are solved in a coupled manner on collocated grid arrangement to reduce computer memory by storing vector and scalar variables at the same locations and this is much easier to apply on complex geometries and with unstructured grids. An algebraic multigrid technique is also used to optimize the computational cost. The Rhie & Chow (1983) interpolation method is used to overcome the pressure-velocity decoupling problem on collocated grid arrangement (Lars-

son *et al.*, 2010; Abbasi *et al.*, 2013). The algorithm is implemented in *ANSYS CFX* software and we utilize the advantage of this algorithm in the study of the petroleum industry. The details procedure of this algorithm is described in Ahammad *et al.* (submitted-2018). Here the algorithm is summarized as follows:

Step 1. Initialize with Δt and other parameters value.

Step 2. Take latest value of u, v, w and P .

Step 3. Apply Rhie and Chow interpolation technique for u, v, w and P .

Step 4. Solve the coupled system of equation for u, v, w and P .

Step 5. Apply Algebraic Multigrid technique to solve the system of equations until convergence criteria fulfill.

Step 6. Solve the other variables of interest (if any).

Step 7. If time reaches at a maximum level then stop otherwise go back to step 2. and repeat the same.

4.2.6 Interface modeling for coupled wellbore-reservoir

In the modeling of coupled wellbore-reservoir, there are mainly two interfaces: porous-porous and porous-fluid. The size of the respective domains also different so sometimes size of the grid may be different. All these factors make the interface modeling more challenging than usual. General Grid Interface (GGI) algorithm connects the resultant surfaces on either side of an interface. Moreover, the GGI algorithm employs an automatic surface trimming function to connect mismatched surfaces. This approach helps GGI algorithm to successfully define interface where the surface on one side of the interface is larger than the other side. In addition, the treatment of the interface fluxes is fully implicit and conservative in mass, momentum, and other species. Thus, it allows to apply the multigrid solver directly, with the same level of robustness or convergence rate (ANSYS, 2016). *ANSYS*

CFX v17.2 have implemented GGI to investigate the rotor/stator interaction for rotating machinery. We attempt to implement this technique in the coupled wellbore-reservoir modelling in the petroleum industries with conservative mass flux interface condition.

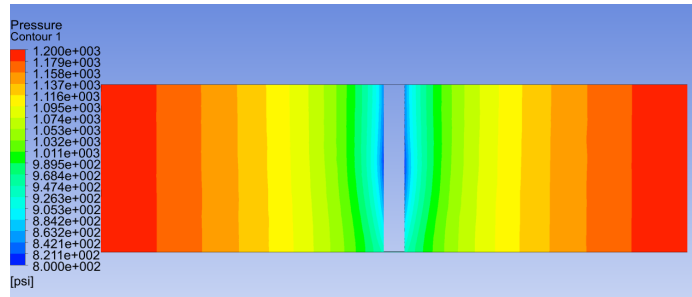
4.3 Results and discussions

4.3.1 CFD model

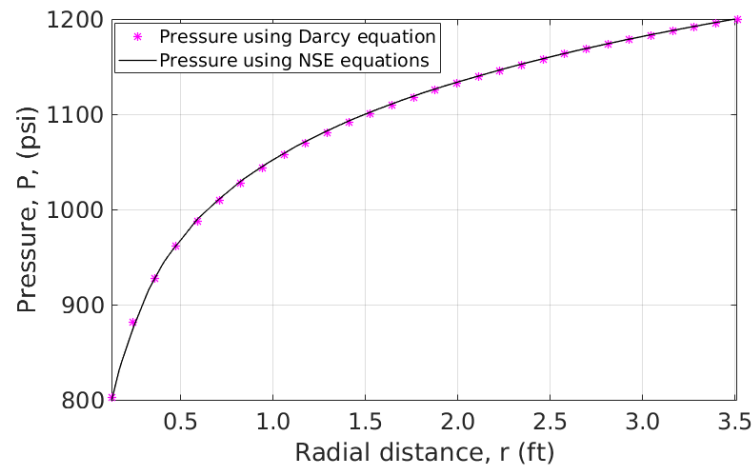
The present CFD model is verified for two cases: one is with the Darcy equation and another one is with pressure diffusivity equation. The details are described in the following sections.

4.3.1.1 Verification with the Darcy equation

We consider a simple case to verify the present CFD set up with available data in the literature. The simulation is performed only in the reservoir region *i.e.* excluding the wellbore in CFD mesh for this case and there is no formation damage in the reservoir. The model is linear ($\beta = 0$) and flow rate is chosen as $q = 474.36[\text{bbl}/\text{day}]$ for this case. This simulation helps to verify our results with the solution of Darcy equation. The pressure contour plot of the present simulation using NSE for a steady-state condition is presented in Fig 4.3(a). A pressure profile is drawn along a horizontal line of the CFD domain to compare with the solution of Darcy equation and the results are illustrated in Fig 4.3(b). As seen in Fig: 4.3(b), the present CFD simulation using NSE has an excellent agreement with the analytical solution of Darcy equation (eqn 4.7) for the steady-state flow condition. In other words, we have designed a CFD model with velocity-pressure coupling solver for oil and gas reservoir, and present CFD model predicts the flow as accurately as it is predicted by the Darcy model.



(a)



(b)

Figure 4.3: Comparison of present model with the analytical solution of Darcy equation for an idealised reservoir (without wellbore for CFD simulation): (a) pressure contour plot of the present CFD set up, (b) comparison of pressure profiles ($\beta = 0$ and $q = 474.36$ [bbl/day]).

Table: 4.2	
Parameter	Value [Oil field units]
P	1200 [psi]
\mathcal{K}	250 [mD]
\mathcal{K}_r	250 [mD]
\mathcal{K}_s	50 [mD]
ϕ_r	25 % [-]
ϕ_s	10 % [-]
q	474.36 [bbl/day]
μ	0.89 [cP]
ρ	62.24 [lb/ft ³]
β_r	1.035×10^8 [ft ⁻¹]
β_s	1.76×10^8 [ft ⁻¹]
c_t	1.4002×10^{-5} [1/psi]
B	1[-]

Table 4.2: Parameter values used for the simulations in this paper. The data for computational domain and relative variables are adapted from (Molina & Tyagi, 2015).

4.3.1.2 Verification with pressure diffusivity equation for coupled wellbore-reservoir

As mentioned in Section 6.4, a CFD solver for the coupled wellbore-reservoir model is being developed in this research in which the pressure and the velocity are obtained by solving a linear system of the equation at each time step. We verify that the field-scale distribution of reservoir pressure can be simulated accurately and efficiently by the implicit CFD method presented in this article. In this case, we consider a coupled wellbore-reservoir model as described in Fig 4.2 where the wellbore is fluid zone and reservoir as a porous zone without any formation damage. The parameters value are listed in the Table 4.2 with loss coefficient as $\beta = 1.035 \times 10^8 [\text{ft}^{-1}]$ and flow rate, $q = 300 [\text{bbl}/\text{day}]$ and reservoir formation permeability is $\mathcal{K}_r = 250 [\text{mD}]$. The simulated pressure contour is plotted on the vertical planes $y = 0$, passing through the center of the wellbore and illustrated in Fig 4.4(a). The result indicates that the assumption of radial symmetry of the flow in the outer region implies that the near-wellbore flow remains approximately symmetric unless there is a perturbation. The CFD prediction of near-wellbore pressure distribution should follow the pressure distribution predicted by pressure diffusivity model. The pressure profile of the simulation using NSE is drawn along a horizontal line of the reservoir model. The analytical solution of PD is compared with the CFD simulation using NSE and presented in Fig 4.4(b). The results have a good agreement except at the wellbore end. The slight decline of pressure drop at the wellbore end is because, we have neglected the extra term in PD to make it simple to get the analytical solution.

4.3.2 Verification with inflow performance relation for coupled wellbore-reservoir

Inflow Performance Relationship (IPR) is defined as the relationship between the well production rate *i.e.* the flow rate at the wellhead and bottomhole pressure of the reservoir. We

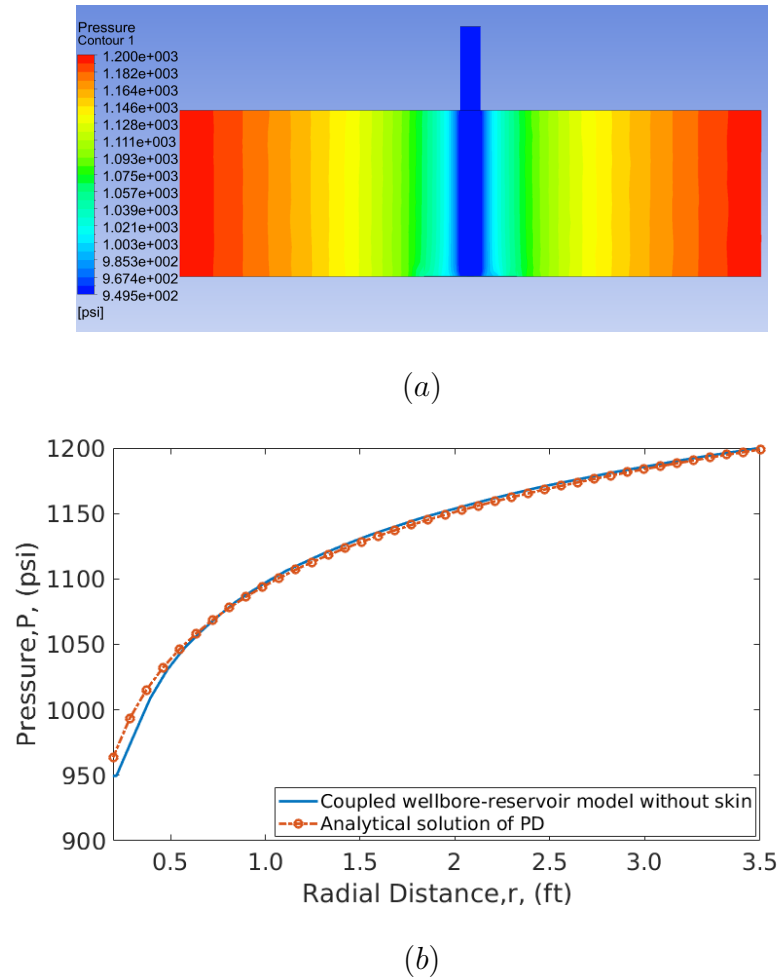


Figure 4.4: Pressure profile distribution of a reservoir without skin zone (*i.e.* $\mathcal{K}_r = 250[\text{mD}]$, and $\mathcal{K}_s = \mathcal{K}_r = 250[\text{mD}]$), (a) pressure contour plot, (b) comparison of pressure profile with analytical solution of pressure diffusivity equation for ($\beta = 1.035 \times 10^8[\text{ft}^{-1}]$ and $q = 300.00 [\text{bbl}/\text{day}]$).

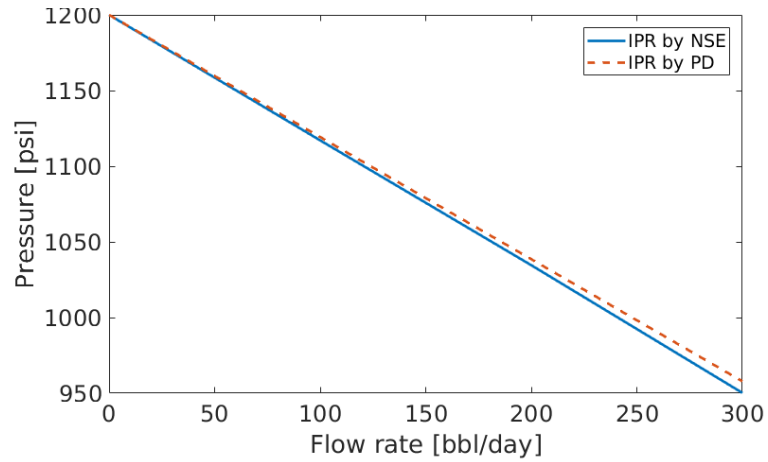


Figure 4.5: Inflow performance analysis with IPR curves for the reservoir without any skin zone.

consider a case with the parameters value listed in Table 4.2, the equation for IPR curve without skin zone leads to (Economides, 2013)

$$P_w = 1200 - \frac{q}{3.46} (\log_{10} t + 4.65). \quad (4.12)$$

We consider flow rates, $q = 100, 200,$ and 300 [bbl/day] to investigate the inflow performance and the simulations are performed for fixed time, $t = 150$ [sec]. The bottom hole pressures for the simulations using NSE are calculated at the final time and the data are compared with the theoretical solution of IPR (eqn 4.12) and the results are presented in Fig 4.5. We notice that the CFD simulations by NSE have a good agreement with the theoretical solution of IPR curve except slight deviation when flow rate increase. The reason of slight deviation may be flow becomes non-linear for a higher flow rate. This result indicates that the CFD model with NSE is capable to simulate reservoir flow as like other models.

4.3.3 Coupled wellbore-reservoir model with formation damage

In the previous section, we demonstrate the ability of the present CFD model for coupled wellbore-reservoir modeling without formation damage. In this section, we study the extension of the coupled reservoir model with a skin zone near the wellbore. A simulation is conducted with the skin zone permeability $\mathcal{K}_s = 50[\text{mD}]$, reservoir formation permeability $\mathcal{K}_r = 250[\text{mD}]$ and flow rate is $q = 300 [\text{bbl}/\text{day}]$. The contour plot and pressure profile of the simulations are presented in Fig 4.6. We see that the pressure gradually decreases in the reservoir region and suddenly drop at the skin zone. The current simulation is compared with the analytical solution of PD where only formation permeability is considered. The CFD result matches with the analytical solution until the beginning of skin zone. There is no combined analytical solution for both zones, thus deviation is observed at the skin zone. Note that, the sudden pressure drop in the skin zone is clearly noticeable in Fig 4.6(b). The comparison of flow behaviour with or without formation damage is discussed in the next section.

4.3.4 Comparison of coupled wellbore-reservoir with and without formation damage

In this investigation, we consider two cases: one simulation without skin zone (Idealized case) and another one with a skin zone (Formation damage case). This means, in the first case, there is only one porous zone with reservoir formation permeability, $\mathcal{K} = 250 [\text{mD}]$ and the second one with $\mathcal{K}_s = 50 [\text{mD}]$ for skin zone *i.e.* permeability of the damage zone at near the wellbore and $\mathcal{K}_r = 250 [\text{mD}]$ for reservoir area. The parameters value are listed in table 4.2 with flow rate, $q = 300 [\text{bbl}/\text{day}]$ for the both cases. In the previous section, we observed that for the both cases pressure is gradually decreasing towards the wellbore surface. In the case of formation damage, the pressure is suddenly dropped (see,

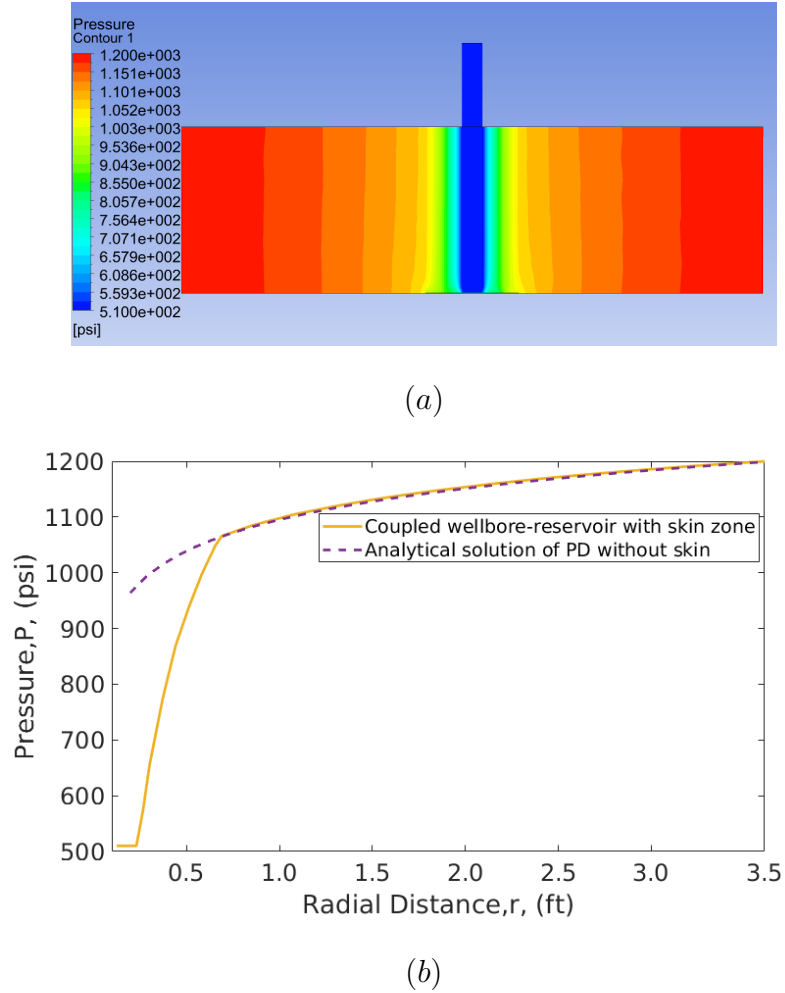


Figure 4.6: Comparison of pressure profiles of an idealised reservoir with a coupled wellbore-reservoir including formation damage where idealised reservoir permeability, $\mathcal{K} = 250[\text{mD}]$, skin zone permeability (*i.e.* $\mathcal{K}_s = 50[\text{mD}]$), : (a) pressure contour plot, (b) comparison of pressure profile with analytical solution of pressure diffusivity equation for ($\beta = 1.035 \times 10^8[\text{ft}^{-1}]$ and $q = 300.00 [\text{bbl}/\text{day}]$).

Fig 4.6(b)) at the skin zone which agrees with the convention. We examine the more detailed by investigating the pressures contour of the both simulations at the reservoir area, skin zone, and wellbore region. The comparative results are displayed in Fig 4.7, where the first column is for the undamaged (Ideal) reservoir and the second column is for damage reservoir. In this figure, the first row represents the pressure contour at the wellbore region for the both cases (Fig 4.7(a) and 4.7(b)). Having the same parameters except at skin zone, we notice that pressure drop at the wellbore for damage zone is much higher than undamaged zone. The second row expresses the pressure contour of the fluid flow through skin zone and without skin zone (Fig 4.7(c) and 4.7(d)). Here, we see pressure at the reservoir and skin zone interface for both cases are the same but pressure drop across the skin zone is higher than without skin zone. This indicates that when initial fluid moves from skin zone to the wellbore and fluid from the reservoir may not enter into skin zone with the same rate due to damage, so pressure dropped at the skin zone does not increase much. The last row (Fig 4.7(e) and 4.7(f)) represents pressure contour for the reservoir area in the both cases. We observe that pressure changes along the reservoir for both cases are almost the same. We quantify these findings with the analytical solution of PD for idealised case. In this regards, we draw pressure profile along a horizontal line of the reservoir for the both simulations. The results are exhibited in Fig 4.8 with the analytical solution of PD. In this figure, we clearly see that there are pressure level in the three regions. The pressure profiles at the reservoir region for the present CFD using NSE matches with the analytical solution of PD as shown in the previous section. The pressure drop is higher in the skin zone (more discussion in the following section) as we see in the contour plot and the wellbore pressures remain steady for both cases as there is no drag force due to porous media.

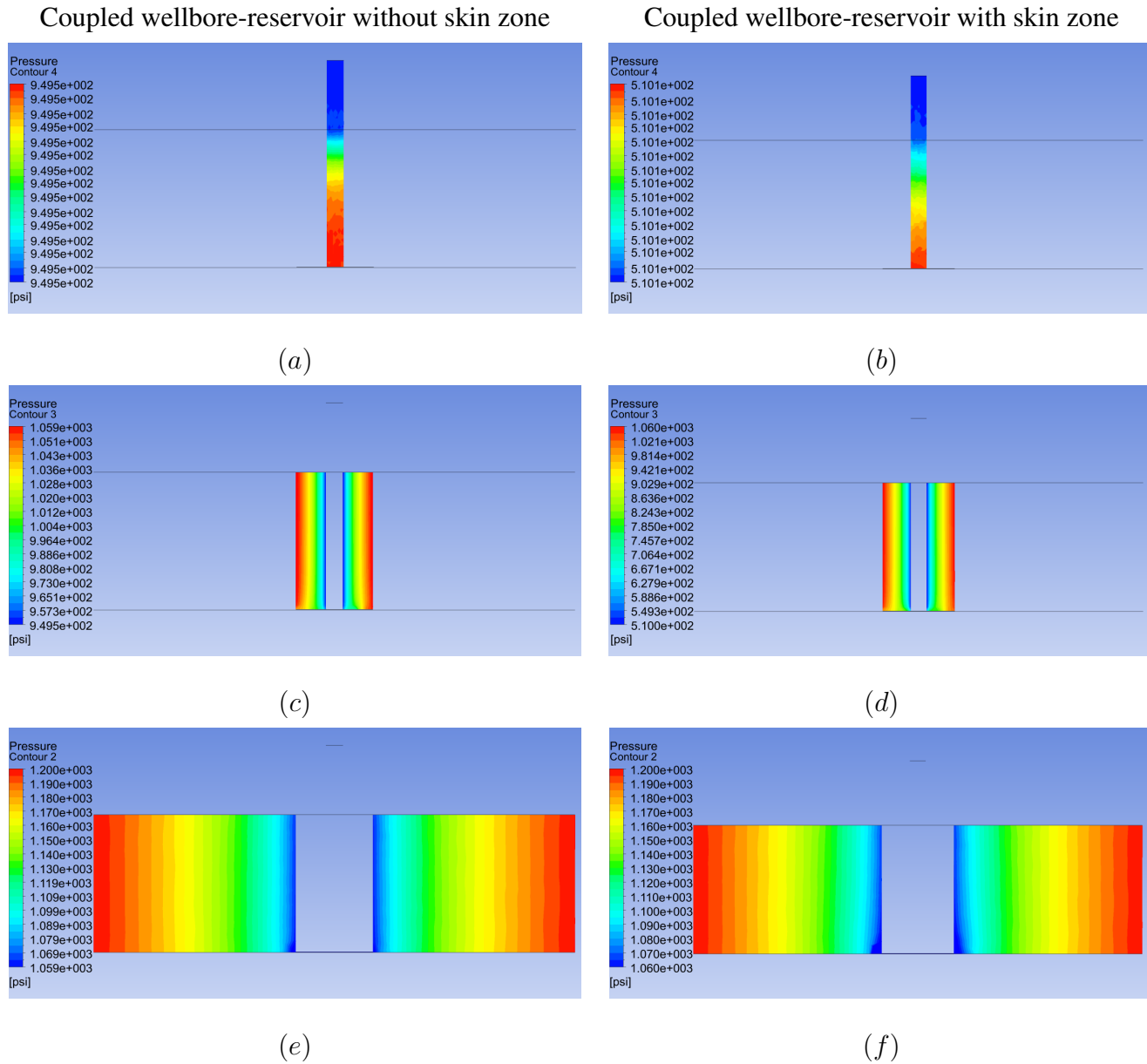


Figure 4.7: Pressure contour plot for coupled wellbore-reservoir model. First row: (a) wellbore region without skin effect and (b) wellbore region with skin effect. Second row: (c) skin zone without its effect and (d) skin zone with its effect. Third row: (e) reservoir area without skin effect and (f) reservoir area with skin effect. All parameters are same except skin zone *i.e.* $\mathcal{K}_r = 250$ [mD] & $\mathcal{K}_s = 50$ [mD] .

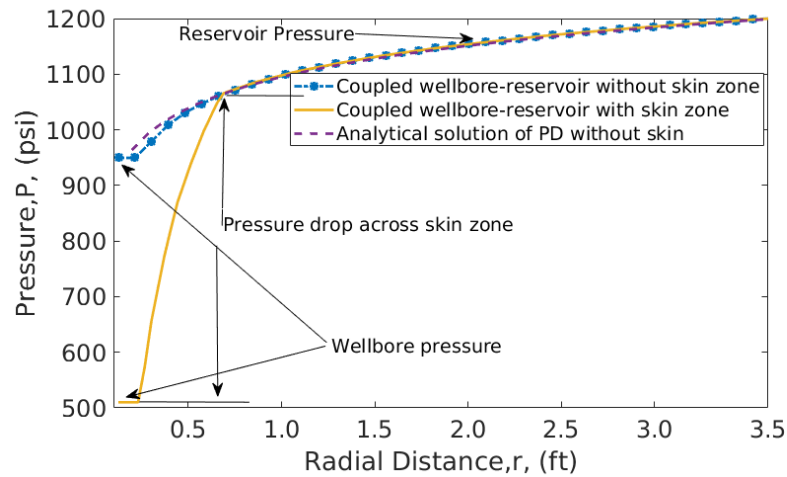
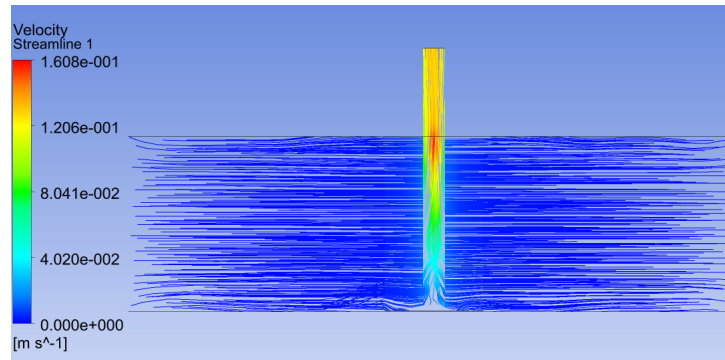


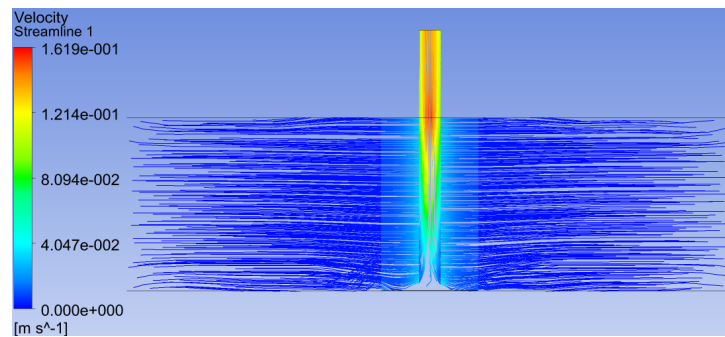
Figure 4.8: Comparison of pressure profile of the undamaged reservoir and damage reservoir with the analytical solution of PD to quantify the results presented in Fig 4.7.

4.3.5 Flow direction for coupled wellbore-reservoir with and without formation damage

Now, we are interested to see the flow direction as a coupled wellbore-reservoir in both cases. This is performed by presenting streamlines plot. The streamlines are plotted along a plane $y = 0$ and presented in Fig: 4.9 for the both cases. We see in the both cases fluids are flowing from reservoir end towards the wellbore and moving to the wellhead. This indicates that fluid flows radially towards the wellbore and along the wellbore it moves vertically to the wellhead. Moreover, fluid velocity for the idealized case remains same in the reservoir whereas fluid velocity increases at the damage zone due to drag of porous media. For the both cases, velocity is higher at surface level of the reservoir in the wellbore. Moreover, this study indicates that the coupled wellbore-reservoir model performs as desired.



(a)



(b)

Figure 4.9: Stream lines plot of the coupled wellbore-reservoir model representing flow direction: (a) without skin zone, (b) with skin zone.

4.3.6 Performance of coupled wellbore-reservoir model

In this section, we study the performance of the model for different parameters such as flow rates, different skin zones and reservoir formations.

4.3.6.1 Coupled wellbore-reservoir with different production rate

In this case, we consider four different production rates to investigate the performance of the present coupled wellbore-reservoir model in terms of pressure drop at the wellbore. The parameters value are listed in Table 4.2 and chose $\mathcal{K}_r = 250$ [mD] and $\phi_r = 25\%$ for the reservoir area, and $\mathcal{K}_s = 50$ [mD] and $\phi_s = 10\%$ for the skin zone in these simulations. Pressure profiles are drawn along a horizontal line of the reservoir for all cases and results are displayed in Fig 4.10. Here, we see the same behavior as pressure decreases gradually within the reservoir and a sudden drop occur at the skin zone. This phenomenon is already explained in the previous section and verified with the analytical solution of PD. Moreover, we notice that the pressure at the wellbore is higher for the higher production rate and lower for the low production rate. This indicates that pressure drop increases with respect to production rate within the same skin zone.

4.3.6.2 Coupled wellbore-reservoir study for different skin zones

This section explains the effect skin zone on the flow at the wellbore for the model of coupled wellbore-reservoir. The skin zone causes alterations of the flow or pressure drop behavior near the wellbore (Dake, 2001). In this investigation, we consider three types of skin zone characteristics such as skin zone permeability, $\mathcal{K}_s = 150, 100, \text{ and } 50$ [mD] with $\phi_s = 10\%$ and the respective loss coefficient, $\beta = 2.541 \times 10^7, 5.179 \times 10^7$ and 1.758×10^8 [ft⁻¹], and all other parameters are from Table 4.2. Using Hawkins's formula for skin factor, (Hawkins Jr *et al.*, 1956; Terry *et al.*, 2014) $s = \left(\frac{\mathcal{K}_r}{\mathcal{K}_s} - 1 \right) \ln \left(\frac{r_s}{r_w} \right)$, we

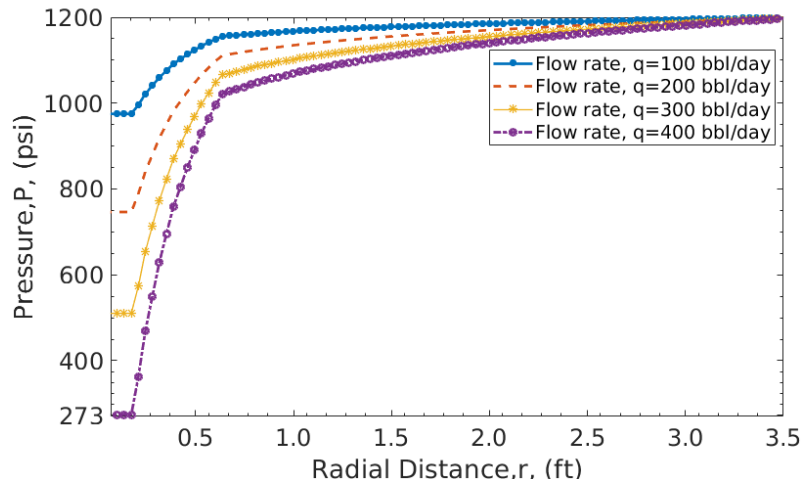
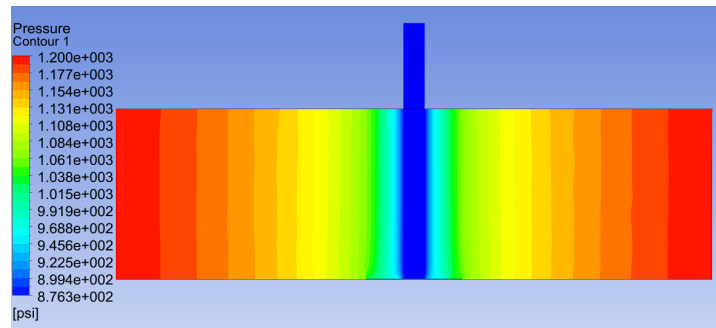


Figure 4.10: Investigation of pressure drop for the different flow conditions for coupled wellbore-reservoir model.

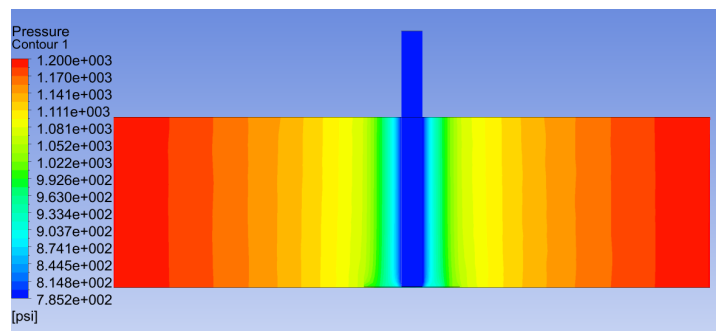
have $s = 6.63, 2.49,$ and 1.11 for the skin zone permeability, $\mathcal{K}_s = 150, 100,$ and $50[\text{mD}]$ respectively. These skin factors are within the range of skin factor used by Rangel-German & Samaniego (2000) for the study of . The positive skin factor means the negative impact on flow rate and pressure drop at the wellbore and vice-versa, moreover, skin factor zero means the ideal case. We examine the impact of skin factor with the pressure drop at the wellbore. The pressure contour plots are presented in Fig 4.11 for all three cases. We quantify our results by pressure profiles for this contour plots in Fig 4.12. We notice that higher pressure drop occurs for higher skin factor *i.e.* low permeability of the skin zone. The pressure drop increases gradually with the increasing of permeability of the skin zone and all the cases pressure profile remain the same at reservoir region.

4.3.6.3 Coupled wellbore-reservoir study for different reservoir formation

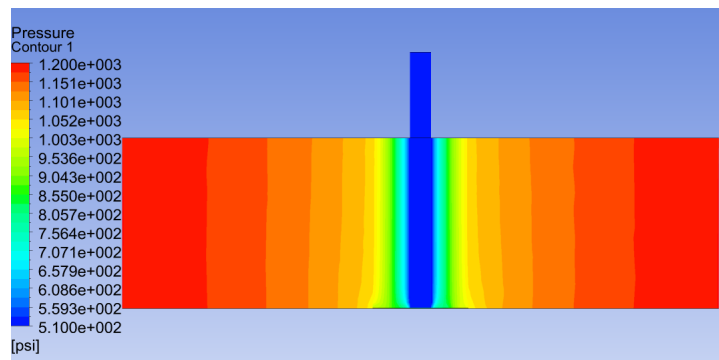
The permeability of the medium is one of the influential parameters of the reservoir that describes the ability of fluids to flow through reservoir formation (Daigle *et al.*, 2017).



(a)



(b)



(c)

Figure 4.11: Pressure contour plots for fixed reservoir formation with different skin zones such as skin permeability: (a) $\mathcal{K}_s = 150$ [mD], (b) $\mathcal{K}_s = 100$ [mD], and (c) $\mathcal{K}_s = 50$ [mD].

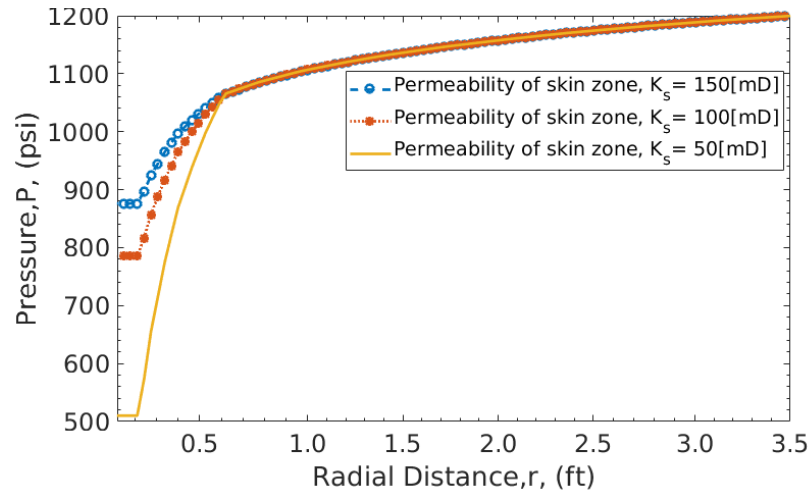


Figure 4.12: Effect of different skin zones on pressure drop, the pressure profiles are drawn along a horizontal line of the domain for the simulations presented in Fig:4.11.

Hereinafter, we investigate the performance of the present CFD model for the different reservoir formations. We consider three types of reservoir formations with permeability, $\mathcal{K}_r = 250, 400$ and 500 [mD] keeping skin zone permeability fixed as $\mathcal{K}_s = 50$ [mD] for all three cases, and other parameters are mentioned in the Table 4.2 with $q = 300$ [bbl/day]. We are not verifying the results here instead investigating the influence of formation permeability in the changing of fluid pressure through the medium. As we see in Fig 4.13, bottom-hole pressure decreases more for the lower permeable formation compare to higher. By observing contour plot, it is difficult to understand the pressure drop across the reservoir to the skin zone. Thus, we draw pressure profiles by following the process as before and the results are illustrated in Fig 4.14. In the pressure profile graph, there are three zones: reservoir area, skin zone, and wellbore area. The pressure drop of the reservoir upto skin surface ($r_s = 0.2$ [m]) is higher for the low permeable formation. This is the reason for pressure drop at the wellbore rather than skin zone effect here. The interesting observation is that differential pressure across the skin is almost the same for three cases as skin zone

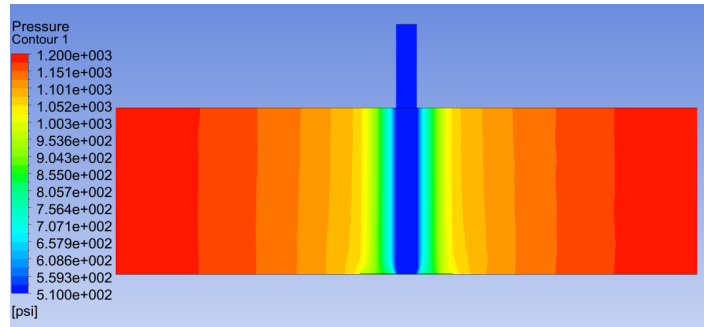
permeability is the same for all cases. The whole phenomena matches with the natural situation and consistent with the results analysis in section 4.3.4 with the analytical solution of PD. The investigation confirms that the present CFD setup is capable to model coupled wellbore-reservoir system with different formations characteristics.

4.4 Conclusion and future work

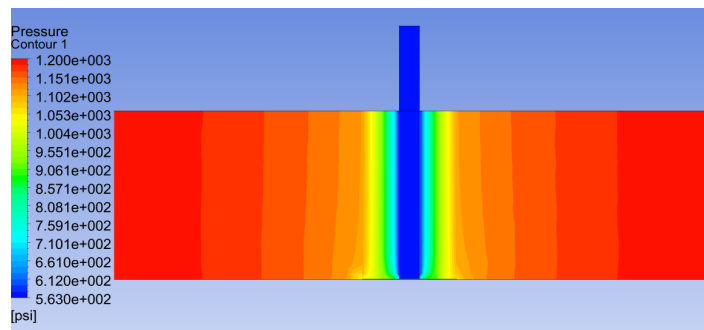
In this study, a coupled wellbore-reservoir model is developed with efficient CFD algorithm to solve the mathematical equations for the reservoir fluid flow. The present CFD facilities offer as a useful tool to help to understand reservoir flow behavior. The present study successfully investigates towards the formulation of the wellbore-reservoir model. We verify our CFD model with analytical solutions of PD, and IPR curve, and other models. The present model enables to study all three regions with a single equation using appropriate interface condition. The model performs as expected for three cases: different flow rates, skin zones, and reservoir formations. Then, we study the transient nature of the flow near the wellbore. In the future, theoretical development can be established for IPR curve to compare the inflow performance of the present coupled wellbore-reservoir model. Furthermore, this model can be extended for the realistic reservoir conditions and can be more verified with field data. Moreover, it can be easily extended for two-phase flow study with appropriate interface conditions. In addition, turbulence flow through wellbore can be modelled with this CFD methodology.

Acknowledgments

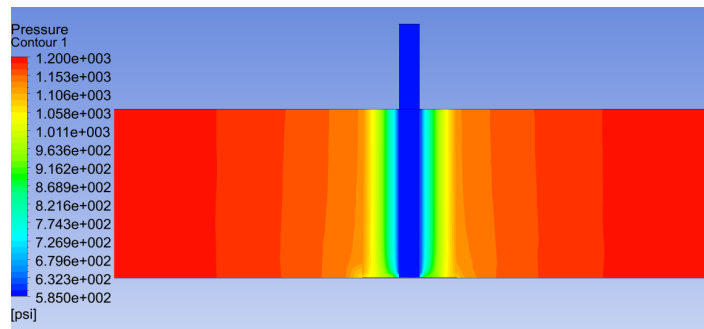
J. Alam acknowledges financial support from the National Science and Research Council (NSERC),Canada. M. A. Rahman acknowledges financial support from the National Sci-



(a)



(b)



(c)

Figure 4.13: Pressure contour plots for fixed skin zone with different reservoir formations permeability such as: (a) $\mathcal{K}_r = 250$ [mD], (b) $\mathcal{K}_r = 400$ [mD], and (c) $\mathcal{K}_r = 500$ [mD].

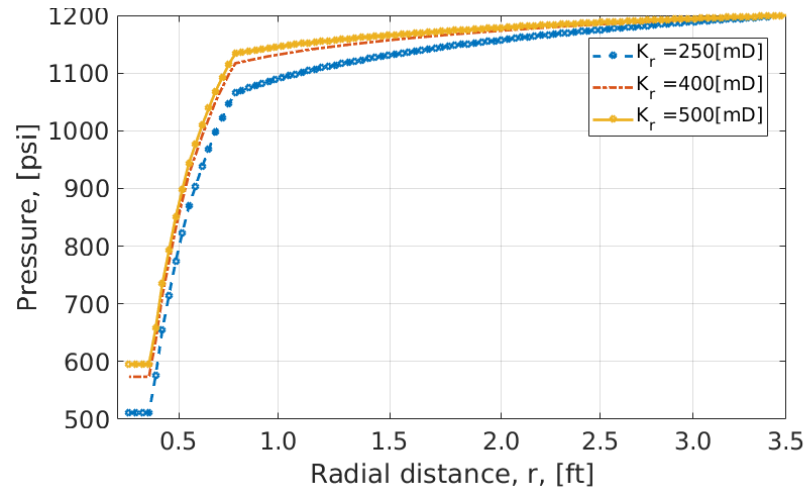


Figure 4.14: Effect of different reservoir formation permeability on pressure drop, the pressure profiles are drawn along a horizontal line of the domain for the simulations presented in Fig:4.13.

ence and Research Council-discovery grant (NSERC-DG), Canada, RDC Ignite , NL and Seed grant Memorial University of Newfoundland, Canada. M. J. Ahammad acknowledges School of graduate studies, Memorial University of Newfoundland, Canada for scholarships.

Nomenclature

Symbol	Units	Description
B	—	Formation volume factor
h	m	Hight of the reservoir
H	m	Hight of the wellbore
P	psi	Pressure
q	kg/s	Flow rate

s	--	Skin Factor
t	s	Time
u	ms^{-1}	True velocity field of i^{th} competent
v	ms^{-1}	True velocity field of j^{th} competent
w	ms^{-1}	True velocity field of k^{th} competent
c_r	1/psi	Rock compressibility
c_f	1/psi	Fluid compressibility
c_t	1/psi	Total compressibility
g_i	ms^{-2}	Gravitational force along i^{th} direction
P_w	psi	Bottom hole pressure
r_e	m	Radius of reservoir end
r_s	m	Radius of skin zone
r_w	m	Radius of wellbore
x_i	m	Axis of i^{th} coordinate
x_j	m	Axis of j^{th} coordinate
u_i	ms^{-1}	Intrinsic velocity field of i^{th} competent
\mathcal{K}_r	m^2	Permeability of the medium at reservoir area
\mathcal{K}_s	m^2	Permeability of the medium at skin zone
μ	mPa.S	Viscosity of fluid
ρ	Kg/m^3	Density
ϕ_r	--	Porosity of the medium the medium at reservoir area
ϕ_s	--	Porosity of the medium medium at skin zone
Abbreviation		
CFD		Computational Fluid Dynamics
EOS		Equation of State

GGI	General Grid Interface
NSE	Navier-Stokes Equations
PD	Pressure Diffusivity Equation
VOF	Volume Of Fluid
EOR	Enhanced Oil Recovery
IPR	Inflow Performance Relations

Chapter 5

Numerical investigation of two-phase flow in a perforation tunnel of a hydrocarbon reservoir

Title of the article: *Numerical investigation of two-phase flow in a perforation tunnel of a hydrocarbon reservoir*

Authors: *M Jalal Ahammad*¹, *Mohammad Azizur Rahman*², *Li Zheng*³.

*Jahrul M Alam*⁴, *Stephen D Butt*⁵.

Corresponding author: Mohammad Azizur Rahman; email: marahman@tamu.edu

Journal of Natural Gas Science and Engineering – Elsevier

Published in volume = 55, pages = 606 – 611, year = 2018.

Abstract: The oil and gas reservoir productivity index depends on the performance of fluid flow through the perforated tunnels. Experimentally, it was observed that higher fluid flow rate occurs in perforation by drilling technique compare to the traditional shooting techniques. This idea is favorable for the increased hydrocarbon production from a hard formation with minimizing formation damages due to shooting techniques. The better understanding of formation damage mechanisms for various reservoir conditions can be optimized for the economic benefits and managerial decision. The perforation by drilling (PD) technique is proposed as an alternative perforation technique since this technique induces less formation damages. Experimental and numerical investigations are ongoing research in this regards. Two-phase flow through a perforation tunnel from the reservoir is being modelled using Navier-Stokes equations. The numerical data were validated with the experimental data. The effects of different petro-physical properties were analyzed in the simulations such as permeability, porosity, fluid viscosity, flow rates, and injection pressure.

¹Mathematics and Statistics, Memorial University, Canada, A1C 5S7

²Petroleum Engineering, Texas A& M University, Qatar

³Process Engineering, Memorial University, Canada, A1C 5S7

⁴Mathematics and Statistics, Memorial University, Canada, A1C 5S7

⁵Process Engineering, Memorial University, Canada, A1C 5S7

Keywords: Computational fluid dynamics (CFD), perforation, formation damage, porous media, two-phase flow.

5.1 Introduction

The proportion of natural gas is increasing significantly for the adjustment of energy sources structure and the fast development of urban fuel gas industry (Wu *et al.*, 2016). The extraction of gas from a reservoir is not that straightforward. Sometimes, natural gas is often extracted with water in most gas fields. This indicates that multiphase flow, especially gas-water two-phase flow, is more common in a gas reservoir. In addition to oil and gas fields, the theory of multiphase flow in porous media can also provide more information to understand the flow phenomena in an aquifer and CO₂ storage (Horgue *et al.*, 2015b). Thus, the research in multiphase flow through porous media is of profound importance in many active research area such as petroleum engineering applications. In petroleum industries, perforation is an essential stage of well completion before final production. The perforation is a communication media that connects the reservoir formation with the wellbore to produce oil or gas. The perforation is created to increase the production rate, though there are some disadvantages of the perforation which leads to damage the virgin reservoir (Wan, 2011). There are different types of technique for perforation, for example, perforation by shooting (Behrmann *et al.*, 2002). The performance of perforation depends not only on various perforation characteristics such as length, radius, density, phasing angle, but also perforation techniques (Economides, 2013). A proper perforation technique can increase production by 10-20% (Bell & Clark, 2009). The perforation technique for the gas reservoir is different than the oil reservoirs (Civan, 2015). The influence of the well completion and perforation performance, and ultimately reservoir life fully depends on the productivity index (Dake, 1994). Numerous researches were conducted towards the perforation

performance including skin factors, low to high permeability, reservoirs heterogeneity etc.. Landman *et al.* (1991) presented a mathematical model to investigate the effects of the perforation distribution of a horizontal well under a steady state inflow condition. Hagoort (2007) studied an analytical model for the prediction of the perforated wells. Single-phase Darcy flow through a single perforation in a semi-infinite porous medium is considered in that case. Rahman *et al.* (2007c) compared the perforation by drilling technique with traditional perforation technique by shooting (PS) for single phase flow. Further, (Rahman *et al.*, 2007a) studied the skin effect due to perforation with the same approach. In both works, they found that during the PS technique fine particles get redistributed around the perforation tunnel. The redistribution reduces the pore throat size which is liable for permeability reduction significantly. As a result, the flow rates decrease at the same level of differential pressure. However, the reduction of permeability by the traditional perforation techniques have not been thoroughly investigated with multiphase flow in petroleum production engineering, especially in the gas reservoirs (Rahman *et al.*, 2007c).

In this article, we study a novel technique for the perforation called perforation by drilling (PD) using CFD. We investigate the improvement of the reservoir productivity index with this technique for the two-phase flow. In this study, we also get more information on the formation damage due to tradition perforation methods. This new technique of perforation can be applied to the EOR process for injecting solvent or fluid.

5.2 Conventional perforation techniques

Perforation is the important key element and the final stage in the completion of a reservoir well. The well completion process is a crucial part, as the productivity index and future performance of the well depend on the successful perforation (Wan, 2011). Day-by-day, more developed technologies are in progress and complex reservoir can be explored to ex-

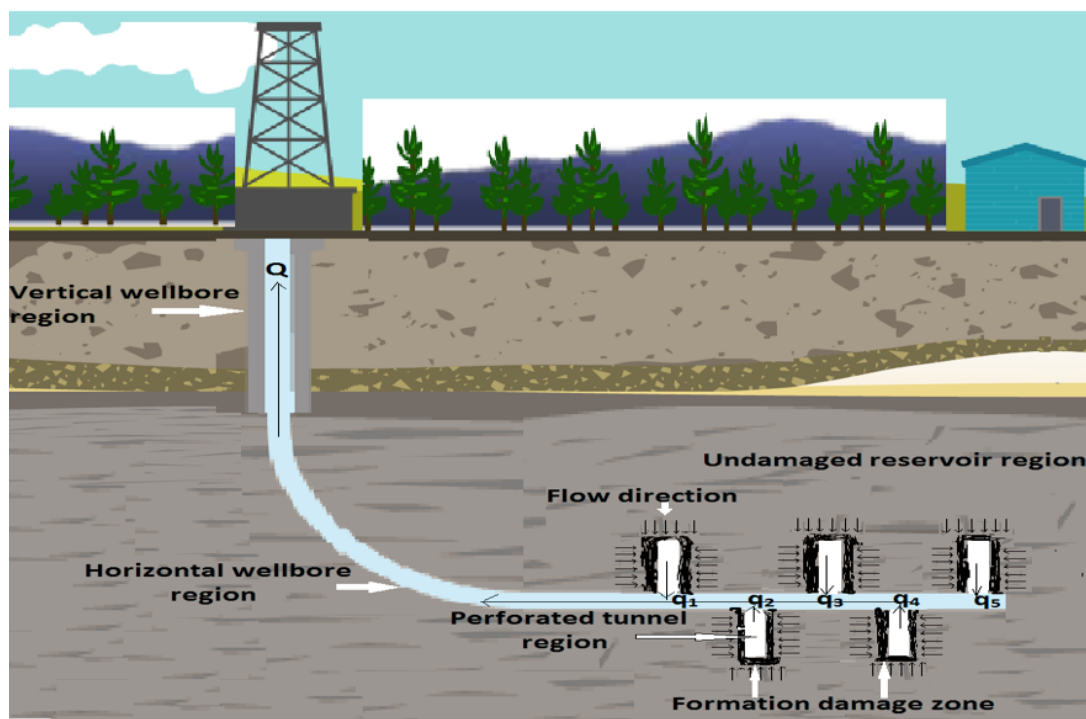


Figure 5.1: Sketch of an idealized reservoir well configuration with horizontal wellbore involving variety of the reservoir elements such as perforation tunnel, formation damage undamaged reservoir region etc.

tract more oil. A schematic deviated drilling system and perforation tunnels with related formation damage is exhibited in Fig: 5.1 alongwith other components of the hydrocarbon reservoir. In the early 1900's, mechanical punching methods were used, projectile technology was introduced in mid-1920's. After 1932, bullet gun was used with a hardened-steel bullet, then this device was replaced with shaped-charged perforator known as a jet perforator. By this time, various techniques were developed including perforation by shooting (PS) (Rahman *et al.*, 2007c). Generally, high energy charged explosives are used for the perforation technique. Mostly formation damage occurs during the 'perforation' stage of the well completion (Wan, 2011). Due to the powerful explosion, the permeability of the reservoir formation reduces about 20 to 75% of the original permeability (Gilliat *et al.*, 1999). As a result, the production of the reservoir reduces significantly (Wan, 2011). Rahman *et al.* (2007a) reported there is a severe decline in productivity index of the reservoir well due to existing perforation technique - so called perforation by shooting (PS). Formation damage is an undesirable operation or alteration of the original formation of the reservoir which causes the reduction of the reservoir permeability. This leads the declination of the productivity index of the reservoir significantly. Thus, it is a matter of billions dollar loss of revenue in the worldwide reservoir industries. The most of the research towards eliminating the permeability reduction due to perforation and the increasing of production rates were done with the various types of a new concept for shooting technology such as enhancing the mechanical properties of the gun (Behrmann *et al.*, 2002).

5.3 Proposed technique - Perforation by Drilling (PD)

In this study, we propose a novel technology for perforation called perforation by drilling (PD). The perforation of drilling (PD) can be performed by deviated drilling system. This will be the new window for the oil industries that can improve the production decline due

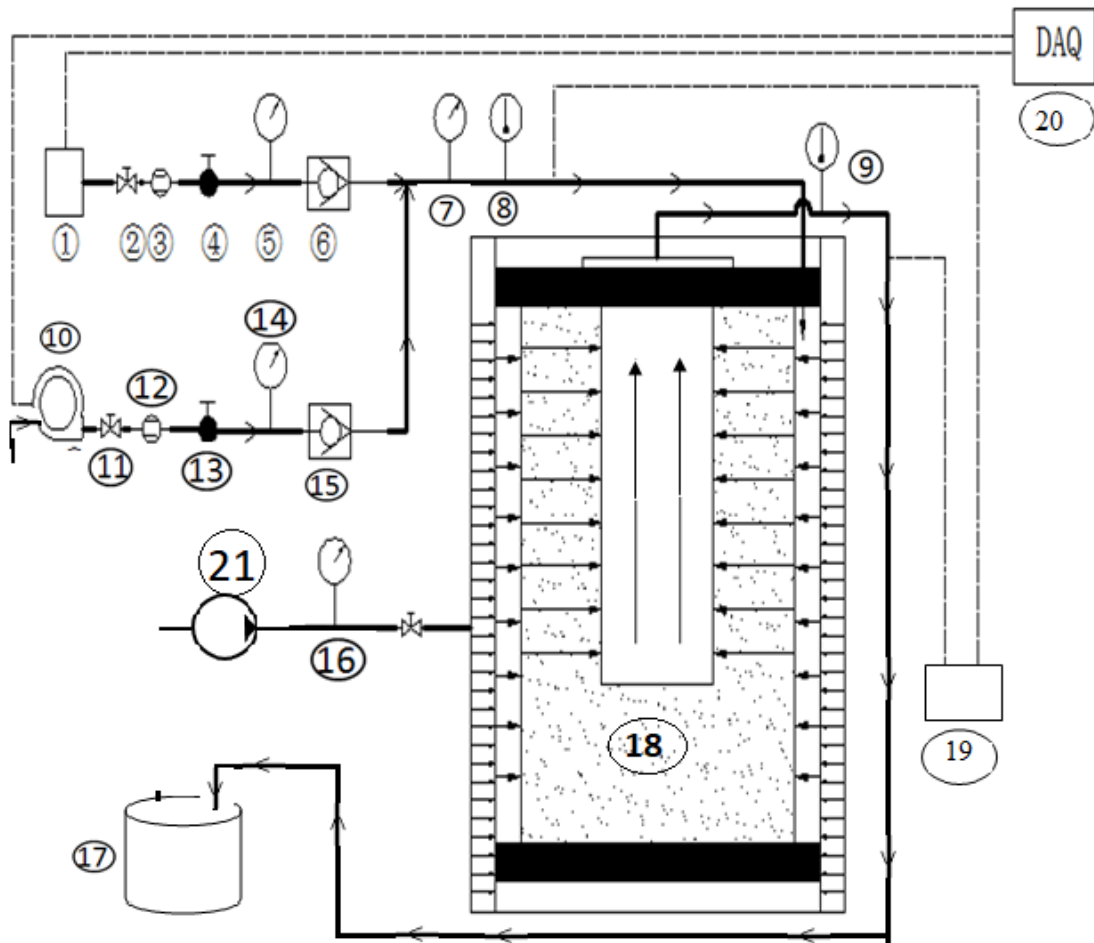


Figure 5.2: Sketch of the experimental set up. (1) Air compressor, (2) and (11) Pressure release valve; (3) Air flow meter; (12) Liquid flow meter; (4) and (13) Control valve; (6) and (15) Non-return valve; (5), (7), (14) and (16) Pressure gauges; (8) and (9) Thermometers; (10) Pump; (17) Water Reservoir; (18) Radial flow cell; (19) Differential pressure gauge; (20) Computerized DAQ (Data Acquisition) system; and (21) Hydraulic pump.

to tradition perforation techniques. The aim of this investigation is to improve the knowledge of well performance and enhance oil recovery using multiphase flow mechanism. We are on the process of developing experimental facilities to study the benefit of perforation by drilling. A sketch of a laboratory experimental set-up is presented in Fig: 5.2. Due to laboratory constrained most of the experimental studies are conducted by neglecting some important reservoir properties such as actual reservoir pressure, axial load, draw-down pressure, and thermal effects. A brief literature review shows that the experimental investigation of perforation techniques are based on simplified assumptions (see, Rahman *et al.* (2007c)). In the present study, a higher confining pressure, axial load, and draw-down pressure are maintained to simulate the in-situ conditions and comparatively larger core sample is used. During the experiment, a specific volume of water was injected into the core sample. Meanwhile, the porosity was changed to observe the change of pressure buildup profiles in the core samples. The detailed description of the experimental development is presented in chapter 2. The experiment has the facilities to inject gas and liquid into the sample through flow lines. Confining pressure helps to create reservoir pressure. A sophisticated rubber membrane is used to isolate the sample from contamination of hydraulic oil that creates confining pressure. The inlet fluid flow rate is measured across the cylindrical samples at a desired flow pressure and outlet flow rate across the perforated tunnel. The core samples used in the numerical simulation exhibits the behavior of sandstone. In a future experiment, both outcrop and laboratory built core samples of sandstone can be used. Different recipes can be used to prepare core samples by using a different ratio of sand, cement.

In the numerical simulations, gas and water are injected radially through the sample. In the single-phase flow, water is injected and the results are compared with the numerical simulation. After validation of numerical simulation with single-phase flow, we moved to two-phase flow with air/water injection process in the numerical simulation.

5.4 Mathematical model

The fluids are entering from reservoir to perforated tunnel, so this is convenient to consider non-Darcy flow (Huang *et al.*, 2016; Saboorian-Jooybari & Pourafshary, 2015; Song *et al.*, 2015; Zeng & Grigg, 2006). In the case homogeneous multiphase flow system, a common flow field has the same characteristics of all fluids, as well as other relevant fields such as temperature. Therefore, the homogeneous model assumes that the transported quantities for that process remains the same for all phases (Higdon, 2013; Miller *et al.*, 1998). The set of equations solved in this problem are the mass and momentum conservation laws. Forchheimer equation is combined through the source term in the momentum balance equation (ANSYS, 2016)

$$\frac{\partial \rho}{\partial t} + \frac{\partial(\rho u_j)}{\partial x_j} = 0, \quad (5.1)$$

$$\rho \left(\frac{\partial u_i}{\partial t} + u_j \frac{\partial u_i}{\partial x_j} \right) = -\frac{\partial P}{\partial x_i} + \frac{\partial \tau_{ij}}{\partial x_i} + \rho g_i + \mathcal{F}_i, \quad (i, j = 1, 2, 3), \quad (5.2)$$

where $\tau_{ij} = \mu \left(\frac{\partial u_i}{\partial x_j} + \frac{\partial u_j}{\partial x_i} \right)$. Darcy and Forchheimer forces are coupled with the momentum sink through \mathcal{F}_i which is defined as

$$\mathcal{F}_i = -\frac{\mu}{\mathcal{K}} u_i - \frac{17.2 \times 10^{10}}{\mathcal{K}^{1.76}} \frac{\rho}{2} |\mathbf{u}| u_i. \quad (5.3)$$

Here, multiphase flow variables are defined as $\rho = \sum_{\alpha=1}^{N_p} r_\alpha \rho_\alpha$, $\mu = \sum_{\alpha=1}^{N_p} r_\alpha \mu_\alpha$, where α, N_p , and r_α indicates phase of fluid, number of total phases and volume fraction.

5.4.1 Computational technique

A finite volume based numerical method is applied to solve the model equations. The system of equation is solved in a coupled manner with an efficient multigrid solver so that the

Table: 5.1 Size of computational domain	
Parameter	Value
Sample diameter	15.24 [cm]
Sample height	30.48 [cm]
Perforation tunnel diameter	2.54 [cm]
Perforation tunnel height	25.4 [cm]

Table 5.1: Parameter values used for the computational domain.

Table: 5.2 Boundary conditions used for the simulations	
Position	Boundary Conditions
Inlet	Air and water flow rates with volume fractions
Outlet	Atmospheric pressure or back pressure
Medium	Homogenous porous media with a particular porosity
Wall	No-slip condition

Table 5.2: Parameter values used for the computational domain.

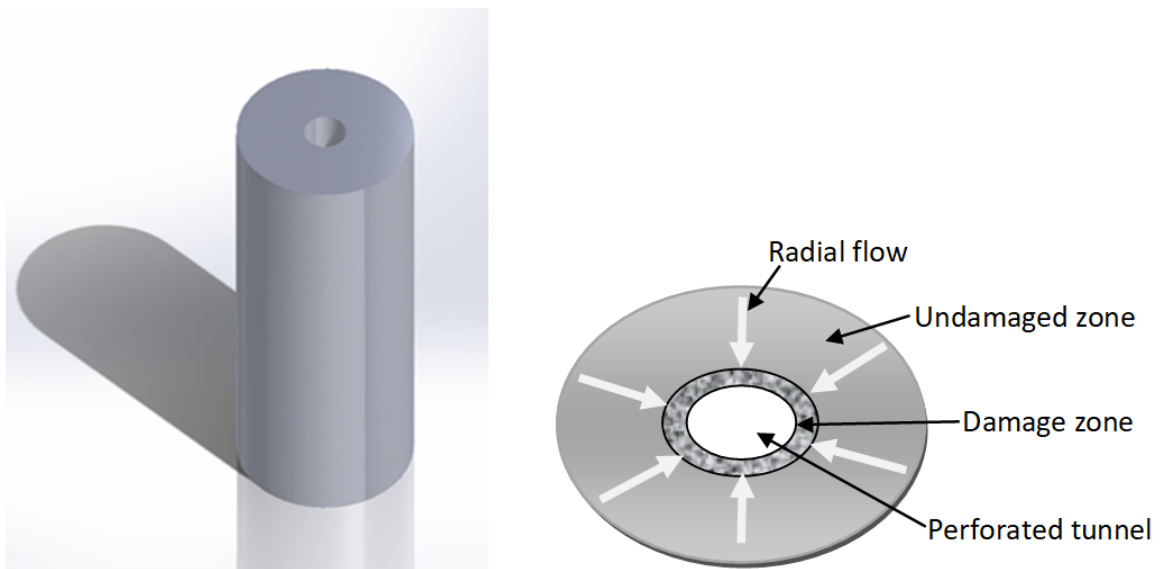


Figure 5.3: A diagram of computational domain. Left figure is the computation geometry having a perforation tunnel at the center and right figure is the cross section of the domain representing the damage zone, undamage region, perforation tunnel and flow direction.

computational cost becomes optimistic. Hexahedral type meshes with no inflation and a smaller grid size, and higher smoothing is used to capture the flow at near perforation tunnel. The detailed computational algorithm is described in Ahammad *et al.* (2018a). Such computational facilities available in *ANSYS CFX* and the advantage of it is availed here. *ANSYS CFX* is a well-known commercial software that assists to model fluid flow through porous media and other related fluid flow problems. A cylindrical core sample with a perforated tunnel at the center is used for the numerical simulations. The representation of the perforation in the formation pay zone and the simulated sample is presented in Fig 5.3. The dimensions of the geometry are mentioned in the Table 5.1. For simplicity, we have used homogeneous and isotropic porous medium in the simulation. The boundary conditions for the simulations are articulated in the Table 5.2. The validation of the CFD simulations for the perforation by drilling was compared with the results of Rahman *et al.* (2007c) and

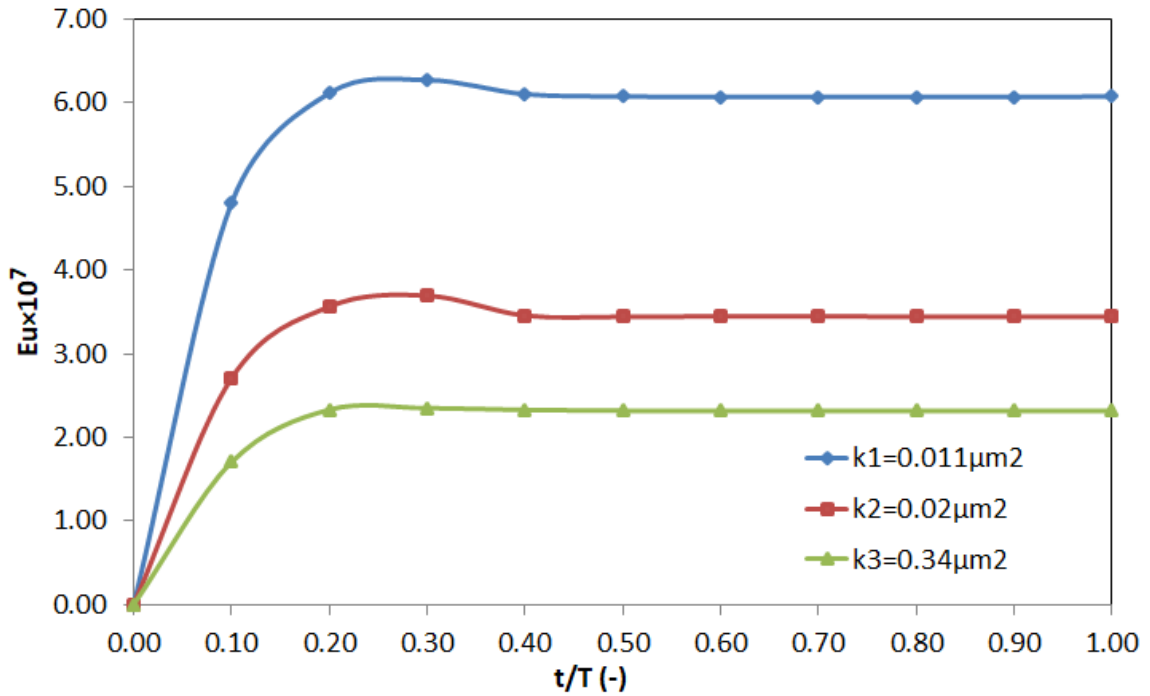


Figure 5.4: The Effect of Permeability on Injection Pressure.

presented in Zheng *et al.* (2016).

5.5 Results and Discussions

The results presented here are a continuous research and extension of the researches presented in Zheng *et al.* (2016). To overcome the challenge of scaling-up of the model, we have presented all the data in the non-dimensional form. The x-axis is presented by non-dimensional time, (t/T_{total}) and y-axis is presented by Euler number (Eu). Euler number (Eu) is the ratio of pressure force (P) to inertia force (ρu^2 i.e. density times squared velocity). Euler number helps to understand the fluid flow when the pressure difference between two points is important. In all the cases of simulations, the mixture of water and air is injected into the core sample for two-phase flow. Three core samples with different val-

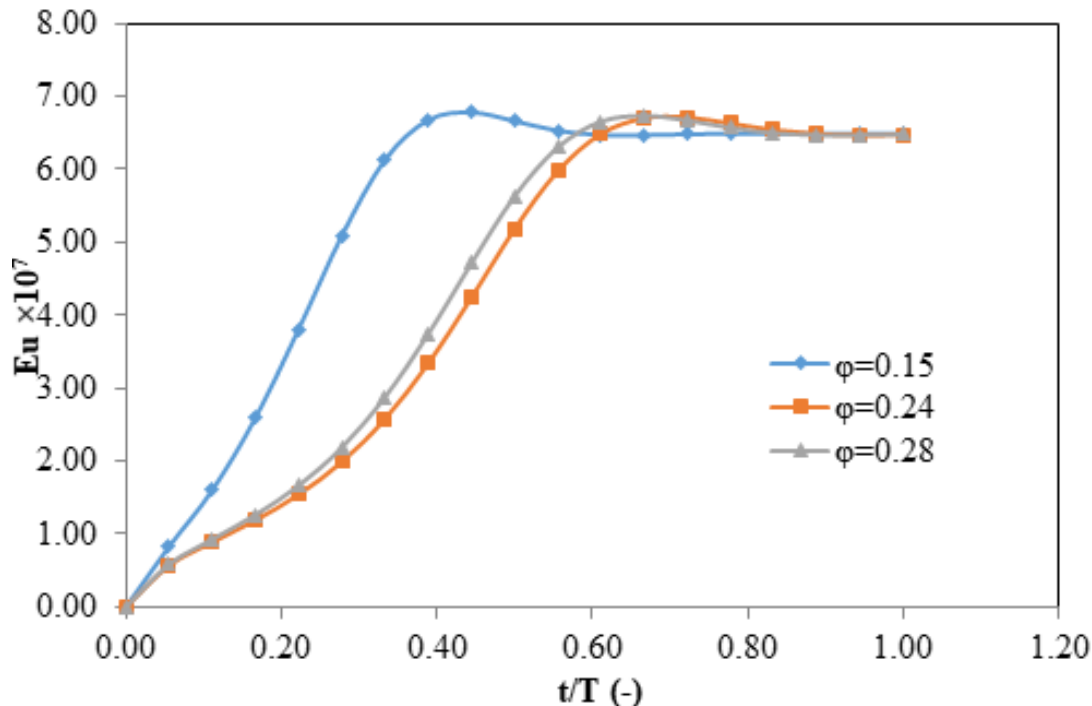


Figure 5.5: The Effect of Porosity on Injection Pressure.

ues of permeability are used to observe the effect of pressure buildup profile with time. The results are presented in Fig 5.4. The injection pressure will increase gradually before the steady-state condition is achieved. When the permeability is low, the higher injection pressure is needed to inject a specific volume of mixture fluid into the core sample and a slightly longer time is required to reach the steady state.

Figure 5.5 describes how the porosity influences the injection pressure for the mixture fluid. The porosity has fewer effects on the pressure after the steady-state condition is achieved. This is because the porosity does not influence the injection pressure of any one of the mixture fluid. However, the porosity affects the pressure profile before the steady-state for a lower porosity sample. The pressure profile achieves higher value in case of low porosity sample, compared to the other high porosity samples. The Jamin effect is dominant in case of low porosity sample before the steady-state condition is achieved. We have used Euler

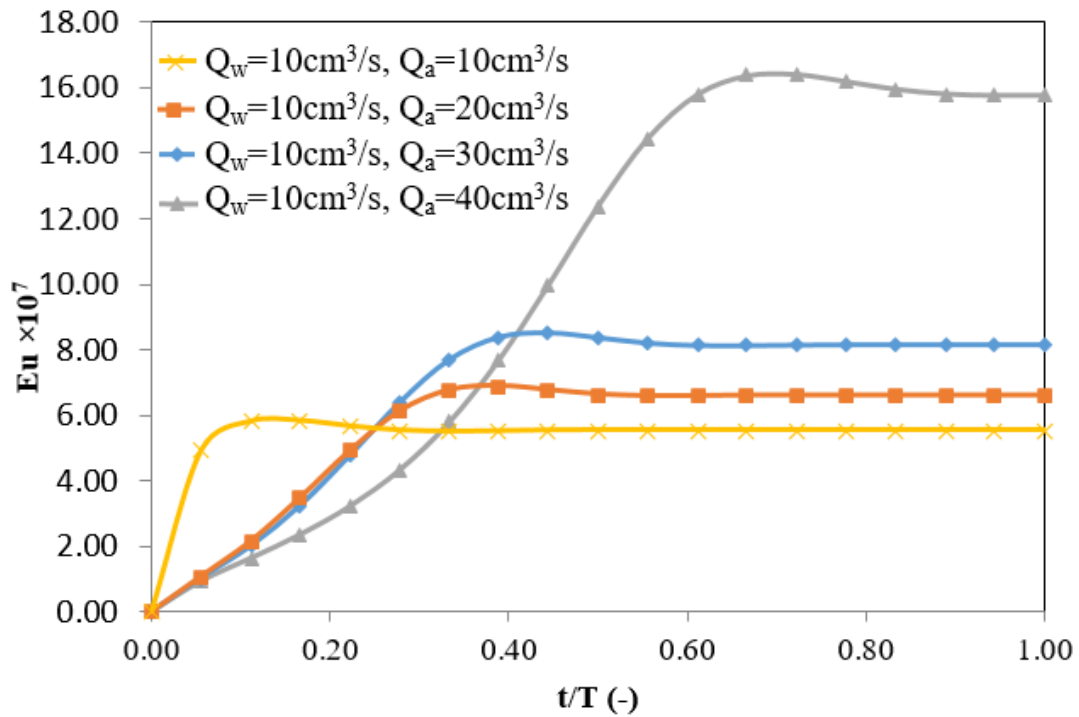


Figure 5.6: The Effect of Air Flow Rate on Injection Pressure.

number and non-dimensional time to make every variable dimensionless. When we make all the variables dimensionless, it is convenient for scaling-up study. We have used different air and water velocities in the simulation. We have varied air and water velocities using the different fraction of air and water in the study. The mixture density and mixture velocity are used in calculating the Euler number. We have considered the proportion or fraction of two phases for calculating the mixture density. For calculating the mixture velocity, we have added both air and water superficial velocities. In calculating Euler number, the changing velocity and density effects were taken into consideration for each case. We investigate the two-phase flow considering water flow rate, $Q_w = 10$ [cm³/s], as constant and changing the flow rate of air, $Q_a = 10$ [cm³/s] to $Q_a = 40$ [cm³/s]. The results are exhibited in the Fig 5.6. The investigation confirms that the steady-state is mainly determined by the flow rate of water while the flow rate of air mainly affects the unstable stage. When a specific

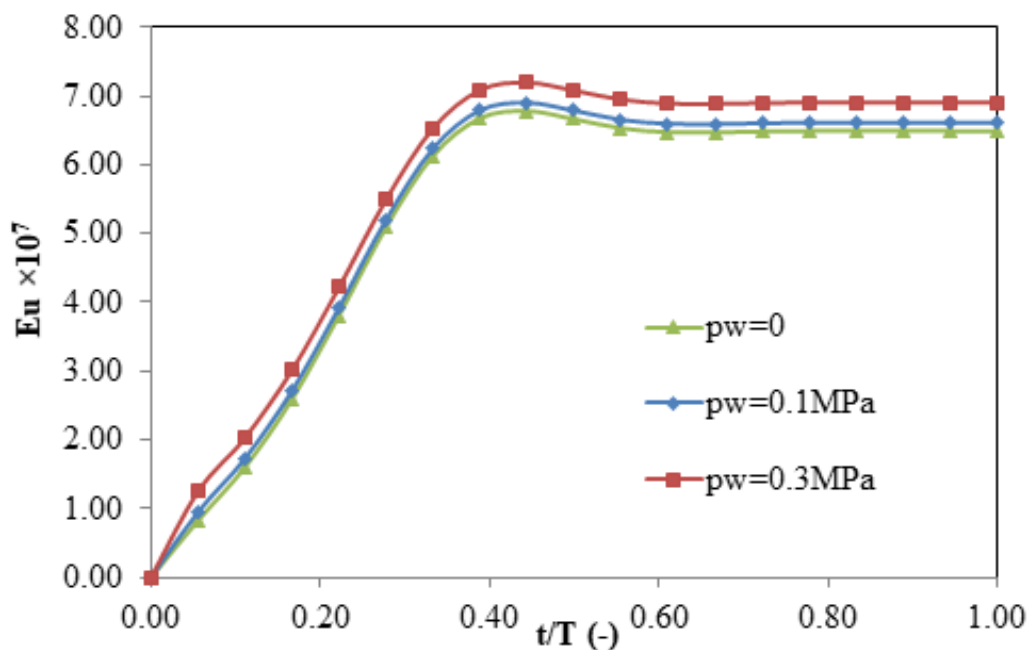


Figure 5.7: The Effect of Back Pressure on Injection Pressure.

volume of water is injected into a sample remains constant and volume of air injected into a sample increases, the time required to be steady-state condition will be shorter. Air helps to reduce the frictional pressure and static pressure loss in the porous medium. The situation can be explained as: the frictional pressure loss is directly proportional to the mixture density and the square of mixture velocity. Thus, increasing gas fraction or velocity helps to reduce the mixture density since the density of air is significantly lower compared to water density (approximately 1000 time less). This significantly lowers the density of the two-phase flow or a mixture of two phases. On the other hand, the mixing of two phases increases the mixture velocity, and this results in significantly way higher frictional pressure loss since the velocity term is squared. Thus, at lower gas phase velocity the frictional pressure loss decreases due to lower density effect. However, at higher gas phase velocity the frictional pressure loss increases due to the square of the mixture velocity term. In this

case, the velocity effect (inertial) supersedes the density effect. Similarly, the hydrostatic pressure loss is directly proportional to the height and density. Thus, increasing air phase with water, significantly reduces the density of the mixture and this helps to reduce static pressure in a medium. Similarly, the back pressure effect is also presented for two-phase flow in Fig 5.7. The backpressure in wellbore has little effect on the pressure buildup profile. The pressure buildup time is mainly affected by the injected fluid, not on the wellbore pressure.

5.6 Conclusion and future work

Based on the present study, the following conclusions can be drawn:

- Fluid flow from hydrocarbon reservoir to perforation tunnel can be conducted using CFD analysis.
- The pressure buildup in the porous medium is greatly affected by gas flow rate, permeability of the medium.
- The wellbore pressure, and porosity have less effect on the pressure buildup profile in a porous medium.
- The dominant factor for the breakthrough of a fluid in a core sample is the gas flow rate.
- Incorporation of gas flow in a porous system reduces hydrostatic pressure loss and less time is required to active the breakthrough time. This numerical study helps to develop a larger scale experimental investigation which is in progress under the authors of the article.

Acknowledgments

J. Alam acknowledges financial support from the National Science and Research Council (NSERC), Canada. M. A. Rahman acknowledges financial support from the National Science and Research Council-discovery grant (NSERC-DG), Canada, RDC Ignite , NL and Seed grant Memorial University of Newfoundland, Canada. M. J. Ahammad acknowledges School of graduate studies, Memorial University of Newfoundland, Canada for scholarships.

Nomenclature

Symbol	Units	Description
B	--	Formation volume factor
h	m	Hight of the reservoir
H	m	Hight of the wellbore
P	psi	Pressure
q	kg/s	Flow rate
s	--	Skin Factor
t	s	Time
u	ms^{-1}	True velocity field of i^{th} competent
c_r	1/psi	Rock compressibility
c_f	1/psi	Fluid compressibility
c_t	1/psi	Total compressibility
g_i	ms^{-2}	Gravitational force along i^{th} direction
P_w	psi	Bottom hole pressure
x_i	m	Axis of i^{th} coordinate

x_j	m	Axis of j^{th} coordinate
u_i	ms^{-1}	Intrinsic velocity field of i^{th} competent
\mathcal{K}	m^2	Permeability of the medium at reservoir area
μ	mPa.S	Viscosity of fluid
ρ	Kg/m^3	Density

Abbreviation

CFD	Computational Fluid Dynamics
Eu	Euler numbers
NSE	Navier-Stokes Equations
PD	Perforation by drilling
PS	Perforation by shooting
EOR	Enhanced Oil Recovery
DAQ	Data Acquisition system

Chapter 6

Numerical simulation of two-phase flow in porous media using a wavelet based phase-field method

Title of the article: *Numerical simulation of two-phase flow in porous media using a wavelet based phase-field method*

Authors: *M Jalal Ahammad*¹, *Jahrul M Alam*², *Mohammad Azizur Rahman*³,
*Stephen D Butt*⁴,

Corresponding author: Jahrul M Alam; email:alamj@mun.ca

Journal of Chemical Engineering Science – Elsevier

Published in volume = 173, pages = 230 – 241, year = 2017.

Abstract: An understanding of the transport and dynamics of two fluids in porous media, as well as the bubbly flow regime, is important for many engineering applications, such as enhanced oil recovery (EOR) method, drilling technology, multiphase production system, etc. In this respect, the dependence of capillary stresses on the excess free-energy of a thin interfacial layer formed by two immiscible fluids is not fully clear, particularly in porous media. Of particular interests are the closure models for interphase forces which often hinder the reliable prediction of the homogeneous flow regime. This article presents a multiphase Computational Fluid Dynamics (CFD) study of bubbles in homogeneous porous media to model the flow of oil and gas, and investigates a closure model that is based on the Allen-Cahn phase-field method, where the capillary stress is derived from the excess free-energy. The governing dynamics is simulated with the volume averaged Navier-Stokes equations extended for multiphase flow in porous media. The equations have been discretized by a wavelet transform method to accurately capture the topological change of the fluid-fluid interface, and have been solved by a unconditionally stable multiphysics CFD solver called the Newton-Krylov method. To validate the closure model for interphase

¹Mathematics and Statistics, Memorial University, Canada, A1C 5S7

²Mathematics and Statistics, Memorial University, Canada, A1C 5S7

³Petroleum Engineering, Texas A& M University, Qatar

⁴Process Engineering, Memorial University, Canada, A1C 5S7

forces, the results of the present phase-field method have been compared with that from experiments, as well as from reference numerical models. An excellent agreement among the results from present phase-field simulations, experiments, and some reference numerical simulations has been observed. The terminal velocity of the rising gas bubble in a liquid saturated porous medium, as well as in a pure liquid has been investigated. The bubble rising velocity in both cases have been compared with respect to the theoretical and experimental results. The study illustrates how the bubble dynamics in porous media depend on the excess free energy of a thin interfacial layer formed by two immiscible fluids.

Keywords: Phase-field method, wavelet method, Navier-Stokes equation, porous medium, bubble dynamics, surface tension.

6.1 Introduction

Numerical modelling of multiphase flow and transport has attracted numerous researchers because of its importance in various scientific and industrial applications (Giorgio *et al.*, 2017; Horgue *et al.*, 2015a; Higdon, 2013). Of particular interests are two-phase flow in and around a wellbore, enhanced oil recovery techniques, and carbon capture and storage projects (e.g. Arzanfudi *et al.*, 2016; Kundu *et al.*, 2016; Rahman *et al.*, 2013). A critical challenge in modelling oil and gas is that the flow rates often cease to remain linear with the pressure gradients in wellbores and in many reservoirs, and the capillary stress becomes important (Wu *et al.*, 2011; Mahdiyar *et al.*, 2011). In particular, near perforation tunnels which are connections between the reservoir and the wellbore (cf. Fig 6.1), a sudden change of the shear stress and the flow direction occurs (Arzanfudi *et al.*, 2016). Molina & Tyagi (2015) considered the Navier-Stokes equation to explain that shear stress associated with the sudden change from horizontal flow in the reservoir to the vertical flow in the wellbore plays an important role in the multiphase flow regime near wellbores. As

the reservoir fluids enter into the wellbore, the liquid phase may remain continuous, but the gas phase may appear as randomly distributed bubbles. In such case, the pressure drop may be described by the bubble velocity, friction factor, and buoyancy (Livescu *et al.*, 2010). In contrast, the presence of bubbles in a reservoir would alter some reservoir properties, such as the macroscopic hydraulic conductivity of the medium, and the pressure drop across a bubble may become a nonlinear function of the fluid velocity. Bubbles may plug some pore channels or fractures and reduce the overall flow rate in a reservoir. The capillary stress plays an important role in bubble dynamics. As discussed below based on the Darcy's equation, bubble dynamics in porous media can be studied by the Buckley-Leverett model, or the pressure profile in the reservoir may be analyzed by the pressure diffusivity equation. In both approaches, the capillary stress is treated implicitly – through the relative permeability. In this article, we investigate the dynamics of an isolated bubble to understand how the capillary stress depends on the excess free-energy of a thin interfacial layer that is formed between two moving immiscible fluids in a homogeneous porous medium. We have considered the Allen-Cahn phase-field method to define the capillary stress as a function of the volume fraction (C) of one of the two fluid phases. We have incorporated the capillary stress explicitly into the volume averaged Navier-Stokes equation, where the resistance of porous media is expressed as a quadratic function of the fluid velocity. We have compared the results from the phase-field simulations with that from the experiments to validate the proposed phase-field model of multiphase flow in porous media. Let us now review two other approaches, which do not account for the capillary stress explicitly.

Using the linear theory based on Darcy's experiment and the classical Gibbs theory of capillarity, a two-phase flow can be described by the following Buckley-Leverett model,

$$\frac{\mu_i}{\mathcal{K}_i} \mathbf{u}_i = -\nabla P_i + \rho_i \mathbf{g}, \quad \frac{\partial s_i}{\partial t} + \nabla \cdot (s_i \mathbf{u}_i) = 0,$$

where μ_i , \mathcal{K}_i , \mathbf{u}_i , P_i , ρ_i , and s_i are viscosity, relative permeability, velocity, pressure, den-

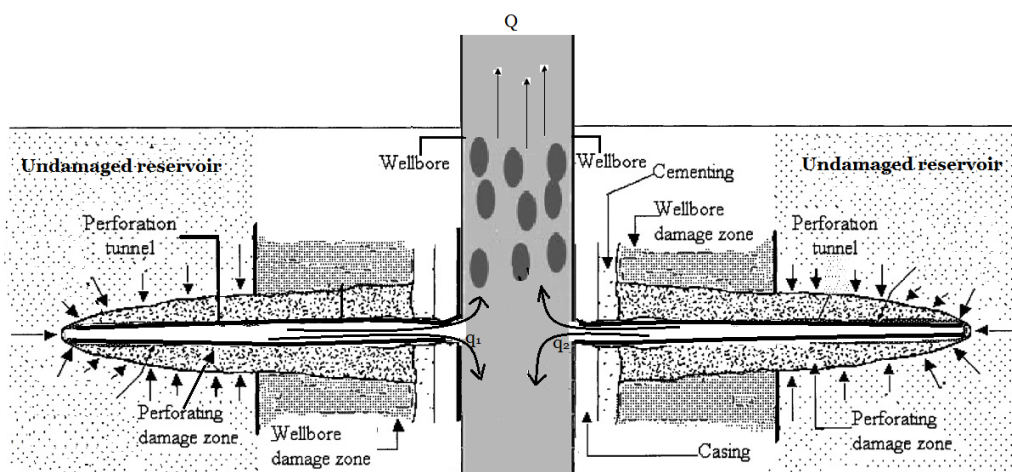


Figure 6.1: A schematic illustration of an oil reservoir, where a vertical wellbore with perforation tunnels are also shown. The figure is adapted from a similar illustration given by Rahman *et al.* (2007b). Note that the fluid flow is vertical in the wellbore and horizontal in the reservoir. Bubbles may be present in the wellbore or in the reservoir. When the reservoir fluid enters into the wellbore, the flow rate is affected by the formation damage near the perforation tunnels.

sity, and saturation of phase i ($= l, g$). In such a model, the details of the capillary phenomena are not resolved individually. Instead, capillary phenomena are lumped into the phenomenological relative permeability, \mathcal{K}_i , which can be measured on core samples in the laboratory. While this approach is pragmatic and fit-for-purpose for many of the operational aspects, one notes that the surface tension has not been accounted explicitly in the Buckley-Leverett model. The linear theory fails to mimic any contribution of the non-Darcy flow regime (Wu *et al.*, 2011; Molina & Tyagi, 2015). Further details can be found from the work of Skjetne *et al.* (1999); Lee *et al.* (1987); Guppy *et al.* (1981); Tek *et al.* (1962), and Swift *et al.* (1962). Based on the evidences of flow patterns in fractures and near wellbores, the Forchheimer equation,

$$\frac{\mu_i}{\mathcal{K}_i} \mathbf{u}_i + \frac{C_F \rho_i}{\sqrt{\mathcal{K}_i}} |\mathbf{u}_i| \mathbf{u}_i = -\nabla P_i + \rho_i \mathbf{g},$$

was proposed to replace the momentum equation in the Buckley-Leverett model, where C_F is the Forchheimer coefficient. The second term on the left hand side of the Forchheimer equation accounts for the frictional pressure loss when fluids flow in reservoirs or through a narrow annulus.

Alternatively, a pressure analysis technique was derived from the conservation of mass, the Darcy's equation, and the equation of state (Khadiji & Soltanieh, 2014b; Dake, 1983). The single-phased pressure diffusivity equation,

$$\frac{\phi \mu c_t}{\mathcal{K}} \frac{\partial P}{\partial t} = \frac{1}{r} \frac{\partial P}{\partial r} + \frac{\partial^2 P}{\partial r^2}$$

forms the foundation of pressure analysis techniques in petroleum engineering, where c_t is the gas compressibility. In practice, wellbores have a damaged zone with reduced permeability resulting from oil well drilling – known as skin effect, and the pressure diffusivity equation often fails to model such wellbores.

This brief review indicates that current understanding of multiphase flow in porous media is not complete. For example, the methods stated above are often found inadequate to

analyze the skin effect in the perforation zone, as well as bubbly flow in fractured porous media. To take advantage of the CFD simulation, it is necessary to understand how to model the stresses due to the interaction among liquid, gas, and solid (e.g. Kundu *et al.*, 2016; Molina & Tyagi, 2015). According to the CFD literature, the phase-field method is a relatively new technique, which is very similar to the volume of fluid (VOF) method. We know that the VOF method models the surface tension based on the curvature of the interface between two fluids, where the wetting phenomena is imposed as a boundary condition on the solid substrates (Afsharpoor *et al.*, 2012). In contrast, the phase-field method models the surface tension and the wetting phenomena based on the chemical potential, which considers a balance of thermodynamic free energy (Kusumaatmaja *et al.*, 2016; Feng *et al.*, 2007; Feng, 2006). In this article, we demonstrate a phase-field modelling approach of simulating a single bubble rising in a fluid, as well as in a fluid saturated porous media. A comparison between the present phase-field simulation with an equivalent experimental study has been considered to indicate the performance of the phase-field approach for an accurate estimate of pressure jump across a fluid-fluid interface. We then extend the phase-field method to simulate bubble dynamics in porous media. We use experimental data to validate the present results and discuss a methodology that provides an overall estimate of the surface tension and resistive forces active on a bubble that moves in a fluid saturated porous media. Comparisons among numerical simulation, mathematical analysis, and experimental data have been used to validate the proposed CFD simulation of multiphase flow phenomena.

Section 6.2 provides a brief outline of the technical details that are necessary to implement the present methodology. In this section, we have discussed the phase-field method that conserves mass and its benefits to incorporate surface tension directly into the Navier-Stokes equation *via* a modification of the deviatoric stress. Section 6.3 outlines the present numerical approach, as well as discusses how our method can be incorporated into an ex-

isting CFD code. Based on a classical test case that is commonly used to study multiphase flow, section 6.4 considers two sets of experimental data to validate the methodology outlined in our work. While showing a good agreement between experimental results and our numerical results, we have also discussed a mathematical formulation of the combined forces on the fluid-fluid interface that evolves through a porous media.

6.2 Simulation methodology

6.2.1 Multiphase flow in porous media

To simulate the multiphase flow in a porous medium, the Navier-Stokes equation along with the conservation of mass and the Allen-Cahn phase field equation have been solved for the intrinsic average of the velocity, \mathbf{u} . For convenience, we have adopted the symbol \mathbf{u} to replace the usual symbol $\langle \mathbf{u} \rangle$ for the average. We have simulated the flow of two immiscible fluids of different densities ($\rho_g < \rho_l$) and viscosities ($\mu_g < \mu_l$). The capillary stress is derived from the excess free-energy of the system accumulated in a thin interface of finite thickness (ϵ) between two fluids. The volume fraction, C , of one of the fluids is used as a phase indicator, which takes a value 1 for one fluid and 0 for the other fluid, where the interface of free-energy is defined by $C \in [0.5 - \epsilon/2, 0.5 + \epsilon/2]$. In other words, the saturation of one phase is C and the other phase is $1 - C$. This representation of the two-phase flow is similar to the volume of fluid method, as well as equivalent to the Buckley-Leverett method. Peaceman & Rachford (1962) presents a detailed derivation of how the individual saturation (s_i) in the Buckley-Leverett model is equivalent to the phase indicator function C (see also, Chen *et al.*, 2006c). The density, the viscosity, and the velocity of the phase-field system are given by $\rho = \rho_g C + \rho_l(1 - C)$, $\mu = \mu_g C + \mu_l(1 - C)$, and $\mathbf{u} = \mathbf{u}_g C + \mathbf{u}_l(1 - C)$ (Antanovskii, 1995).

The simultaneous flow of a liquid and a gas behaves as an incompressible flow if the corresponding Mach number (the ratio of the velocity to the sound speed) is less than 0.3 (Kundu *et al.*, 2012; Antanovskii, 1995). Thus, the conservation of mass becomes

$$\nabla \cdot \mathbf{u} = 0.$$

Since the length scale characterizing the pore structures of the porous medium is much less than that of the REV, as well as the computational mesh, the porous medium is represented by a packed spheres. In this approach, the viscous drag exerted by the spheres is equivalent to the volumetric flow rate that is linearly related to the pressure gradient in the Darcy's equation (Bear, 1972), and the form drag exerted by the spheres is equivalent to the resistive force in the Forchheimer equation (deLemos, 2006). For each phase, the porous medium is modelled in terms of the total resistive (drag) force

$$f_i = - \left[\frac{\nu}{\mathcal{K}} + C_F \frac{|\mathbf{u}|}{\sqrt{\mathcal{K}}} \right] \mathbf{u},$$

where $\mathcal{K}[\text{m}^2]$ is the effective permeability of the model porous medium, ν is the kinematic viscosity and C_F is a constant. For spheres of diameter d (*e.g.* characteristic pore-scale), both \mathcal{K} and C_F can be estimated using Ergun's methodology (Ergun, 1952) such that $C_F = F/\sqrt{\mathcal{K}}$,

$$\mathcal{K} = \frac{d^2 \phi^3}{(1 - \phi)^2}, \quad F = \frac{1.75d}{150(1 - \phi)},$$

and ϕ is the porosity of a porous medium. A technical details of the above model for single-phase flow in porous media is documented by deLemos (2006), Breugem & Rees (2006) and Bear (1972). Following Antanovskii (1995) and Breugem & Rees (2006), we have derived the following 'intrinsic average' of the momentum equation for a two-phase flow in porous media:

$$\rho \frac{D\mathbf{u}}{Dt} = -\nabla P + \nabla \cdot (\mu \nabla \mathbf{u} + \mu \nabla \mathbf{u}^T) - \frac{\phi \mu \mathbf{u}}{\mathcal{K}} - \frac{C_F \phi |\mathbf{u}| \mathbf{u}}{\sqrt{\mathcal{K}}} + (\rho_l - \rho_g) \mathbf{g} - \nabla \cdot \boldsymbol{\tau}_\sigma, \quad (6.1)$$

where

$$\frac{D\mathbf{u}}{Dt} = \frac{\partial\mathbf{u}}{\partial t} + \mathbf{u} \cdot \nabla\mathbf{u},$$

$\nabla\mathbf{u}^T$ denotes the transpose of the velocity gradient tensor $\nabla\mathbf{u}$, and $\boldsymbol{\tau}_\sigma = \sigma\kappa\epsilon^2\nabla C \otimes \nabla C$ denotes the stress tensor contributed by the surface tension.

6.2.2 The phase-field method and the surface tension

6.2.2.1 Dynamics of the two-phase interface

The phase-field method is a relatively new approach for two-phase flow simulation (Vasconcelos *et al.*, 2014; Kim, 2012; Provatas & Elder, 2011; Feng *et al.*, 2007; Jacqmin, 1999; Antanovskii, 1995). It employs the Navier-Stokes equations to accurately simulate the motion of a contact line (Cai *et al.*, 2015) or to directly simulate pore-scale flow of two fluids (Alpak *et al.*, 2016). There are two versions of the phase-field method. The Cahn-Hilliard method uses a fourth order diffusion (e.g. Jacqmin, 1999) and the Allen-Cahn method uses a second order diffusion (e.g. Vasconcelos *et al.*, 2014). Both approaches preserve the immiscibility of fluids by conserving mass of each phase. This article has adopted the Allen-Cahn method because its numerical treatment is more efficient with respect to the Cahn-Hilliard method.

In phase-field methods, the total free-energy is defined by the functional

$$\mathcal{W} = \int_{\Omega} \left(\frac{\epsilon^2}{2} |\nabla C|^2 + f(C) \right) d\Omega, \quad (6.2)$$

where ϵ is the thickness of the interface containing excess free-energy of the two phase system, and the double well potential takes the form $f(C) = C^2(1 - C)^2$. The dynamics of the interface is then governed by the evolution of $C(\mathbf{x}, t)$ according to

$$\frac{\partial C}{\partial t} + \mathbf{u} \cdot \nabla C = \mathcal{T}\mu^c + \frac{\mathcal{T}}{|\Omega|} \int f'(C) d\Omega, \quad (6.3)$$

where $1/\mathcal{T}$ is called the elastic relaxation time-scale and μ^c is called the chemical potential, which is defined by

$$\mu^c = -\frac{\delta W}{\delta C} = \epsilon^2 \nabla^2 C - f'(C)$$

is called the chemical potential (Yang *et al.*, 2006). The last term in (6.3) ensures the conservation of C (Vasconcelos *et al.*, 2014). Clearly, the chemical potential, μ^c , vanishes away from the interface. In other words, the phase-field equation (6.2) approaches to the VOF equation away from the interface (Alpak *et al.*, 2016; Hirt & Nichols, 1981).

6.2.2.2 Surface tension

The surface tension across a fluid-fluid interface can be obtained from the Young-Laplace equation

$$P_g - P_l = \sigma \kappa,$$

where σ [N/m] is the surface tension and κ [1/m] is the local curvature of the interface. (Chen *et al.*, 2006a). Thus, the stress acting on an arbitrary fluid surface must account for an additional component $\sigma \kappa$ in a two-phase system in such a way that the surface tension does not alter the stress tensor in the region that is away from the fluid-fluid interface. An accurate representation of stress in a two-phase system is a potential advantage of the phase-field theory. Antanovskii (1995) and Jacqmin (1999) provide a detailed derivation of stress that is modified by the surface tension. For the present Allen-Cahn method (cf. Vasconcelos *et al.*, 2014), the assumptions remain the same as the assumptions considered by Jacqmin (1999) for the Cahn-Hilliard method. In the Navier-Stokes equations, the total stress for a two-phase flow is thus given by (*e.g.* Eq 6.1)

$$\nabla \cdot \boldsymbol{\tau} = \nabla \cdot [-P\mathbf{I} + \mu(\nabla \mathbf{u} + \nabla \mathbf{u}^T)] + \sigma \kappa \mu^c \nabla C,$$

where the last term accounts for the divergence of stress due to the surface tension, which has been derived using the variational derivative of \mathcal{W} (cf. eq. 6.2) and expanding $\nabla \cdot$

$(\nabla C \otimes \nabla C)$. In other words, the last term in eq (6.1) is given by

$$\nabla \cdot \tau_\sigma = -\sigma \kappa \mu^c \nabla C.$$

We have employed the above theory to simulate a two-phase flow of a gas and a liquid by solving Eqs (6.1-6.2) along with the conservation of mass, $\nabla \cdot \mathbf{u} = 0$.

6.3 Computational procedures

This section outlines the discretization method and the solution techniques, where the mathematical details are not repeated, and can be found from the cited articles. The governing equations are discretized on a mesh that is a collection of non-overlapping rectangles with n_x cells in the x direction and n_y cells in the y direction.

6.3.1 Wavelet based CFD simulation

The wavelet method has the multi-resolution properties, and is often called ‘numerical microscope’ in signal and image processing (Mallat, 2009). Recently, the efficiency of wavelet-based CFD simulation techniques has been demonstrated by several authors (Alam, 2015; Alam *et al.*, 2012; Sun *et al.*, 2012; Schneider & Vasilyev, 2010). In particular, the wavelet method is known to capture the evolution of a thin interface accurately. There are three primary approaches of implementing the wavelet method: *i*) the wavelet collocation method based on the nodal approximations (Jameson, 1993; Mehra & Kumar, 2005; Alam *et al.*, 2014); *ii*) the wavelet method based on the wavelet expansion coefficients (Liandrat & Tchamitchian, 1990; Mehra & Kumar, 2005); and *iii*) the wavelet method based on finite difference discretization and dynamically adaptive mesh refinement (Vasilyev & Bowman, 2000; Alam *et al.*, 2012). The present method falls under the category *i*) – a detailed implementation of which is given by Alam *et al.* (2014), and is not reproduced here for brevity.

Briefly, it forms a trial solution based on the wavelet expansion series, which extends the weighted residual collocation method presented by Finlayson (2013). The spatial truncation error of the present wavelet method is $\mathcal{O}(\Delta x^{2p})$ ($p = 3$ for the present study), and is also second order in time (see also, Walsh & Alam, 2016). The method is unconditionally stable, which means that if Δx is reduced to improve spatial truncation error, it is not necessary to reduce Δt unless there is a need of improving temporal truncation error. The method treats the coupling of velocity, pressure, and phase-field through a Newton-Krylov iterative solver. It is worth mentioning that the overall computational scaling of this wavelet method is asymptotically optimal, *i.e.* its computational complexity is $\mathcal{O}(\mathcal{N})$ for a mesh of \mathcal{N} grid points.

6.3.2 Simulation and parameters

For the purpose of illustrating bubble dynamics and understanding the effect of capillary stress and resistive force of the porous medium, we have simulated multiphase flow in an isolated porous block so that all other features of the reservoir do not influence the results. First, we have considered two sets of phase-field simulations. In one simulation, we have turned off the resistive force of the porous medium; in other simulation, we vary the resistive force. Thus, we gain an understanding of how the capillary stress affects the multiphase flow in porous media. Second, we have considered the result of an equivalent numerical simulation to understand the performance of the proposed CFD technique. Third, we have considered the result from an experiment that deals with air bubble rising in a porous medium saturated by water. The comparison between the phase-field simulation and the experiment illustrates that capillary stress is a function of the excess free-energy of the multiphase flow. Fourth, we have considered the balance of forces acting on a bubble to analytically predict the terminal velocity of a rising bubble. Phase-field solution is

compared with the analytical solution.

For all simulations, the model region is initially saturated with a fluid of density ρ_l and viscosity μ_l . We have discussed our results with respect to dimensionless parameters, namely the Reynolds number $Re = UD/\nu$, the Darcy number $Da = \mathcal{K}/D^2$, and the Bond number $Bo = gD^2\rho_l/\sigma$, where $\nu = \mu_l/\rho_l$ and D is the characteristic length scale.

6.4 Numerical simulations

Let us begin with a numerical validation of the phase-field method in section 6.4.1, and demonstrate that the macroscale surface tension computed from the chemical potential is indeed the microscale surface tension that satisfies the classical Young-Laplace equation.

6.4.1 Macroscale modelling of surface tension

The Young-Laplace equation states a balance of normal stresses between two stationary fluids which meet at an interface. In the phase-field method, the Young-Laplace equation is applied at macroscale on an interface of thickness ϵ . When the mesh resolution, Δ , and the thickness of the interface, ϵ , are about the same order of magnitude, the Young-Laplace equation would be satisfied by the phase-field method. Hua & Lou (2007) observed numerically that a further reduction of mesh resolution is not necessary to satisfy Young-Laplace equation. When the mesh resolution is greater than the thickness of the interface, there is a net imbalance of surface forces, and the total stress tensor is not resolved because Young-Laplace equation is not satisfied.

6.4.1.1 Test case

To demonstrate the phase-field modelling of pressure loss by capillary friction, we have examined the surface tension by simulating a rising air bubble in a tube of diameter 10 cm, saturated with water. To understand the effect of surface tension, we have turned off the resistive force of the porous medium. Fig 6.2(a) displays a vertical cross section of the tube at $t = 0$, where a bubble is formed with 65.5 ml air, and is visualized with a color filled contour plot. We have used $C = 1$ (red) to denote the fluid of density $\rho_g = 1.2 \text{ kg/m}^3$ (air), and $C = 0$ (yellow) to denote the fluid of density $\rho_l = 997 \text{ kg/m}^3$ (water). The numerical simulation has been repeated under the same physical and numerical conditions except the mesh has been refined. Four meshes are labelled with respect to number of cells in the horizontal and vertical directions, and are denoted by R1(32×64), R2(64×128), R3(128×256), R4(256×512).

6.4.1.2 Observation

The outcome of this investigation is depicted in the Fig: 6.2(b – e). The results reported in Fig 6.2 show an imbalance of capillary pressure within and out of the bubble, which alters the shape of the bubble until when the size of computational cells, Δ , has been reached to about the same order of magnitude as the thickness of the phase-field interface. A careful comparison between four contour plots in Fig 6.2(b – e) indicates that the discrepancy may not be primarily because of the numerical truncation error (see also Hua & Lou, 2007). In contrast, the coarser resolutions are insufficient to resolve the surface tension. To gain a quantitative understanding, we have plotted the contours of the moving interface at $C = 0.5$ in Fig 6.3, showing the terminal bubble shapes at each resolution. Clearly, the contour at the coarsest mesh R1(32×64) has no wiggles or oscillations, which indicates that the solution on the coarsest mesh has converged with inaccurate physics. The phase-field im-

plementation of the Young-Laplace equation is settled gradually as the mesh is refined. Based on the contour plots in Fig 6.3, the Young-Laplace equation is satisfied on two highest resolution meshes. This result indicates that surface tension applied on the phase-field interface of thickness, $\epsilon/D = 0.022$, is accurately resolved on a mesh with $\Delta/D = 0.015$ in R3(128×256), which is a near optimal balance between the CPU time and the memory (Jacqmin, 1999; Vasconcelos *et al.*, 2014). We also note that both the memory and the CPU time increased approximately linearly for the present numerical algorithm when we had switched to the higher resolution $\Delta/D = 0.0075$ in R4(256×512).

6.4.1.3 Comments on the terminal bubble shape

Fig: 6.4 compares time series of the terminal velocity for the rising bubble at various resolutions. The results show that the velocity increases linearly until about $t = 0.5$ and the time series of the velocity are in agreement for until about $t = 2$. When the bubble pressure is lost by friction, a temporal fluctuation is seen in the velocity time series at the lowest resolution R1(32×64). The velocity of the bubble reaches a steady state, showing a terminal velocity in agreement with $U \propto \sqrt{gD}$, except at the coarsest resolution R1.

6.4.2 Experimental validation of the bubble dynamics

Let us consider the first principle conservation law to understand the pressure profile in a vertical tube based on the multiphase flow mechanism. The momentum equation (6.1) may be reduced to

$$u \frac{\partial v}{\partial x} + v \frac{\partial v}{\partial y} = -\frac{1}{\rho_l} \frac{\partial p}{\partial y} + \frac{\mu_l}{\rho_l} \frac{\partial^2 v}{\partial x^2}$$

for the liquid phase around the bubble. When the bubble rises without changing its shape, the liquid flow around the bubble possess the character of a laminar boundary layer. As the interface is approached, the liquid flow tends to the Stokes flow regime. The laminar

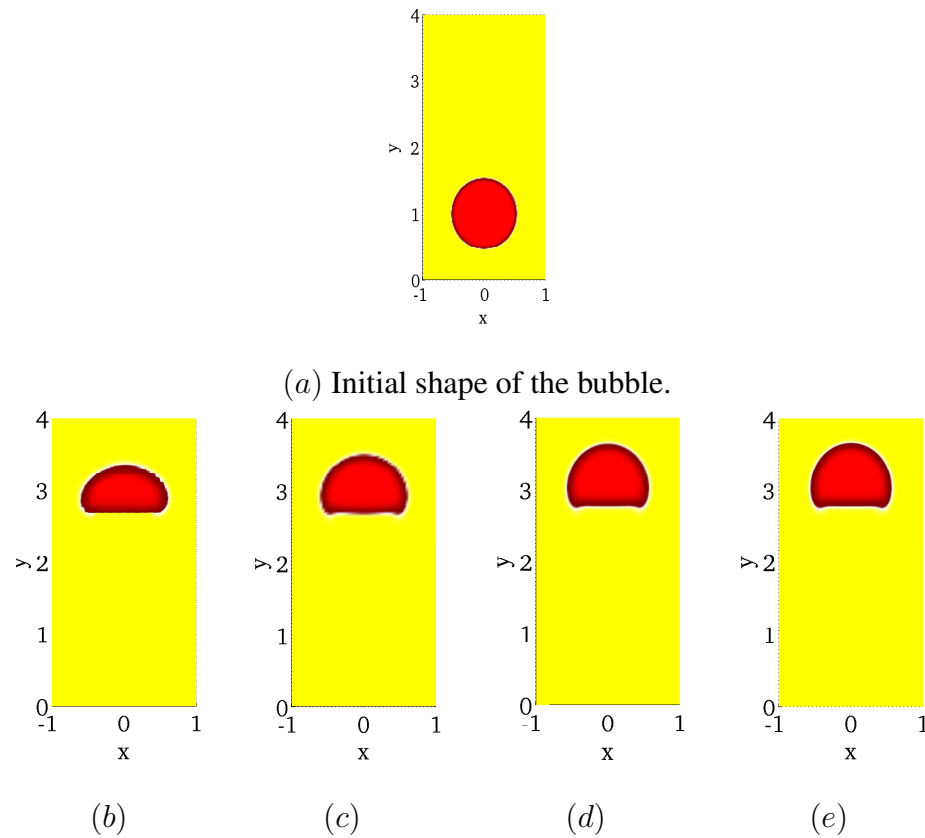


Figure 6.2: Temporal evolution of a rising bubble in a liquid for various meshes of resolutions: (a) R1(32×64), (b) R2(65×128), (c) R3(128×256), (d) R4(256×512). All the cases are at the same time, $tD/W = 7.4$.

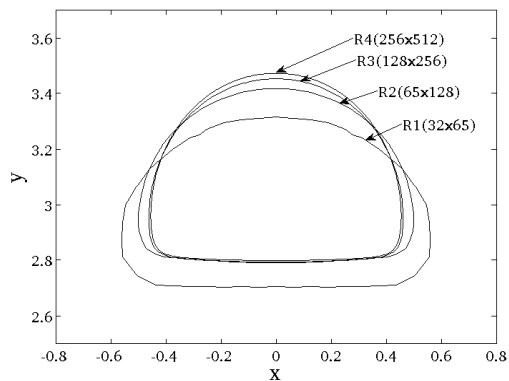


Figure 6.3: Contour line plot of the simulations presented in Fig 6.2. The results represent how accurately the interface between two fluids have been resolved by various resolutions.

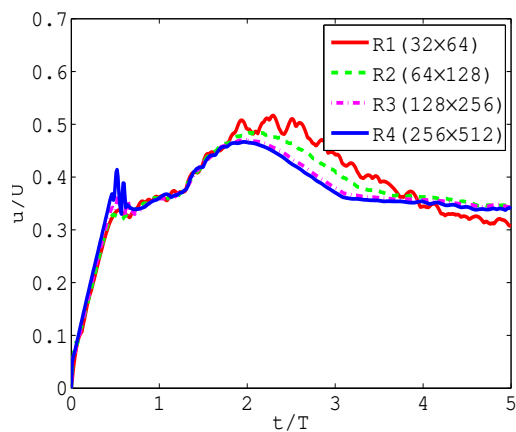


Figure 6.4: Time series of the velocity of the simulation presented in Fig 6.2. The results represent the convergence of the approximate solutions subject to the surface tension and truncation error.

boundary layer theory indicates that the upward rising bubble would have $\frac{\partial^2 v}{\partial x^2} > 0$ on the interface for the lower half of the bubble, and thus, $dp/dy > 0$. As a result, $v(x)$ tends to have a local minima near the center of the bubble, when pressure rises along the vertical direction. Hua & Lou (2007) illustrates that a rising bubble may feel a jet force beneath it from the surrounding liquid. In other words, frictional pressure loss from rising bubble contribute to the ‘adverse’ vertical pressure gradient. Following sections demonstrate this hypothesis experimentally and numerically.

6.4.2.1 Experimental data

Bhaga & Weber (1981) provides an experimental study on the shape regimes and terminal velocities of a bubble that is rising in a viscous liquid, where the flow field around a bubble was visualized with a hydrogen tracer technique. The shape regimes observed experimentally by Bhaga & Weber (1981) was also studied numerically by Hua & Lou (2007). These results indicate when the viscous force (or the surface tension) is relatively strong, the bubbles remain spherical. The shape regimes of the rising bubbles help the understanding of the pressure loss due to friction and entrainment of surrounding liquid. As it was observed by Bhaga & Weber (1981) (see Fig 13 therein), friction and entrainment of surrounding liquid plays a dominant role on the terminal shape of bubbles.

6.4.2.2 Numerical simulations

In Fig 6.5, we have compared the shape of a rising bubble among the experimental work of Bhaga & Weber (1981), the numerical simulation of Hua & Lou (2007), and the present numerical simulation. Note that, the results in Fig 6.5 may not be considered for a one-to-one comparison. In contrast, we see clearly that the liquid pushes beneath the bubble like a jet because the bubble pressure has been lost due to friction with the surrounding liquid.

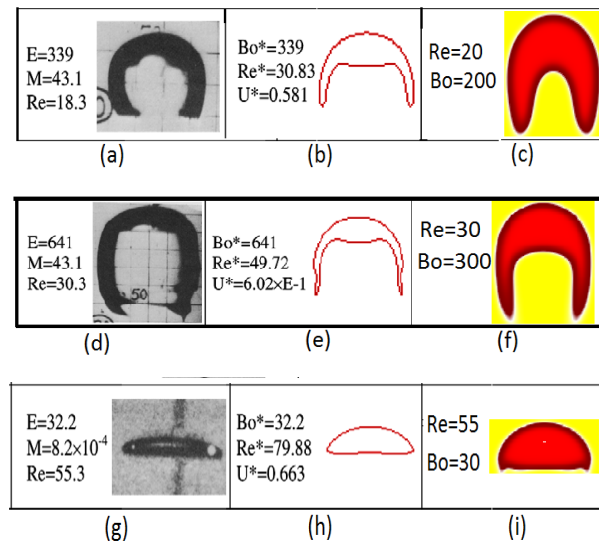


Figure 6.5: Terminal shapes of the rising bubble in a liquid. (a), (d) and (g) are plots of the experimental results provided by Bhaga & Weber (1981). (b), (e) and (h) are plots of corresponding numerical results provided by Hua & Lou (2007). (c), (f) and (i) are plots of numerical results present CFD simulation. Although the physical conditions and parameters are not exactly the same for three cases, the comparison supports findings of ‘adverse’ pressure gradient in the wellbore.

Recall, the viscous force dominates over the inertia force when $Re < 1$. Similarly, the surface tension dominates over the buoyancy force when $Bo < 1$. Bhaga & Weber (1981) provides a characteristic flow for bubble dynamics based on the Reynolds number and the Bond number.

In order to gain a better idea, we have considered a numerical study with $Re = 5, 10,$ and 20 . For each Re , we have also varied the Bond number, namely, $Bo = 5, 10, 20, 50,$ and 100 . We have noticed that the pressure occurs for Bond number ≥ 5 if Re is fixed at 20 . Similar pressure loss is seen for $Re \geq 5$ if the Bond number is fixed at 100 . This simulation has been presented in Fig 6.6, where we have also compared the present simulation with that from (Hua & Lou, 2007). Note that, the buoyancy force may be strong compared to the surface tension in the wellbore during the period of primary recovery. Thus, the present phase-field simulation of two-phase flow would help to characterize the wellbore pressure profile if the gas flow in the wellbore takes the form of dispersed bubbles.

6.4.3 Bubble dynamics in porous media

In this section, we consider the interaction among the buoyancy force, the surface tension, and the frictional force due to the porous medium. We have presented a simplified mathematical expression to describe the balance among these three forces. We have solved the Allen-Cahn Navier-Stokes equation to estimate the effect of these three forces. A comparison between the numerical simulation and the mathematical derivation indicates that the derived mathematical model is appropriate under the assumptions adopted.

6.4.3.1 Two-phase flow simulation in a porous medium

The setup of the simulation is similar to the case presented in section 6.4.1.1 (*here-in-after*, bubble in a clear medium). For bubbles in a porous medium, the solid phase is mod-

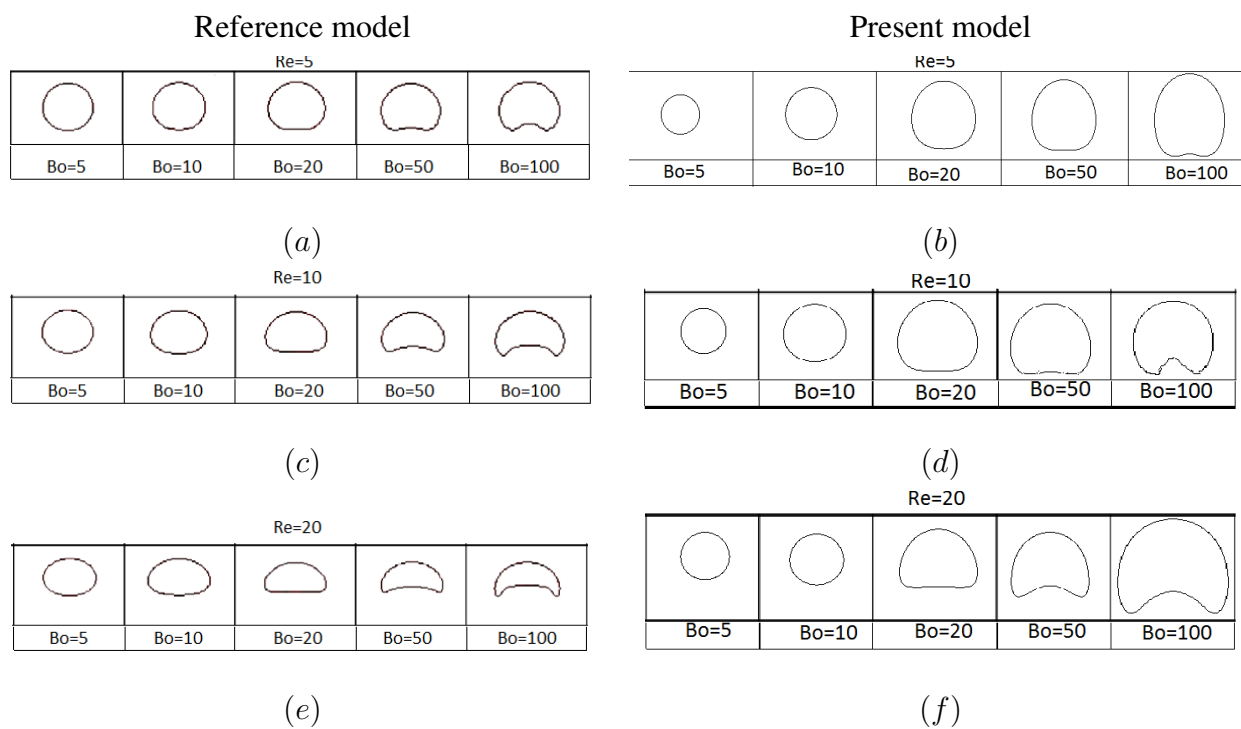


Figure 6.6: Terminal shapes of a rising gas bubble in a liquid. (a), (c) and (e) are plots from the reference model provided by Hua & Lou (2007). (b), (d) and (f) are corresponding plots from the present CFD simulation. Although the modelling technique and the numerical method are not the same in both cases, the comparison supports the findings of the two-phase flow modelling approach considered in the present work.

elled by the frictional force in Eq (6.1), which can be characterized by the Darcy number $\mathcal{D}a = \mathcal{K}/D^2$. A large Darcy number implies a large relative permeability, and *vice versa*. Here, $\sqrt{\mathcal{K}}$ represents a characteristic length for the gap between the solid phase and the fluid phase. In the limit of $\sqrt{\mathcal{K}} \gg D$ and if the bubble is approximately spherical, the frictional force on the bubble is primarily due to the surrounding fluid, which can be described adequately by the Stokes approximation (Kundu *et al.*, 2012). In the opposite limit, the solid phase is very close to the fluid phase, and the fluid particles within a bubble experience simultaneously a drag force parallel to the direction of mean flow and a lift force along the transverse direction. Further details of this phenomena was studied experimentally by Takemura *et al.* (2002).

We have simulated a spherical bubble of diameter D in a fluid saturated porous medium with porosity, $\phi = 18\%$. The observation of this simulation is reported in Fig 6.7. The data has been post-processed and visualized as a color filled contour plots in Fig 6.7(a-d) for four values of the Darcy numbers, $\mathcal{D}a = 9 \times 10^{-3}$, $\mathcal{D}a = 9 \times 10^{-4}$, $\mathcal{D}a = 9 \times 10^{-5}$, and $\mathcal{D}a = 9 \times 10^{-7}$. The snapshots in Fig 6.7 are taken when the bubble has travelled approximately a distance of $2D$. We notice that the bubble retains a spherical shape approximately for the highest Darcy number considered here (Fig 6.7a). When the Darcy number decreases the lift force becomes important (e.g. Takemura *et al.*, 2002), and one notices that the bubble deforms, e.g. Fig 6.7b to 6.7d. As we have demonstrated in case of a clear medium, a bubble deforms due to the change of local viscous stress ($Re > 1$) and capillary forces ($Bo > 1$). In the present case, since $\mathcal{D}a$ is the only controlled parameter, the deformation of the bubble in Fig 6.7 is primarily due to the frictional force of the porous medium.

6.4.3.2 Momentum balance and frictional force of porous media

Let us consider a bubble of diameter $D = 2r$ (r , radius) and density ρ_1 , which rises in a homogeneous and isotropic porous medium, and the medium is saturated initially with a

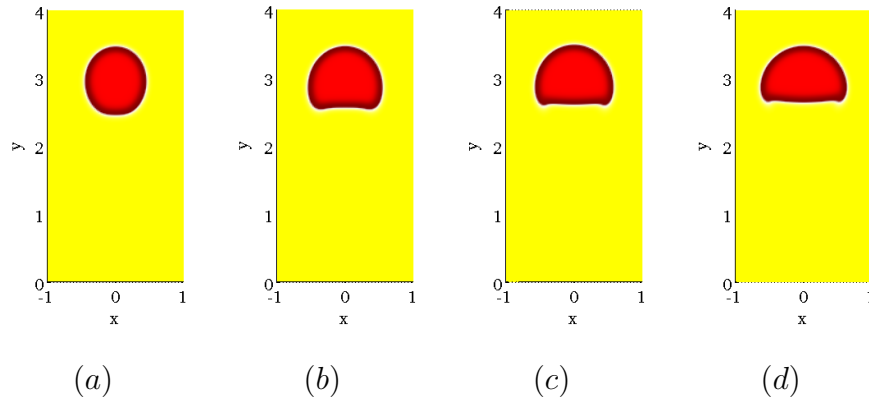


Figure 6.7: The Effects of permeability on the shape of the rising bubbles. Here, all the parameters including porosity, $\phi = 18\%$ for the simulations are same except the Darcy numbers. The results (a) for the $\mathcal{D}a = 9 \times 10^{-3}$ with $t = 6.85$, (b) for the $\mathcal{D}a = 9 \times 10^{-4}$ with $t = 6.9$, (c) for the $\mathcal{D}a = 9 \times 10^{-5}$ with $t = 7.0$ and (d) for the $\mathcal{D}a = 9 \times 10^{-7}$ with $t = 8.9$.

fluid of density ρ_2 . The frictional force of the porous medium is given by $f_p = -(\mu/\mathcal{K} + F\rho v/\mathcal{K})v$ in the present model (based on the Forchheimer equation), which can also be expressed using the expression of \mathcal{K} and \mathcal{F} given by (see Ergun, 1952)

$$\mathcal{K} = \frac{d^2\phi^3}{150A(1-\phi)^2} \quad \text{and} \quad F = \frac{1.75d}{150(1-\phi)}.$$

According to Bear (1972), an equivalent radius of pore throat for this porous medium is $R = (2\sqrt{3} - 3)d/6$. These information can be used to estimate the terminal velocity of the bubble, using the vertical component of the momentum balance Eq (6.1), which takes the form

$$\frac{4}{3}\pi r^3 \rho_1 \frac{dv}{dt} = (\rho_2 - \rho_1) \frac{4}{3}\pi r^3 g - 2\pi R \sigma \sin \theta - A \left[\frac{150v(1-\phi)^2\mu}{d^2\phi^3} + \frac{1.75\rho_1 v^2(1-\phi)}{d\phi^3} \right] \frac{4}{3}\pi r^3.$$

Here, the first two terms on the right hand side represents the buoyancy force and the surface tension, respectively, and the term within $[\dots]$ represents the frictional force. The

above equation can be rearranged as $dv/dt = av^2 + bv + c$, and from which the terminal velocity v_T is then given by

$$av_T^2 + bv_T + c = 0.$$

One may employ a symbolic computing software, such as MAPLE, and obtain the following form of the terminal velocity

$$v_T = \frac{(1 - \phi)\mu}{d\rho_1} \left[-42.86 \pm \sqrt{1836.74 - \frac{0.57}{A} \left(\frac{\rho_1 d_p^3 \phi^3}{(1 - \phi)^3 \mu^2} \right) \left(\frac{3R}{2r^3} \sigma \sin \theta - (\rho_2 - \rho_1)g \right)} \right].$$

Let us now examine the above simplified mathematical expression using the proposed phase-field simulation.

6.4.3.3 Numerical and experimental validation of the terminal velocity of a bubble

Experimental data from literature can be used to model bubble dynamics in porous media. The experimental data and findings of Takemura *et al.* (2002) suggest that an overall effect of frictional forces results in pore-scale velocity vectors shifted by an angle θ with respect to the direction of mean flow. A quick calculation indicates that a bubble has travelled a net vertical distance $D \cos \theta$ in a porous medium during a period when it has travelled an actual average distance of about D . As a result, the terminal speed of the bubble in porous media has an equivalent impact with respect to that in clear media. This phenomena may be characterized from controlled numerical simulations. Let us now present a comparison of the terminal speed of a bubble rising in a porous medium with that in a clear medium.

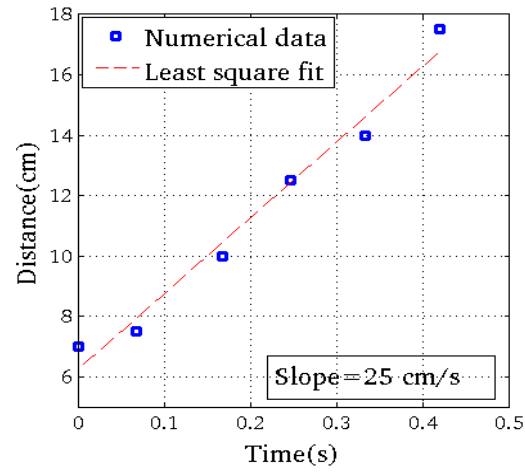
Fig 6.8 compares the time-distance plot for two numerical simulations. Fig 6.8(a) presents the result, where a rising bubble in a fluid of higher density has been simulated. The terminal velocity has been estimated 25 cm/s. Fig 6.8(b) presents the result under the same conditions as that is in Fig 6.8(a), except now the bubble rises in a fluid saturated porous medium. The terminal velocity is estimated 17.5 cm/s in this case. For this simulation, the ratio of the net distance travelled to the actual vertical distance is approximately

$\cos 45^\circ$. In other words, the local velocity vectors of fluid particles with the bubble has an overall shift of 45° with respect to the vertical direction when bubble rises in porous media. It is worth mentioning that the several other investigators measured the apparent dispersion coefficient in a porous medium and found that the effect of the porous medium on the dispersion coefficient is equivalent to the local velocity vectors shifted by $\theta \approx 45^\circ$.

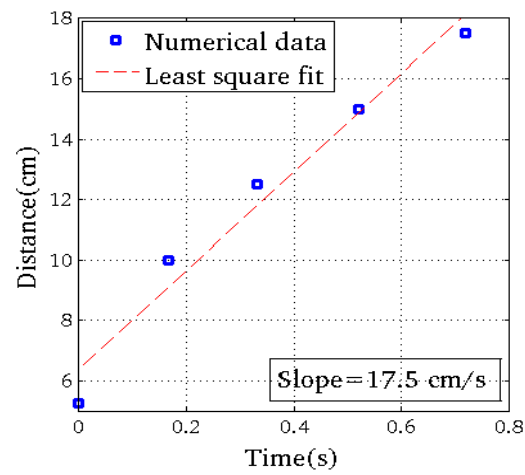
Roosevelt & Corapcioglu (1998) and Corapcioglu *et al.* (2004) reported experimental studies that are dynamically equivalent to the case discussed in the present work. We have considered such experimental data along with two sets of data obtained from the numerical simulations with our phase-field method. One of the simulations is carried out in a clear medium, and the other is done with a porous medium. In each case, the size of initial bubble is the only parameter that has been varied. The result is presented in Fig 6.9, showing a comparison among the experimental data, numerical simulation, and analytical results. In both cases, the numerical simulation has a good agreement with the analytical solution for the entire range of bubble sizes. We see that the experimental data show a trend of deviation for bubbles of radius < 0.3 cm, which indicates that the measurement error may have dominated for small bubble. Note also that the slight discrepancy between the numerical data and the analytical solution for small bubbles could have been improved by increasing numerical resolution.

6.4.4 Mass conservation in a phase-field simulation

In a two-phase flow simulation with Allen-Cahn phase-field method, we assume that no mass transfer occurs from one phase to another although we do not calculate the saturation of each phases individually. Mass conservation is important in such modelling approach because the simulations would preserve the immiscibility despite there is a diffuse interface between two phases. In view of petroleum engineering, a phase-field simulation that does



(a)



(b)

Figure 6.8: Time vs distance plot for a rising bubble. (a) A test of a rising bubble in a fluid. The data fit well with an average speed 25 cm/s. (b) A test of a rising bubble in a fluid saturated porous medium. The data fit well with an average speed 17.5 cm/s.

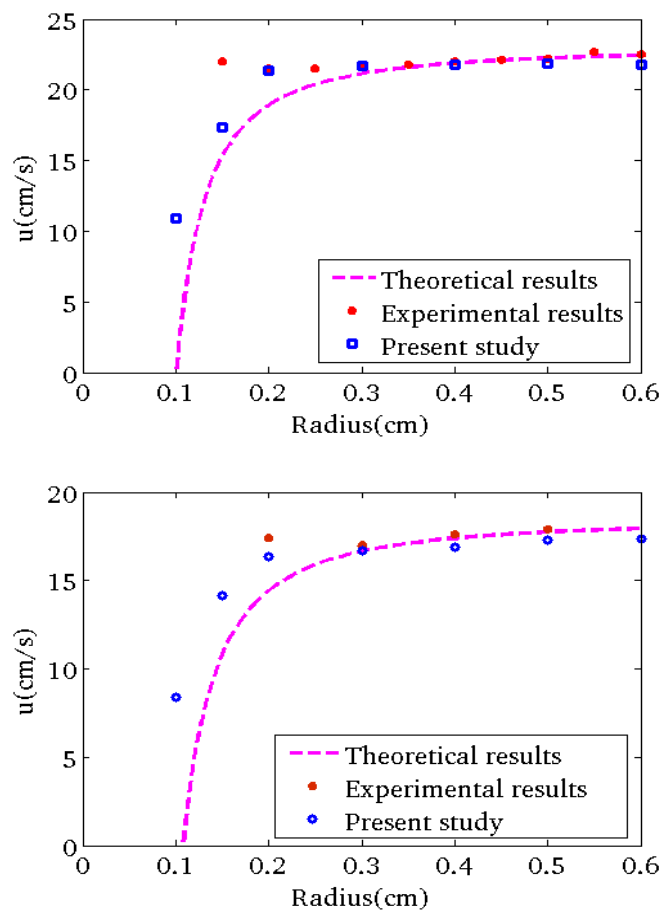


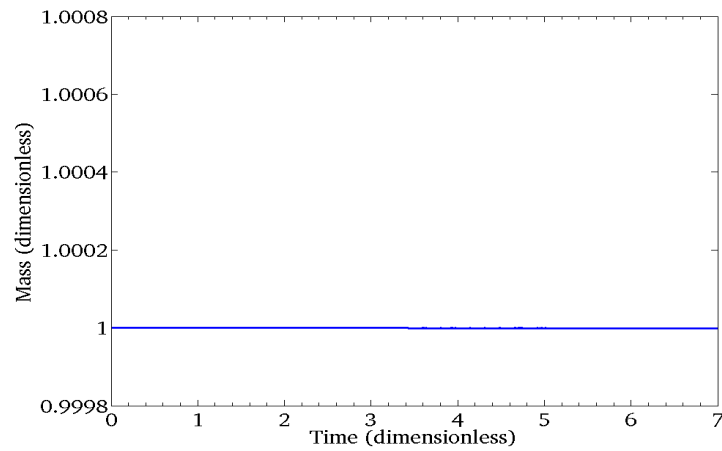
Figure 6.9: The terminal bubble velocity of a rising bubble as a function of the initial radius of the bubble. The present numerical study is compared with respect to the theoretical terminal velocity v_T and experimental data from Roosevelt & Corapcioglu (1998). (a) clear fluid, and (b) fluid saturated porous medium.

not conserve mass would predict the overall rate of oil production inaccurately. Since the bubble may deform from its initial spherical shape during a period of travel, depending on the underlying physical condition, immiscibility implies that the mass of individual phase would still conserve..

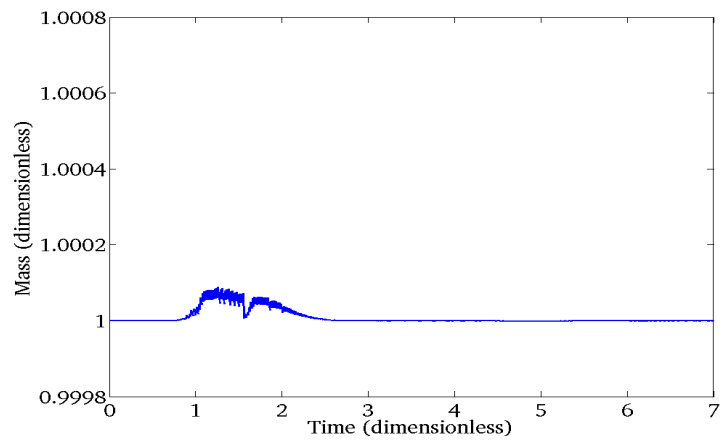
In a phase-field model, one thus expects that the quantity $\langle C(\mathbf{x}, t) \rangle = \int_{\Omega} C(\mathbf{x}, t) d\Omega$ remains approximately constant for the entire period of simulation. The conservation of mass can be examined by analyzing the time series, $\langle C(\mathbf{x}, t) \rangle / \langle C(\mathbf{x}, 0) \rangle$. In Fig 6.2 and 6.7, we notice that the bubble has been deformed during its travel. We have presented the time series $\langle C(\mathbf{x}, t) \rangle / \langle C(\mathbf{x}, 0) \rangle$ in Fig: 6.10(a, b). The plot in Fig:6.10(a) shows that the total mass is conserved with a sufficient accuracy in case of a liquid saturated medium - as expected. In case of the liquid saturated porous medium, the plot in Fig:6.10(b) shows a relative numerical error that is $\mathcal{O}(10^{-4})$. It is evident from this result that the proposed CFD simulation is highly accurate in terms of numerical truncation error.

6.5 Conclusion and future work

In the study of multiphase flow, the dynamics of the interface between two fluids can be described according to the classical Gibbs theory of capillarity, where fluid properties vary discontinuously across a sharp interface of zero thickness (Xu & Meakin, 2008; Antanovskii, 1995). The classical Buckley-Leverett approach is a sharp-interface method for multiphase flow in porous media based on the Darcy's equation, where capillary phenomena are lumped into the relative permeability. In contrast, the phase-field theory of capillarity is based on the thermodynamic principle of equilibrium, where fluid properties vary continuously across an interface of finite thickness, which contains excess free-energy of the system (Jacqmin, 1999). Literatures indicate that there is a growing interest on phase-field modelling of multiphase flow; however, there is a lack of studies on how to extend the



(a)



(b)

Figure 6.10: The time series representing the normalized mass of the gas phase. Clearly the total mass is conserved with sufficient accuracy. (a) The time series associated to the results in Fig: 6.2 (clear medium); (b) the time series associated to the results in Fig: 6.7(b) in the porous media with the Darcy number, $Da = 9 \times 10^{-4}$. Note the terminal bubble shapes are very close for the selected results.

phase-field method for a CFD simulation of multiphase flow in porous media.

In this article, we have introduced a wavelet-based phase-field method for the CFD simulation of multiphase flow in homogeneous porous media, and have analyzed the bubble dynamics to understand how the excess free-energy of the system is related to capillary phenomena. The following findings are useful to extend the proposed multiphase flow modelling approach.

- The phase-field method based on the van der Waals free-energy theory describes the capillary phenomena adequately in case of a gas bubble rising in water.
- In a macroscale CFD simulation, where the mesh does not resolve the porous media at the pore scale, the capillary stress tensor can be expressed as a tensor of the gradients of phase-field variable. In comparison to experiment, this construction of capillary stress is felt adequate in the present study.
- A comparison between the CFD simulation and the experimental data has been used to demonstrate that the phase-field method obtains the terminal shape and velocity of bubbles accurately. This indicates that the topological shapes of the bubbles can be described by the excess free-energy of the system. In other words, phase-field method predicts the bubble coalescence and break up accurately.

A study on the mesh independent simulation and time series analysis indicates that the transient simulations help to understand the time history of a two-phase flow, where the proposed CFD method does not suffer from any visible artificial numerical damping. Authors note that the accuracy and efficiency of their wavelet-based CFD code are due to the rigorous mathematical foundation of the wavelet method and the phase-field method, and the implementation of this code has taken advantage of two well-known software libraries, `libMesh` (Kirk *et al.*, 2006) and `PETSc` (Balay *et al.*, 1997). The present implementation

of the multi-resolution wavelet method has taken advantage of the object oriented C++ environment provided by the `libMesh` library. Similarly, the parallel implementation of the multiphysics wavelet solver has interfaced the `SNES` solver of the `PETSc` library.

The CFD method presented in this work has investigated the bubble shapes for a range of values of the non-dimensional parameters, such as the Reynolds number, the Bond number, and the Darcy number. A spherical shape of the bubble indicates that the pressure falls along the vertical direction, $dp/dz < 0$, and we say that the pressure drop is “favorable”. On the other hand, the skirted shape of the bubble indicates that the pressure rises along the vertical direction, $dp/dz > 0$, and we say that the pressure drop is “adverse” or “unfavorable”. This means that the present wavelet-based phase-field approach of multiphase flow simulation characterizes the overall flow rate or pressure drop when bubbles are driven by the buoyancy force. Further investigation is necessary to fully understand how bubbles break up or coalesce in porous media as they migrate with the continuous phase. Notably, this article does not have enough scope of discussing bubbly flow in heterogeneous or fractured porous media, which may be addressed in a future study.

Finally, authors note that the present research can be extended to investigate the deliverable from various drilling techniques, to directly simulate experimental procedures for similar purposes, and to simulate flow and transport in the field scale wellbores and reservoirs. Such work is currently underway.

Acknowledgements

J. Alam acknowledges financial support from the National Science and Research Council (NSERC), Canada. M. A. Rahman acknowledges financial support from the National Science and Research Council-discovery grant(NSERC-DG), Canada, RDC Ignite, NL and Seed grant Memorial University of Newfoundland, Canada. S. D. Butt acknowledges fi-

nancial support from the National Science and Research Council (NSERC), Canada. M. J. Ahammad acknowledges School of graduate studies, Memorial University of Newfoundland, Canada for scholarships.

Nomenclature

Symbol	Units	Description
x	m	Horizontal coordinate
z	m	Vertical coordinate
t	s	Time
\mathbf{u}	ms^{-1}	Velocity field
P	Pa	Pressure
g	ms^{-2}	Acceleration due to gravity
\mathcal{K}	m^2	Permeability of the medium
ϕ	--	Porosity of the medium
c_t	--	Gas compressibility
C	m^3	Volume fraction of fluid
I	--	Identity matrix
d	m	Characteristic of pore space
μ_g	mPa.S	Gas viscosity
μ_l	mPa.S	Liquid viscosity
ν	m^2/s	Kinematic viscosity
ρ_g	Kg/m^3	Gas density
ρ_l	Kg/m^3	Liquid density
ρ	Kg/m^3	Density
P_l	Pa	Liquid pressure

P_g	Pa	Gas pressure
σ	Nm^{-1}	Surface tension
τ_σ	Nm^{-1}	Stress due to surface tension
ϵ	m	Interface thickness
κ	1/m	Curvature of the interface
\mathcal{W}	Nm^{-1}	Total free energy
μ^c	J/mole = Newton	Chemical potential
$1/\mathcal{T}$	1/s	Inverse elastic relaxation time-scale
$\Delta x, \Delta y, \Delta z$		Grid space along x, y, z -axis
ΔV		Grid volume
Δt		Time step
\mathcal{O}		Order of magnitude
μm		Micrometer
\mathcal{N}		Number of grid points
Non-dimensional parameters		
Re		Reynolds number
Da		Darcy number
Bo		Bond number
U		Velocity scale
D		Length scale
Subscript		
g		Gas
i		$i = 1, 2$ phase
l		Liquid
Abbreviation		

CFD	Computational Fluid Dynamics
CPU	Central Processing Unit
VOF	Volume Of Fluid
EOR	Enhanced Oil Recovery

Chapter 7

Conclusion and future research direction

The aim of the research project in this thesis is to study multiphase flow around near the wellbore of a reservoir using the 3D Navier-Stokes Equations. We use an experimental and a CFD approach to understand the problem. In this regard, a new radial flow experimental prototype is developed and validated with two types of samples (Chapter 2). The primary experimental investigations are performed with these samples and the results indicate that the apparatus is capable of simulating near-wellbore flow phenomena. The experimental results can be verified with the theoretical results for different flow and formation conditions such as μ , ϕ , \mathcal{K} and q . More experiments can be performed to explore the wide range of applications with this setup but were not done for now due to the timeline constraint. In general, the experiments are not free from limitations. The main constraints of the experiment setup include the boundary conditions (*i.e* positioning of the measurement tools on the right place of the physical domain of the problem). Despite these limitations, more oil/gas reservoir engineering problems can be conducted in future with this experimental setup as mentioned in the (Chapter 2). More validation tests can be performed to understand the coupled dynamics of wellbore-reservoir fluid flow. In addition to this, the characteristics of the various formation zones and formation damage due to different perforation techniques

with multiphase flow mechanism, formation damage in the near-wellbore environment due to the drilling process and the field trial of the innovated new drilling fluid can be pursued with this setup.

In chapter 3, a CFD approach is employed to model of fluid flows phenomena around the near wellbore of a reservoir using the 3D Navier-Stokes equations. A coupled solver is used to get a robust, accurate numerical solution of NSE for the reservoir fluid flows. The model is verified with the analytical solution of a simplified model and successfully applied to study flow at the near wellbore of a reservoir for different flow scenarios. The results indicate that the model can be extended for wellbore-skin-reservoir coupling model with different skin zones. The research towards this point has been conducted in chapter 4. In future, the different layers of a reservoir can be included in the new model. Furthermore, the model can be extended for a horizontal well with formation damage and other features such as mitigation can be included in the model.

The model described in chapter 3 is extended as a coupled wellbore-reservoir model in chapter 4. The numerical simulations are performed with efficient CFD methodology for the reservoir fluid flows. The model is verified and investigated flow performance of an idealized reservoir. In the future, this model can be extended for the realistic reservoir conditions and can be more verified with field data. Moreover, it can be easily extended for two-phase flow study with appropriate interface conditions. In addition, turbulence flow through wellbore can be modelled with this CFD methodology.

In the next chapter 5, the Navier-Stokes equations are applied to investigate reservoir fluid flow through a perforation tunnel. The results indicate that the pressure buildup in the porous medium is greatly affected by gas flow rate and formation permeability. In addition, the breakthrough of pressure build-up for the flow in a core sample is the gas flow rate and gas flow in a porous system reduces hydrostatic pressure loss. The research in this chapter suggests the future study of the dynamics of the interface between two fluids for the flow

through porous media with an appropriate model.

In the final chapter 6, a phase-field technique is applied to model the interface between two fluids in the study of multiphase flow in homogeneous porous media. Classically, the interface between two fluids is explained with Gibbs theory of capillarity considering a discontinuous sharp interface of zero thickness (Xu & Meakin, 2008; Antanovskii, 1995). Here, a wavelet-based phase-field methodology with a continuous interface of finite thickness is introduced, which contains excess free-energy of the system (Jacqmin, 1999). In this investigation, it is remarkable that the capillary stress tensor can be expressed as a tensor of the gradients of the phase-field variable. Moreover, the topological shapes of the bubbles for two-phase flow can be explained by the excess free-energy of the system, *i.e.* phase-field method can predict the bubble coalescence and break up accurately. The wavelet-based CFD methodology used here with the accuracy and efficiency due to the rigorous mathematical foundation of the wavelet method and the phase-field method. The present implementation of the multi-resolution wavelet method has taken advantage of two well-known software libraries, `libMesh` (Kirk *et al.*, 2006) and `PETSc` (Balay *et al.*, 1997). In the future, the wavelet-based phase-field methodology can be applied to discuss the bubbly flow in heterogeneous or fractured porous media. In addition, this CFD methodology can be applied to directly simulate experimental procedures for similar purposes and to simulate flow in the field scale wellbores and reservoirs.

Bibliography

ABBASI, R., ASHRAFIZADEH, A. & SHADARAM, A. 2013 A comparative study of finite volume pressure-correction projection methods on co-located grid arrangements. *Computers & Fluids* **81**, 68–84.

AFSHARPOOR, A., BALHOFF, M. T., BONNECAZE, R. & HUH, C. 2012 Cfd modeling of the effect of polymer elasticity on residual oil saturation at the pore-scale. *Journal of Petroleum Science and Engineering* **94-95**, 79–88.

AHAMMAD, M. J. & ALAM, J. M. 2017 A numerical study of two-phase miscible flow through porous media with a lagrangian model. *The Journal of Computational Multi-phase Flows* p. 1757482X17701791.

AHAMMAD, M. J., ALAM, J. M., RAHMAN, M. & BUTT, S. D. 2017 Numerical simulation of two-phase flow in porous media using a wavelet based phase-field method. *Chemical Engineering Science* **173**, 230–241.

AHAMMAD, M. J., RAHMAN, M. A., ALAM, J. M. & BUTT, S. D. submitted-2018 A cfd investigation of the flow behavior near a wellbore using navier-stokes equation. *Journal of Advances Mechanical Engineering* .

- AHAMMAD, M. J., RAHMAN, M. A., BUTT, S. D. & ALAM, J. M. 2018a A coupled wellbore-reservoir model based on 3d navier-stokes equations with ‘skin zone’ around wellbore. *Journal of Petroleum Science and Engineering* **submitted**, xx.
- AHAMMAD, M. J., RAHMAN, M. A., ZHENG, L., ALAM, J. M. & BUTT, S. D. 2018b Numerical investigation of two-phase fluid flow in a perforation tunnel. *Journal of Natural Gas Science and Engineering* **55**, 606–611.
- ALAM, J., WALSH, R., HOSSAIN, M. A. & ROSE, A. 2014 A computational methodology for two-dimensional fluid flows. *Int. J. Numer. Meth. Fluids* **75(12)**, 835–859.
- ALAM, J. M. 2015 A multiscale modeling study for the convective mass transfer in a subsurface aquifer. *Heat and Mass Transfer* **51** (9), 1247–1261.
- ALAM, J. M., KEVLAHAN, N. K.-R., VASILYEV, O. & HOSSAIN, Z. 2012 A multiresolution model for the simulation of transient heat and mass transfer. *Numerical Heat Transfer* **61(B)**, 1–24.
- ALPAK, F. O., RIVIERE, B. & FRANK, F. 2016 A phase-field method for the direct simulation of two-phase flows in pore-scale media using a non-equilibrium wetting boundary condition. *Computational Geosciences* pp. 1–28.
- ANOVITZ, L. M. & COLE, D. R. 2015 Characterization and analysis of porosity and pore structures. *Reviews in Mineralogy and geochemistry* **80** (1), 61–164.
- ANSYS, R. 2016 Release 16.2, ansys cfx-solver theory guide, ansys.
- ANTANOVSKII, L. K. 1995 A phase field model of capillarity. *Physics of Fluids* **7** (4), 747–753.

- ARZANFUDI, M. M., SAEID, S., AL-KHOURY, R. & SLUYS, L. 2016 Multidomain-staggered coupling technique for darcy–navier stokes multiphase flow: An application to co₂ geosequestration. *Finite Elements in Analysis and Design* **121**, 52–63.
- ASTM-D5084 2010 Standard test methods for measurement of hydraulic conductivity of saturated porous materials using a flexible wall permeameter. *ASTM International* pp. 1–24.
- AZADI, M., AMINOSSADATI, S. M. & CHEN, Z. 2017 Development of an integrated reservoir-wellbore model to examine the hydrodynamic behaviour of perforated pipes. *Journal of Petroleum Science and Engineering* **156**, 269–281.
- AZIN, R., MOHAMADI-BAGHMOLAEI, M. & SAKHAEI, Z. 2017 Parametric analysis of diffusivity equation in oil reservoirs. *Journal of Petroleum Exploration and Production Technology* **7** (1), 169–179.
- BALAY, S., GROPP, W. D., MCINNES, L. C. & SMITH, B. F. 1997 Efficient management of parallelism in object-oriented numerical software libraries. In *Modern software tools for scientific computing*, pp. 163–202. Springer.
- BARLA, G., BARLA, M. & DEBERNARDI, D. 2010 New triaxial apparatus for rocks. *Rock mechanics and rock engineering* **43** (2), 225–230.
- BARTH, T. & JESPERSEN, D. 1989 The design and application of upwind schemes on unstructured meshes. In *27th Aerospace sciences meeting*, p. 366.
- BEAR, J. 1972 *Dynamic of fluids in porous media*, 1st edn. American Elsevier publishing company.
- BEHRMANN, L., HUGHES, K., JOHNSON, A., WALTON, I. *et al.* 2002 New underbalanced perforating technique increases completion efficiency and eliminates costly acid

- stimulation. In *SPE Annual Technical Conference and Exhibition*. Society of Petroleum Engineers.
- BELL, M. & CLARK, N. 2009 Reactive perforating—putting the exclamation point on a great well. In *American Association of Drilling Engineers 2009 National Technical Conference & Exhibition, New Orleans, Louisiana*.
- BHAGA, D. & WEBER, M. E. 1981 Bubbles in viscous liquids : shapes, wakes and velocities. *J. Fluid Mech.* , wol. 105, p p . 61-85 **105**, 61–85.
- BRANETS, L. V., GHAI, S. S., LYONS, S. L. & WU, X.-H. 2009 Challenges and technologies in reservoir modeling. *Communications in Computational Physics* **6** (1), 1.
- BREUGEM, W. P. & REES, D. A. S. 2006 A Derivation of the Volume-Averaged Boussinesq Equations for Flow in Porous Media with Viscous Dissipation. *Transport in Porous Media* **63** (1), 1–12.
- BUTT, S. 1999 Development of an apparatus to study the gas permeability and acoustic emission characteristics of an outburst-prone sandstone as a function of stress. *International Journal of Rock Mechanics and Mining Sciences* **8** (36), 1079–1085.
- BUTT, S. D., FREMPONG, P. K., MUKHERJEE, C. & UPSHALL, J. 2005 Characterization of the permeability and acoustic properties of an outburst-prone sandstone. *Journal of applied geophysics* **58** (1), 1–12.
- BYRNE, M., DJAYAPERTAPA, L., WATSON, K., GOODIN, B. *et al.* 2014 Complex completion design and inflow prediction enabled by detailed numerical well modeling. In *SPE International Symposium and Exhibition on Formation Damage Control*. Society of Petroleum Engineers.

- BYRNE, M. T., JIMENEZ, M. A., CHAVEZ, J. C. *et al.* 2009 Predicting well inflow using computational fluid dynamics-closer to the truth? In *8th European Formation Damage Conference*. Society of Petroleum Engineers.
- BYRNE, M. T., JIMENEZ, M. A., ROJAS, E. A. & CHAVEZ, J. C. 2010 Modeling well inflow potential in three dimensions using computational fluid dynamics. In *SPE International Symposium and Exhibition on Formation Damage Control*. Society of Petroleum Engineers.
- CAI, X., MARSCHALL, H., WÖRNER, M. & DEUTSCHMANN, O. 2015 Numerical simulation of wetting phenomena with a phase-field method using openfoam. *Chemical Engineering & Technology* **38** (11), 1985–1992.
- CHAUDHRY, A. 2004 *Oil well testing handbook*. Elsevier.
- CHEN, T., CHIU, M.-S. & WENG, C.-N. 2006a Derivation of the generalized Young-Laplace equation of curved interfaces in nanoscaled solids. *Journal of Applied Physics* **100** (7), 074308–1–10.
- CHEN, Z., HUAN, G. & LI, B. 2004 An improved impes method for two-phase flow in porous media. *Transport in porous media* **54** (3), 361–376.
- CHEN, Z., HUAN, G. & MA, Y. 2006b *Computational methods for multiphase flows in porous media*. SIAM.
- CHEN, Z., HUAN, G. & MA, Y. 2006c *Computational methods for multiphase flows in porous media*. SIAM.
- CHUPIN, G., HU, B., HAUGSET, T., SAGEN, J., CLAUDEL, M. *et al.* 2007 Integrated wellbore/reservoir model predicts flow transients in liquid-loaded gas wells. In *SPE Annual Technical Conference and Exhibition*. Society of Petroleum Engineers.

- CIVAN, F. 2015 *Reservoir formation damage*. Gulf Professional Publishing.
- CORAPCIOGLU, M. Y., CIHAN, A. & DRAZENOVIC, M. 2004 Rise velocity of an air bubble in porous media: Theoretical studies. *Water Resources Research* **40**, 1–9.
- D4543, A. S. 1985 Standard practice for preparing rock core specimens and determining dimensional and shape tolerances. *American Society for the Testing of Materials* .
- DAIGLE, H., RASROMANI, E. & GRAY, K. 2017 Near-wellbore permeability alteration in depleted, anisotropic reservoirs. *Journal of Petroleum Science and Engineering* **157**, 302–311.
- DAKE, L. P. 1983 *Fundamentals of reservoir engineering*, , vol. 8. Elsevier.
- DAKE, L. P. 1994 The practice of reservoir engineering. *Developments in petroleum science* **36**, 311–458.
- DAKE, L. P. 2001 *The practice of reservoir engineering (revised edition)*, , vol. 36. Elsevier.
- DELEMONS, M. J. S. 2006 *Turbulence in Porous Media modeling and applications*, 1st edn. ELSEVIER.
- DING, D. 2011 Coupled simulation of near-wellbore and reservoir models. *Journal of Petroleum Science and Engineering* **76** (1-2), 21–36.
- DING, Y. *et al.* 1999 Transient pressure solution in the presence of pressure drop in the wellbore. In *SPE Annual Technical Conference and Exhibition*. Society of Petroleum Engineers.
- DULLIEN, F. A. 2012 *Porous media: fluid transport and pore structure*. Academic press.

- ECONOMIDES, M. J. 2013 *Petroleum production systems*. Pearson Education.
- ELSAIED, S. A., BAKER, R., CHURCHER, P. L. & EDMUNDS, A. C. 1993 Multidisciplinary reservoir characterization and simulation study of the weyburn unit. *Journal of Petroleum Technology* **45(10)**, 930–934,973.
- ERGUN, S. 1952 Fluid flow through packed columns. *Chem. Eng. Prog.* **48**, 89–94.
- FENG, X. 2006 Fully discrete finite element approximations of the navier–stokes–cahn–hilliard diffuse interface model for two-phase fluid flows. *SIAM Journal on Numerical Analysis* **44** (3), 1049–1072.
- FENG, X., HE, Y. & LIU, C. 2007 Analysis of finite element approximations of a phase field model for two-phase fluids. *Mathematics of Computation* **76(258)**, 539–571.
- FINLAYSON, B. A. 2013 *The method of weighted residuals and variational principles*, 3rd edn. SIAM.
- FIROOZABADI, A. & KATZ, D. L. 1979 An analysis of high-velocity gas flow through porous media. *Journal of Petroleum Technology* **31** (02), 211–216.
- GILLIAT, J., SNIDER, P. M. & HANEY, R. 1999 A review of field performance of new propellant/perforating technologies. In *SPE annual technical conference*, pp. 97–106.
- GIORGIO, B., INZOLI, F., ZIEGENHEIN, T. & LUCAS, D. 2017 Computational fluid-dynamic modeling of the pseudo-homogeneous flow regime in large-scale bubble columns. *Chemical Engineering Science* **160**, 144–160.
- GUPPY, K., CINCO-LEY, H., RAMEY JR, H. J. *et al.* 1981 Effect of non-Darcy flow on the constant-pressure production of fractured wells. *Society of Petroleum Engineers Journal* **21** (03), 390–400.

- HAGOORT, J. 2007 An analytical model for predicting the productivity of perforated wells. *Journal of Petroleum Science and Engineering* **56** (4), 199–218.
- HASLE, G., LIE, K.-A. & QUAK, E. 2007 *Geometric Modelling, Numerical Simulation, and Optimization: Applied Mathematics at SINTEF*. Springer.
- HAWKINS JR, M. F. *et al.* 1956 A note on the skin effect. *Journal of Petroleum Technology* **8** (12), 65–66.
- HELMIG, R., FLEMISCH, B., WOLFF, M., EBIGBO, A. & CLASS, H. 2013 Model coupling for multiphase flow in porous media. *Advances in Water Resources* **51**, 52–66.
- HIGDON, J. 2013 Multiphase flow in porous media. *Journal of Fluid Mechanics* **730**, 1–4.
- HILLEL, D. 1998 *Environmental soil physics: Fundamentals, applications, and environmental considerations*. Elsevier.
- HIRT, C. & NICHOLS, B. 1981 Volume of fluid (VOF) method for the dynamics of free boundaries. *Journal of Computational Physics* **39** (1), 201 – 225.
- HOLDITCH, S., MORSE, R. *et al.* 1976 The effects of non-darcy flow on the behavior of hydraulically fractured gas wells (includes associated paper 6417). *Journal of Petroleum Technology* **28** (10), 1–169.
- HOLT, R., BRIGNOLI, M. & KENTER, C. 2000 Core quality: quantification of coring-induced rock alteration. *International Journal of Rock Mechanics and Mining Sciences* **37** (6), 889–907.
- HORGUE, P., SOULAINÉ, C., FRANC, J., GUIBERT, R. & DEBENEST, G. 2015a An open-source toolbox for multiphase flow in porous media. *Computer Physics Communications* **187**, 217–226.

- HORGUE, P., SOULAINÉ, C., FRANC, J., GUIBERT, R. & DEBENEST, G. 2015b An open-source toolbox for multiphase flow in porous media. *Computer Physics Communications* **187**, 217–226.
- HUA, J. & LOU, J. 2007 Numerical simulation of bubble rising in viscous liquid. *Journal of Computational Physics* **222**, 769–795.
- HUANG, G., SONG, H., CAO, Y., YANG, J., WANG, Y., KILLOUGH, J. & CAI, S. 2016 Numerical investigation of low-velocity non-darcy flow of gas and water in coal seams. *Journal of Natural Gas Science and Engineering* **34**, 124–138.
- ISLAM, M. R., MOUSSAVIZADEGAN, S. H., MUSTAFIZ, S. & ABOU-KASSEM, J. H. 2010 *Advanced petroleum reservoir simulation*. Scrivener, Wiley.
- JACQMIN, D. 1999 Calculation of two-phase navier–stokes flows using phase-field modeling. *Journal of Computational Physics* **155** (1), 96–127.
- JAMESON, L. 1993 On the wavelet based differentiation matrix. *Journal of Scientific Computing* **8** (3), 267–305.
- JIN, Y., CHEN, K. P. & CHEN, M. 2012 Highly compressible porous media flow near a wellbore: effect of gas acceleration. *Journal of Fluids Engineering* **134** (1), 011301.
- KHADIVI, K. & SOLTANIEH, M. 2014a Numerical solution of the nonlinear diffusivity equation in heterogeneous reservoirs with wellbore phase redistribution. *Journal of Petroleum Science and Engineering* **114**, 82–90.
- KHADIVI, K. & SOLTANIEH, M. 2014b Numerical solution of the nonlinear diffusivity equation in heterogeneous reservoirs with wellbore phase redistribution. *Journal of Petroleum Science and Engineering* **114**, 82–90.

- KHADIVI, K., SOLTANIEH, M. & FARHADPOUR, F. A. 2013 A coupled wellbore- reservoir flow model for numerical pressure transient analysis in vertically heterogeneous reservoirs. *Journal of Porous Media* **16** (5).
- KHANIAMINJAN, A. & GOUDARZI, A. 2008 Non-darcy fluid flow through porous media. *SPE* **114019**, 1–19.
- KIM, J. 2012 Phase-field models for multi-component fluid flows. *Commun. Comput. Phys* **12** (3), 613–661.
- KIRK, B., PETERSON, S. & STOGNER, J. AND CAREY, W. 2006 LibMesh : A C++ library for parallel adaptive mesh refinement/coarsening simulations. *Engineering with Computers* **22(3)**, 237–254.
- KUNDU, P., KUMAR, V. & MISHRA, I. M. 2016 Experimental and numerical investigation of fluid flow hydrodynamics in porous media: Characterization of pre-darcy, darcy and non-darcy flow regimes. *Powder Technology* **303**, 278–291.
- KUNDU, P. K., COHEN, I. M. & DOWLING, D. R. 2012 *Fluid Mechanics*, 5th edn. ELSEVIER.
- KUSUMAATMAJA, H., HEMINGWAY, E. J. & FIELDING, S. M. 2016 Moving contact line dynamics: from diffuse to sharp interfaces. *Journal of Fluid Mechanics* **788**, 209–227.
- LANDMAN, M., GOLDTHORPE, W. *et al.* 1991 Optimization of perforation distribution for horizontal wells. In *SPE Asia-Pacific conference*. Society of Petroleum Engineers.
- LARSSON, J., IACCARINO, G. *et al.* 2010 A co-located incompressible navier-stokes solver with exact mass, momentum and kinetic energy conservation in the inviscid limit. *Journal of Computational Physics* **229** (12), 4425–4430.

- LEE, R., LOGAN, R., TEK, M. *et al.* 1987 Effect of turbulence on transient flow of real gas through porous media. *SPE Formation Evaluation* **2** (01), 108–120.
- LI, D., SVEC, R. K., ENGLER, T. W., GRIGG, R. B. *et al.* 2001 Modeling and simulation of the wafer non-darcy flow experiments. In *SPE Western Regional Meeting*. Society of Petroleum Engineers.
- LIANDRAT, J. & TCHAMITCHIAN, P. 1990 Resolution of the 1d regularized burgers equation using a spatial wavelet approximation. *Tech. Rep.* NASA Contractor Report 187480. NASA Langley Research Center, Hampton VA.
- LIU, P., LI, W., XIA, J., JIAO, Y. & BIE, A. 2016 Derivation and application of mathematical model for well test analysis with variable skin factor in hydrocarbon reservoirs. *AIP Advances* **6** (6), 065324.
- LIVESCU, S., DURLOFSKY, L., AZIZ, K. & GINESTRA, J. 2010 A fully-coupled thermal multiphase wellbore flow model for use in reservoir simulation. *Journal of Petroleum Science and Engineering* **71** (3), 138–146.
- MAHDIYAR, H., JAMIOLAHMADY, M. & SOHRABI, M. 2011 Improved Darcy and non-Darcy flow formulations around hydraulically fractured wells. *Journal of Petroleum Science and Engineering* **78** (1), 149–159.
- MALLAT, S. 2009 *A wavelet tour of signal processing*. Academic press.
- MCKEE, C. R., BUMB, A. C., KOENIG, R. A. *et al.* 1988 Stress-dependent permeability and porosity of coal and other geologic formations. *SPE formation evaluation* **3** (01), 81–91.

- MEHRA, M. & KUMAR, B. V. R. 2005 Time-accurate solution of advection-diffusion problems by wavelet-taylor-galerkin method. *Communications in Numerical Methods in Engineering* **21** (6), 313–326.
- MILLER, C. T., CHRISTAKOS, G., IMHOFF, P. T., MCBRIDE, J. F., PEDIT, J. A. & TRANGENSTEIN, J. A. 1998 Multiphase flow and transport modeling in heterogeneous porous media: challenges and approaches. *Advances in Water Resources* **21** (2), 77–120.
- MOLINA, O. & TYAGI, M. 2015 A computational fluid dynamics approach to predict pressure drop and flow behavior in the near wellbore region of a frac-packed gas well. In *ASME 2015 34th International Conference on Ocean, Offshore and Arctic Engineering*, pp. V010T11A023–V010T11A023. American Society of Mechanical Engineers.
- NARSILIO, G. A., BUZZI, O., FITYUS, S., YUN, T. S. & SMITH, D. W. 2009 Upscaling of navier–stokes equations in porous media: Theoretical, numerical and experimental approach. *Computers and Geotechnics* **36** (7), 1200–1206.
- NIND, J. 1989 *Hydrocarbon reservoir and well performance*. Springer Science & Business Media.
- OLBRICHT, W. 1996 Pore-scale prototypes of multiphase flow in porous media. *Annual review of fluid mechanics* **28** (1), 187–213.
- PEACEMAN, D. W. & RACHFORD, J. 1962 Numerical calculation of multidimensional miscible displacement. *SPE Journal* **2**(4), 327–339.
- PERERA, M., RANJITH, P., CHOI, S. & AIREY, D. 2011 Numerical simulation of gas flow through porous sandstone and its experimental validation. *Fuel* **90** (2), 547–554.
- PLETCHER, R. H., TANNEHILL, J. C. & ANDERSON, D. 2012 *Computational fluid mechanics and heat transfer*. CRC Press.

- PLETCHER, R. H., TANNEHILL, J. C. & ANDERSON, D. A. 2013 *Computational Fluid Mechanics and Heat transfer*, 3rd edn. Taylor & Francis group.
- POPOV, P., EFENDIEV, Y. & QIN, G. 2009 Multiscale modeling and simulations of flows in naturally fractured karst reservoirs. *Communications in computational physics* **6**(1), 162–184.
- PROVATAS, N. & ELDER, K. 2011 *Phase-field methods in materials science and engineering*, 1st edn. John Wiley & Sons.
- PRUESS, K. & ZHANG, K. 2008 Numerical modeling studies of the dissolution - diffusion - convection process during CO₂ storage in saline aquifers. *Lawrence Berkeley National Laboratory, California Technical Report LBNL-1243E*, 1–32.
- RAHMAN, M., ADANE, K. F. & SANDERS, R. S. 2013 An improved method for applying the lockhart-martinelli correlation to three-phase gas-liquid-solid horizontal pipeline flows. *The Canadian Journal of Chemical Engineering* **91** (8), 1372–1382.
- RAHMAN, M., MUSTAFIZ, S., KOKSAL, M. & ISLAM, M. 2007a Quantifying the skin factor for estimating the completion efficiency of perforation tunnels in petroleum wells. *Journal of Petroleum Science and Engineering* **58** (1), 99–110.
- RAHMAN, M. A., MUSTAFIZ, S., BIAZAR, J., KOKSAL, M. & ISLAM, M. 2007b Investigation of a novel perforation technique in petroleum wells-perforation by drilling. *Journal of the Franklin Institute* **344** (5), 777–789.
- RAHMAN, M. A., MUSTAFIZ, S., BIAZAR, J., KOKSAL, M. & ISLAM, M. 2007c Investigation of a novel perforation technique in petroleum wells perforation by drilling. *Journal of the Franklin Institute* **344** (5), 777–789.

- RAMIREZ, W. F. 1987 *Application of optimal control theory to enhanced oil recovery*, , vol. 21. Elsevier.
- RANGEL-GERMAN, E. & SAMANIEGO, F. 2000 On the determination of the skin factor and the turbulence term coefficient through a single constant gas pressure test. *Journal of Petroleum Science and Engineering* **26** (1-4), 121–131.
- RANJITH, P. & PERERA, M. 2011 A new triaxial apparatus to study the mechanical and fluid flow aspects of carbon dioxide sequestration in geological formations. *Fuel* **90** (8), 2751–2759.
- RAZMINIA, K., RAZMINIA, A., KHARRAT, R. & BALEANU, D. 2014 Analysis of diffusivity equation using differential quadrature method. *Rom J Phys* **59** (3-4), 233–246.
- REDONDO, C., RUBIO, G. & VALERO, E. 2018 On the efficiency of the impes method for two phase flow problems in porous media. *Journal of Petroleum Science and Engineering* **164**, 427–436.
- RHIE, C. & CHOW, W. L. 1983 Numerical study of the turbulent flow past an airfoil with trailing edge separation. *AIAA journal* **21** (11), 1525–1532.
- ROOSEVELT, S. E. & CORAPCIOGLU, M. Y. 1998 Air bubble migration in a granular porous medium: Experimental studies. *Water Resources Research* **34**(5), 1131–1142.
- SABOORIAN-JOOYBARI, H. & POURAFSHARY, P. 2015 Significance of non-darcy flow effect in fractured tight reservoirs. *Journal of Natural Gas Science and Engineering* **24**, 132–143.
- SCHNEIDER, K. & VASILYEV, O. V. 2010 Wavelet methods in computational fluid dynamics. *Annu. Rev. Fluid Mech.* **42** (1), 473–503.

- SHEPHERD, J., RIXON, L. & GRIFFITHS, L. 1981 Outbursts and geological structures in coal mines: a review. In *International Journal of Rock Mechanics and Mining Sciences & Geomechanics Abstracts*, , vol. 18, pp. 267–283. Elsevier.
- SHI, H., HOLMES, J. A., DURLOFSKY, L. J., AZIZ, K., DIAZ, L., ALKAYA, B., ODDIE, G. *et al.* 2005 Drift-flux modeling of two-phase flow in wellbores. *Spe Journal* **10** (01), 24–33.
- SKJETNE, E., KLØV, T., GUDMUNDSSON, J. *et al.* 1999 Experiments and modeling of high-velocity pressure loss in sandstone fractures. In *SPE Annual Technical Conference and Exhibition*. Society of Petroleum Engineers.
- SOMERTON, W. H., SÖYLEMEZOĞLU, I. & DUDLEY, R. 1975 Effect of stress on permeability of coal. In *International journal of rock mechanics and mining sciences & geomechanics abstracts*, , vol. 12, pp. 129–145. Elsevier.
- SONG, Z., SONG, H., CAO, Y., KILLOUGH, J., LEUNG, J., HUANG, G. & GAO, S. 2015 Numerical research on co₂ storage efficiency in saline aquifer with low-velocity non-darcy flow. *Journal of Natural Gas Science and Engineering* **23**, 338–345.
- SUN, D., LI, B., GLADKIKH, M., SATTI, R., EVANS, R. *et al.* 2013 Comparison of skin factors for perforated completions calculated with computational-fluid-dynamics software and the karakas-tariq semianalytical model. *SPE Drilling & Completion* **28** (01), 21–33.
- SUN, J., WANG, J. & YANG, Y. 2012 CFD simulation and wavelet transform analysis of vortex and coherent structure in a gas-solid fluidized bed. *Chemical Engineering Science* **71**, 507 – 519.

- SWIFT, G., KIEL, O. *et al.* 1962 The prediction of gas-well performance including the effect of non-darcy flow. *Journal of Petroleum Technology* **14** (07), 791–798.
- SZANYI, M. L., HEMMINGSEN, C. S., YAN, W., WALTHER, J. H. & GLIMBERG, S. L. 2018 Near-wellbore modeling of a horizontal well with computational fluid dynamics. *Journal of Petroleum Science and Engineering* **160**, 119–128.
- TAKEMURA, F., TAKAGI, S., MAGNAUDET, J. & MATSUMOTO, Y. 2002 Drag and lift forces on a bubble rising near a vertical wall in a viscous liquid. *Journal of Fluid Mechanics* **461**, 277–300.
- TANG, H., HASAN, A. R., KILLOUGH, J. *et al.* 2017 A fully-coupled wellbore-reservoir model for transient liquid loading in horizontal gas wells. In *SPE Annual Technical Conference and Exhibition*. Society of Petroleum Engineers.
- TEK, M., COATS, K., KATZ, D. *et al.* 1962 The effect of turbulence on flow of natural gas through porous reservoirs. *Journal of Petroleum Technology* **14** (07), 799–806.
- TERRY, R. E., ROGERS, J. B. & CRAFT, B. C. 2014 *Applied petroleum reservoir engineering*. Pearson Education.
- TU, J., YEOH, G. H. & LIU, C. 2018 *Computational fluid dynamics: a practical approach*. Butterworth-Heinemann.
- VASCONCELOS, D. F. M., ROSSA, A. L. & COUTINHO, A. L. G. A. 2014 A residual-based Allen-Cahn phase field model for the mixture of incompressible fluid flows. *Int. J. Numer. Meth. Fluids* **75**, 645–667.
- VASILYEV, O. V. & BOWMAN, C. 2000 Second-generation wavelet collocation method for the solution of partial differential equations. *J. Comput. Phys.* **165**, 660–693.

- VICENTE, R., SARICA, C., ERTEKIN, T. *et al.* 2000 A numerical model coupling reservoir and horizontal well flow dynamics: Transient behavior of single-phase liquid and gas flow. In *SPE/CIM International Conference on Horizontal Well Technology*. Society of Petroleum Engineers.
- VIETE, D. & RANJITH, P. 2006 The effect of CO₂ on the geomechanical and permeability behaviour of brown coal: implications for coal seam CO₂ sequestration. *International Journal of Coal Geology* **66** (3), 204–216.
- WALSH, R. P. & ALAM, J. M. 2016 Fujiwhara interaction of tropical cyclone scale vortices using a weighted residual collocation method. *International Journal for Numerical Methods in Fluids* **82** (2), 91–110.
- WAN, R. 2011 *Advanced well completion engineering*. Gulf Professional Publishing.
- WANG, F. 2016 Continuous reservoir model calibration with time-dependent reservoir properties diagnosed from long-term down-hole transient pressure data. *Arabian Journal of Geosciences* **9** (4), 1–12.
- WANG, X. & SHENG, J. J. 2017 Effect of low-velocity non-darcy flow on well production performance in shale and tight oil reservoirs. *Fuel* **190**, 41–46.
- WEISBROD, N., MCGINNIS, T., ROCKHOLD, M. L., NIEMET, M. R. & SELKER, J. S. 2009 Effective darcy-scale contact angles in porous media imbibing solutions of various surface tensions. *Water Resources Research* **45** (4).
- WU, D., JU, B. & BRANTSON, E. T. 2016 Investigation of productivity decline in tight gas wells due to formation damage and non-darcy effect: Laboratory, mathematical modeling and application. *Journal of Natural Gas Science and Engineering* **34**, 779–791.

- WU, Y.-S. 2002a Numerical simulation of single-phase and multiphase non-Darcy flow in porous and fractured reservoirs. *Transport in Porous Media* **49** (2), 209–240.
- WU, Y.-S. 2002b Numerical simulation of single-phase and multiphase non-darcy flow in porous and fractured reservoirs. *Transport in Porous Media* **49** (2), 209–240.
- WU, Y.-S., LAI, B., MISKIMINS, J. L., FAKCHAROENPHOL, P. & DI, Y. 2011 Analysis of multiphase non-darcy flow in porous media. *Transport in Porous Media* **88** (2), 205–223.
- XU, Z. & MEAKIN, P. 2008 Phase-field modeling of solute precipitation and dissolution. *The Journal of chemical physics* **129** (1), 014705–14784.
- YANG, X., FENG, J. J., LIU, C. & SHEN, J. 2006 Numerical simulations of jet pinching-off and drop formation using an energetic variational phase-field method. *Journal of Computational Physics* **218**, 417–428.
- YUAN, B. & WOOD, D. 2018 A comprehensive review of formation damage during enhanced oil and gas recovery. *Journal of Petroleum Science and Engineering* .
- ZENG, Z. & GRIGG, R. 2006 A criterion for non-Darcy flow in porous media. *Transport in porous media* **63** (1), 57–69.
- ZHENG, L., RAHMAN, M., AHAMMAD, M., BUTT, S., ALAM, J. *et al.* 2016 Experimental and numerical investigation of a novel technique for perforation in petroleum reservoir. In *SPE International Conference and Exhibition on Formation Damage Control*. Society of Petroleum Engineers.
- ZOBACK, M. D. 2010 *Reservoir geomechanics*. Cambridge University Press.